Phase resolved characterization of nanoscale features in optical microstructures

Thèse N° 9787

Présentée le 29 novembre 2019

à la Faculté des sciences et techniques de l'ingénieur
Laboratoire d'optique appliquée
Programme doctoral en photonique

pour l'obtention du grade de Docteur ès Sciences

par

Michail SYMEONIDIS

Acceptée sur proposition du jury

Prof. H. Altug, présidente du jury
Dr. T. Scharf, directeur de thèse
Dr A. Hermerschmidt, rapporteur
Dr M.-S. Kim, rapporteur
Prof. G. Villanueva, rapporteur

2019

ÉCOLE POLYTECHNIQUE
FÉDÉRALE DE LAUSANNE

I am a series of small victories and large defeats
and I am as amazed as any other
that I have gotten from there to here.
— Charles Bukowski

To those that extend a helping hand.
To those that wake you from the slumber.
To my friends and family.

Acknowledgements

You are reading my Doctoral Thesis, the result of my work and research for four years. Although the completion of the Thesis is an individual achievement, it would be selfish to claim that I achieved it on my own; I had help – direct or indirect – from various people in order to reach this point. Given this chance, I would like to express them my gratitude.

I have to start with my supervisor, Dr. Toralf Scharf, and the head of the NAM group, Professor Olivier Martin, both of whom I thank for the cooperation. Crucial for my scientific advancement has been also the collaboration with Radius, Andreas and Professor Carsten Rockstuhl from Karlsruhe Institute of Technology and Rossella and Professor Thomas Bürgi from University of Geneva. Thank you all very much for helping me write a peer-reviewed paper. I enjoyed the process, no matter how stressful; it was a pleasure working with you. Equally insightful and constructive was the collaboration with Professor Wataru Nakagawa, whom I sincerely thank for all the help and discussions – scientific or otherwise – we held together. I also appreciate the help of Dr. Andreas Hermerschmidt, Dong-Cheon and Jeremy. I would like to specially thank Dr. Myun-Sik Kim for all the inspiration and guidance. Although it was only for a few months, it was pivotal for my research to advance. I am also grateful to all my colleagues and peers for the support and the fun times we had together. I also owe a big, big thank you to all Tuesday's (ir)regulars for all the beers, jokes and advice we shared.

Finally, I thank my parents because, if it wasn't for them, I wouldn't be neither.

Thessaloniki, 18 September 2019 M. S.

Abstract

In this study, we apply interferometric microscopy to study the phase, alongside the intensity, of the light field transmitted through a wide variety of samples. Additionally, we conduct those interferometric measurements at different wavelengths within the visible spectrum, probing the spectral evolution of the optical effects that the studied samples create. Using a priori knowledge about the samples, we identify specific features and trends they imprint on the parameters of the transmitted field, thus we optimally analyze the recorded intensity and phase data. We demonstrate that phase maps include useful information that reveal the features of the samples. The wide applicability of the spectrally resolved interference microscopy is the major novelty contributed by the present work. The phase seldom recorded, therefore we first present and explain the tools that we use throughout this work, both in terms of set-up and data post-processing. Next, we show the acquired results, starting from samples with typical dimensions in few hundreds of microns and concluding with particles of few hundreds of nanometers. More specifically, we study microlenses of high numerical aperture that are difficult to characterize with conventional methods. We propose a novel approach to extract the surface profile of such microlenses, providing useful feedback for manufacturing purposes. We do that by using phase measurements at a plane that lies between the surface of the lens and its focal plane. The next sample we study is a phase element, which is naturally easier to discern in the phase domain. We localize specific points in intensity and phase profiles that are correlated to the position of the walls of the actual sample. We also demonstrate the existence of phase singularities in phase measurements that can be proved an invaluable tool in high precision characterization processes. Next, we investigate the photonic nanojet phenomenon, which is the bright spot created on the shadow side of a dielectric sphere. The creation of this bright spot is not achieved through propagation inside the material, like conventional lenses, it is the combination of the light scattered and diffracted by the sphere. Therefore, we study its spectral evolution using intensity measurements and outline the size of the sphere that indicates the crossing from the dominant refractive regime to the diffractive one; combining intensity and phase information, we attempt to identify the size at which the behavior of the dielectric spheres changes again from diffractive to scattering regimes. In the last experiments chapter, we study individual nano-sized particles, which are either simple spheres (dielectric / metallic) or the more complex structures of the core-shell meta-atom. We show that the spectral information of their response in intensity and phase can be used to identify the particle itself (simple dielectric, metal or meta-atom) and assess its responses with the respect to the engineered one (for the meta-atom case). Those examples validate the claimed benefits of the phase exploration. Still, there is ample room for further study; we debate about those prospects in the concluding chapter of this work.

Keywords: Interference microscopy, spectrally resolved interferometry, microlenses, diffractive optical elements, photonic nanojet, meta-materials, meta-atom, nano-particles

Zusammenfassung

In dieser Studie untersuchen wir wie die Phaseninformation eines übertragenen Lichtfeldes in der Interferenzmikroskopie genutzt werden kann um spezifische Merkmale einer Probe zu untersuchen. Dabei konzentrieren wir uns auf Probleme deren Strukturgrössen im Mikrometerbereich liegen. Ein wesentliche Neuerung die wir einführen ist die Messungen bei verschiedenen Wellenlängen. Dadurch kann gezielt der Einfluss der Wellenlänge auf optischen Effekte untersucht werden. Um die Informationen aus Intensitäts- und Phasendaten optimal zu nutzen ist a priori Wissen über die Proben, deren Struktur und Zusammensetzung, wichtig. Nur so lassen sich die Resultate aus Simulationen und Messungen komplexer drei dimensionaler Phasen- und Intensitätsfelder sinnvoll interpretieren. In vielen praktischen Fällen wird die Phase des Lichtes nicht aufgezeichnet, weil man dazu spezielle Techniken benötigt. Daher stellen wir zunächst diese Techniken vor, wobei wir auf den Aufbau und die wesentlichen Elemente der Datennachbearbeitung eingehen. Als nächstes diskutieren wir die verschiedene Anwendung auf Probleme im sogenannten resonanten Bereich, in welchem Streuung Beugung und Brechung des Lichtes eine nicht zu vernachlässigende Rolle spielen. Die untersuchten Proben haben dabei typische Abmessungen die von hundert Mikrometern bis hin zu Partikeln mit einem Durchmesser von wenigen hundert Nanometern reichen. Zuerst untersuchen wir Mikrolinsen mit hoher numerischer Apertur, deren Oberflächenprofil mit herkömmlichen Methoden nur schwer zugänglich ist. Das Oberflächenprofil ist wichtig in für die Herstellung der Mikrolinse. Wir schlagen einen neuartigen Ansatz vor, indem wir Phasenmessungen in einer Ebene durchführen, die zwischen der Oberfläche der Linse und ihrer Fokusebene liegt. Als weitere Anwendung untersuchen wir diffraktive optische Elemente. Solche diffraktiven Optiken haben stufenförmige Oberflächenprofile und erzeugen eine Phasenmodulation des Lichtes. Zur Qualitätskontrolle ist eine genaue Positionsbestimmung der Stufen wichtig und wir zeigen, wie Intensitäts- und Phasenprofile zur deren hochpräzisen Messung benutzt werden kann und wie sich die Existenz von Phasensingularitäten einsetzen lässt. In einem weiteren Beispiel wird das Phänomen des photonischen Nanojet betrachten. Der photonische Nanojet erzeugt eine Lichtbündelung auf der Schattenseite einer dielektrischen Kugel. Die Erzeugung dieser Lichtbündelung wird durch die Kombination des von der Kugel gestreuten und gebeugten Lichts erzeugt. Interessant ist hier die Untersuchung der spektralen Eigenschaften, da diese nicht mehr auf dem klassischen Konzept der Brechung beruht. Mit wellenlängenaufgelösten Messungen können wir hier ein neues Kriterium für den resonanten Bereich einführen. Dabei benutzen wir eine Kombination aus Intensitäts- und Phaseninformationen und identifizieren, bei welcher Größe sich das Verhalten der dielektrischen Kugeln von brechend zu beugend und streuend ändert. Für kleinste Strukturen spielt die Streuung eine dominate Rolle. Im letzten Kapitel untersuchen wir deshalb wie wellenlängenabhängige Interferenzmikroskopie benutzt werden kann, um Strukturen kleiner als die Wellenlänge zu charakterisieren. In den Experimenten untersuchen wir einzelne Partikel, die entweder homogene Kugeln oder komplexe Strukturen eines typischen Kern-Schale-Meta-Atoms sind. Wir zeigen, dass die spektrale Information der Phasen- und Intensitätsmessungen verwendet werden können, um Teilchen zu identifizieren oder die verschiedenen Einflüssen der Komponenten im Falle des Metaatoms zu bewerten. All diese Beispiele zeigen die Vorteile die Messungen der Phase zur Untersuchung komplexer Probleme im resonanten Bereich beitragen können. Unsere Untersuchen zeigen aber auch das weitere Studien sinnvoll sind und wir diskutieren diese Perspektiven im abschließenden Kapitel dieser Arbeit.

Contents

1 Introduction

Light is inextricably linked to the progress of civilization, be it in society, arts, economy or science. In the latter domain, where this work also belongs to, light is but a small part in the center of the electromagnetic spectrum (Fig. 1.1); what makes it utterly important however, is the fact that the human eye is sensitive to that part of the electromagnetic radiation, it is what allows us to "see". It should come with no surprise then, that the interest of manipulating light, in the form of mirrors, lenses, color filters, etc. can be traced back to ancient times.

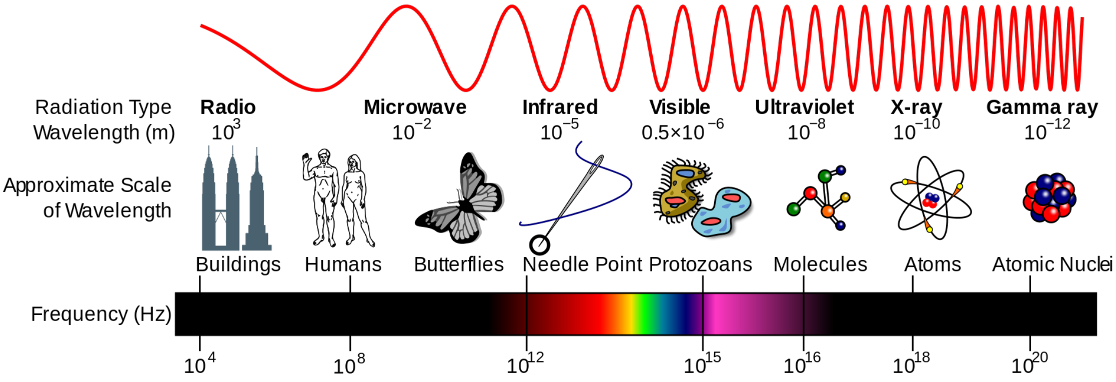

Figure 1.1 – Electromagnetic spectrum and its regions. Image adapted from Wikipedia.

The recent understanding of the nature of light, along with technical advances in fabrication and analysis of optical components have enabled us to look at tiny features; structures whose dimensions lie in the micro-scale. This is the aim of microscopy, which is the most widely used tool in the metrology field, i.e. the science of measuring and quantifying the properties of objects. Microscopy is also the technique we use in this work, since we study nano-scale features that optical micro-structures imprint on a light field. To be more precise, the main idea is to shine light on a specific structure and, by collecting the light that is transmitted through it, conclude on its properties.

This is already a small deviation from conventional microscopy, since we are not imaging the structures themselves, rather we extract information about them, by analyzing the transmitted light. Additionally, we examine the phase, alongside the intensity of the light field, that is not often investigated. To better appreciate the motivation of this choice, let us study the properties of light a bit closer. In the framework of classical physics, light can be regarded as a wave $\mathbf{u}(\mathbf{r}, t)$ that is mathematically described by the real function:

$$\mathbf{u}(\mathbf{r}, t) = u_x(\mathbf{r}, t)\hat{\mathbf{x}} + u_y(\mathbf{r}, t)\hat{\mathbf{y}} + u_z(\mathbf{r}, t)\hat{\mathbf{z}}, \tag{1.1}$$

where $\mathbf{r} = (x, y, z)$ is the position and t is time. Each component u_i of the wavefunction satisfies the wave equation:

$$\nabla^2 u_i - \frac{1}{c^2}\frac{\partial^2 u_i}{\partial t^2} = 0, \tag{1.2}$$

where ∇^2 is the Laplacian operator and c is the speed of light inside the medium. A function that satisfies eq. 1.2 is:

$$u_x(\mathbf{r}, t) = \alpha(\mathbf{r}) \cos\left[2\pi v t + \phi(\mathbf{r})\right], \tag{1.3}$$

where $\alpha(\mathbf{r})$ is the amplitude, v is the frequency and $\phi(\mathbf{r})$ is the (spatial) phase. The harmonic time dependence of eq. 1.3 implies that the field oscillates with a single frequency (monochromatic). We assume, without loss of generality, a wave that has non-zero components only along $\hat{\mathbf{x}}$, which means that it is linearly polarized along that axis. The monochromatic wave gives us a well defined time dependence and the linear polarization allows us to use a scalar function, both of which greatly simplify the analysis, while still being reasonable and easy to produce (e.g. with Laser sources and polarizers). Using the superposition principle, we can lift those assumptions in a straightforward, yet computationally demanding way. Having said that, we will continue to use eq. 1.3 to show the necessary concepts for this work. The first remark is that in order to fully describe the wave, we need its amplitude $\alpha(\mathbf{r})$ and its phase $\phi(\mathbf{r})$ (assuming the frequency v is known). However, most measurements record the intensity of the field, that is related to its amplitude and phase is not often investigated. As expected, there are sound reasons for this fact.

Why is phase not always measured?

The answer to that question is really simple; all the available optical sensors (e.g. photosensitive film, photo-diode, eye) are sensitive only to the intensity of the impinging field. Here we should clarify what is intensity and how it is related to the amplitude of eq. 1.3. The optical intensity $I(\mathbf{r}, t)$, defined as the optical power per unit area (units of watts/cm^2), is proportional to the average of the squared wavefunction:

$$I(\mathbf{r}, t) = 2\langle u^2(\mathbf{r}, t)\rangle. \tag{1.4}$$

The averaging, denoted by the operator $\langle\cdot\rangle$, is taken over a time interval much longer than the period of light, since at optical frequencies the period of one cycle is extremely short: 2×10^{-15} s for a light of wavelength $\lambda = 600\,\text{nm}$ for example. The definition contains some arbitrariness regarding the factor 2, however this factor will be proven convenient shortly and this definition still connects the wavefunction with a physically measurable quantity. Introducing eq. 1.3 into eq. 1.4, we get:

$$I(\mathbf{r}) = \alpha^2(\mathbf{r}), \tag{1.5}$$

which shows the relation between intensity and amplitude.

Since we cannot measure the phase of the field directly, we must find an indirect method of measurement. Thanks to the superposition principle, when two waves are simultaneously present at the same space, the resulting wave is their sum. This leads to the interference effects that are described below. In order to elegantly describe those effects, we will use the complex representation of the wavefunction:

$$U(\mathbf{r}, t) = \alpha(\mathbf{r}) exp\left[j\phi(\mathbf{r})\right] exp\left(j2\pi\nu t\right), \tag{1.6}$$

which is equivalent to eq. 1.3, since:

$$u(\mathbf{r}, t) = \Re\{U(\mathbf{r}, t)\} = \frac{1}{2}\left[U(\mathbf{r}, t) + U^*(\mathbf{r}, t)\right], \tag{1.7}$$

where U^* is the complex conjugate. By inserting eq. 1.6 into eq. 1.4, it follows:

$$I(\mathbf{r}) = |U(\mathbf{r})|^2. \tag{1.8}$$

The superposition of two monochromatic waves of the same frequency can be written as:

$$U(\mathbf{r}) = U_1(\mathbf{r}) + U_2(\mathbf{r}), \tag{1.9}$$

where we omit the harmonic time dependence for simplicity. The intensity of the resulting wave U is given by:

$$I = |U|^2 = |U_1 + U_2|^2 = |U_1|^2 + |U_2|^2 + U_1^* U_2 + U_1 U_2^*. \tag{1.10}$$

Expressing U_i as:

$$U_1 = \sqrt{I_1} exp(j\phi_1) \quad \text{and} \quad U_2 = \sqrt{I_2} exp(j\phi_2), \tag{1.11}$$

where ϕ_i is the phase of the waves, we get:

$$I = I_1 + I_2 + 2\sqrt{I_1 I_2}\cos(\Delta\phi), \tag{1.12}$$

with $\Delta\phi = \phi_2 - \phi_1$. Equation 1.12 shows that the phase of the superimposing waves also affect the resulting intensity and provides us with a way to extract phase (difference) information using only intensity measurements. More details on how this is done are given in the next chapter. It is obvious though that another wave is necessary, which increases the complexity of the measuring configuration; that is the reason why the simpler intensity measurements are much more often used, despite the fact that there is a way to extract the phase information.

Is phase important?

Since we have shown how the phase information can be extracted, the next question that arises is *why* to do it. As said previously, phase is necessary to fully describe a wave. An object can be regarded as group of many individual point sources, each of which emits a different wave. The importance of phase information grows, when those sources are coherent, since such processes are characterized by phase [1]. In order to demonstrate the importance of phase in signals, we repeat the idea of a classic paper of Oppenheim and Lim [2].

Before we show the experiment itself, we will remind that, according to Fourier analysis, an arbitrary [1] function $f(x, y)$ can be analyzed into a sum of harmonic functions of different *spatial* frequencies and complex amplitudes (all functions have the same time dependence). The Fourier transform of a function gives those complex amplitudes that indicate how strong each function is (amplitude of Fourier coefficients) and where the maxima and minima lie (phase of Fourier coefficients). Mathematically, we can write the function $f(x, y)$ as a sum of harmonic functions of the form:

$$F(v_x, v_y) exp\left[-j2\pi(v_x x + v_y y)\right], \tag{1.13}$$

where $F(v_x, v_y)$ is the complex amplitude and v_x and v_y are the spatial frequencies.

This is schematically shown in Fig. 1.2, where the image of Jean-Baptiste Joseph Fourier is decomposed into its Fourier components. Those components are essentially plane waves, travelling along different directions, and we plot the wavefunction at a z = constant plane.

Going back to the initial experiment, we will utilize the Fourier analysis to demonstrate the importance of phase. In Fig. 1.3(a) we show a gray-scale image of Albert Einstein with dimensions 512 pixels × 512 pixels. Figures 1.3(b) and 1.3(c) show the log-scaled magnitude (the absolute value of the amplitude that is easier to visualize) and the phase of the Fourier

---

[1] There are some constrains of course. There are plenty of textbooks giving details on the matter.

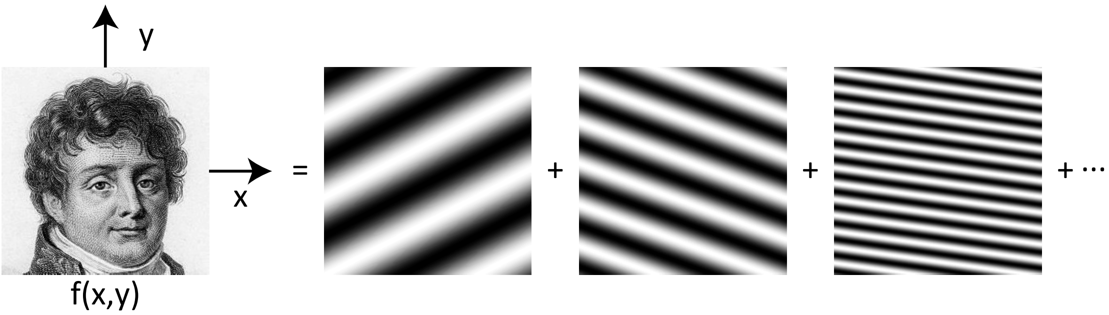

Figure 1.2 – An arbitrary function $f(x,y)$ can be analyzed as a sum of harmonic functions of different *spatial* frequencies and complex amplitudes. The image of Jean-Baptiste Joseph Fourier is the infinite sum of plane waves travelling at different directions.

coefficients, respectively. Each point on the image corresponds to a pair of spatial frequencies υ_x and υ_y, along x and y direction. The same information is shown in Fig. 1.4, this time for a grey-scaled image of Mona Lisa. We observe that the magnitude has a better defined shape when compared to the phase, that to a large extend, seems random.

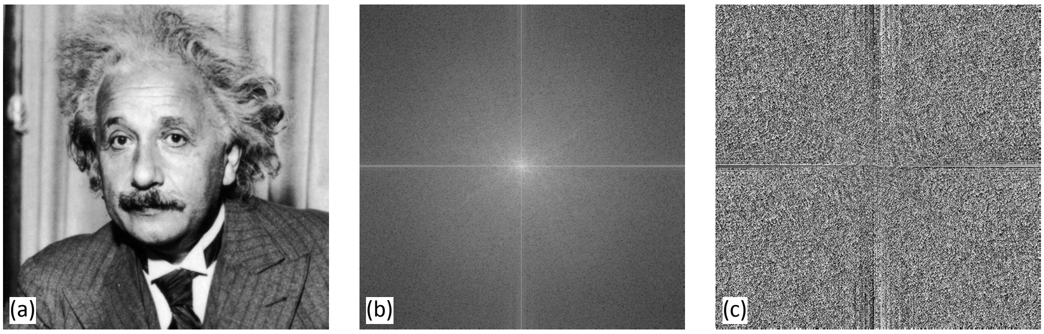

Figure 1.3 – (a) Image of Albert Einstein. (b) log-scaled magnitude and (c) phase of its Fourier components.

Since the coefficients of the images are known, we can describe the plane waves that compose the image, thus we can re-create the initial image by applying the inverse Fourier transform. This is trivial however, so we will create two different images by combining the Fourier coefficients of the two images. In the first case we combine the magnitude of the Fourier transform of the image of Albert Einstein with the phase coefficients calculated for the Mona Lisa's image. In the second case we take the other combination, i.e. the magnitude of the Fourier coefficients of Mona Lisa's image and the phase coefficients extracted from Albert Einstein's image. To formulate it mathematically, we can write:

$$\begin{array}{lllllll} I_1(x,y) & = & FT\{i_{Albert}(x,y)\} & I_2(x,y) & = & FT\{i_{Lisa}(x,y)\}, \\ I_3(x,y) & = & |I_1|exp\left[j\cdot\angle(I_2)\right] & I_4(x,y) & = & |I_2|exp\left[j\cdot\angle(I_1)\right], \end{array} \quad (1.14)$$

where $FT\{\cdot\}$, denotes the Fourier transform operation and $\angle(I_i)$ is the angle of the complex

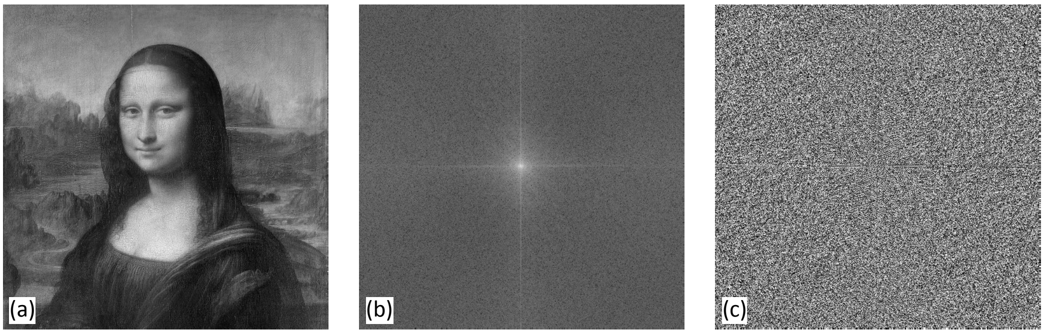

Figure 1.4 – (a) Image of Mona Lisa. (b) log-scaled magnitude and (c) phase of its Fourier components.

function I_i.

The resulting inverse Fourier transform of I_3 and I_4 are shown in Figs. 1.5(a) and 1.5(b), respectively, which makes evident the effect of phase. The resulting image resembles stronger the image whose phase was used for its creation. Figuratively, one could say that amplitude dictates how much light there is, while phase defines how the light is distributed in space. Neglecting the phase information, or assuming a different phase map from the actual one, can produce heavily misleading results.

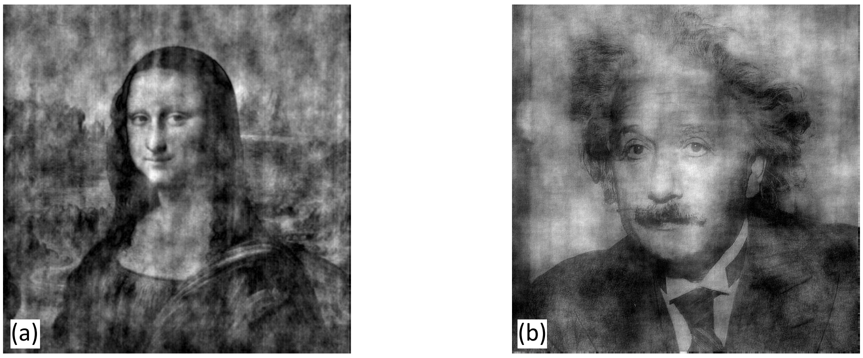

Figure 1.5 – (a) Inverse Fourier transform of the image created using Albert Einsteins's magnitude Fourier coefficients and Mona Lisa's phase Fourier coefficients and (b) of the image created using Mona Lisa's magnitude Fourier coefficients and Albert Einstein's phase Fourier coefficients. The results resemble much stronger the image, whose phase was used.

Another reason that makes the extraction of phase beneficial is related to the resolution limit of microscopy. To better understand this concept, let us assume a circular aperture that is illuminated by a point source. According to Fraunhofer analysis, the diffraction pattern of the aperture on the observation plane is given by the formula:

$$I(P) = |U(P)|^2 = \left[\frac{2J_1(k\alpha R)}{k\alpha R}\right] I_0, \tag{1.15}$$

where $k = \frac{2\pi}{\lambda}$ is propagation constant, α is the radius of the aperture, R is position on the observation screen and I_0 is the intensity in the center, which can be assumed normalized, so that $I_0 = 1$. This formula is known as Airy disk pattern. The configuration is shown in Fig. 1.6(a), while the formula is plotted in Fig. 1.6(b). The inset shows the calculated diffraction pattern of a circular aperture of radius $\alpha = 1\,\mu\text{m}$, illuminated by the wavelength of $\lambda = 500\,\text{nm}$ and viewed at a distance of $Z = 1\,\text{mm}$. The image is intentionally overexposed to highlight the low intensity rings. The phase of this function is constant within each bright ring and consecutive rings show a phase difference of π.

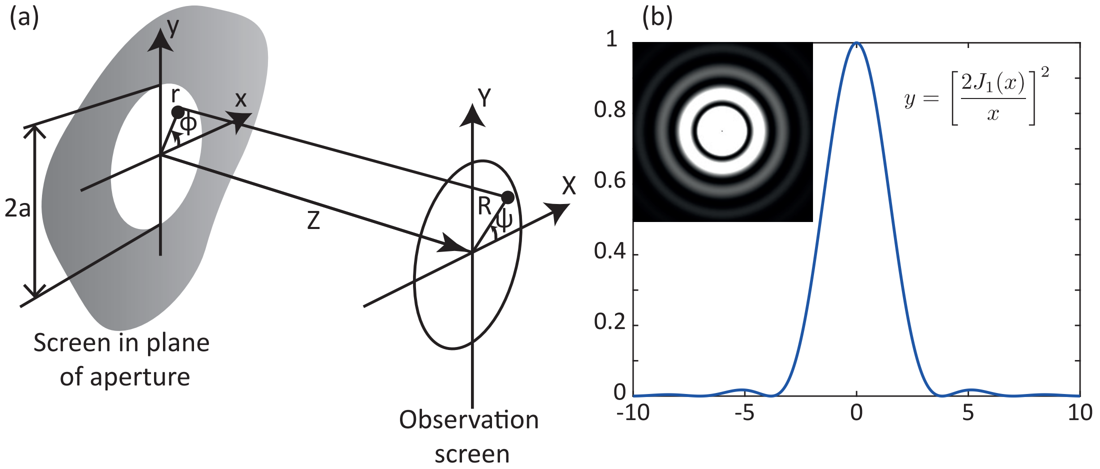

Figure 1.6 – A circular aperture illuminated by a point source creates a diffraction pattern on the observation plane (a). This pattern is the Fraunhofer approximation is described by the Airy function, shown in (b). The inset shows the calculated diffraction pattern of a circular aperture of $\alpha = 1\,\mu\text{m}$, illuminated at $\lambda = 500\,\text{nm}$, viewed at a distance of $Z = 1\,\text{mm}$.

If we imagine a lens filling the aperture and the sources being two distinct points of a sample under examination, the diffraction pattern of the two source will appear on the image plane of the lens. In order for two points to be distinguishable, they should be sufficiently separated. One criterion for incoherent illumination states that the two points of equal intensity can be resolved if the maximum of the one diffraction pattern coincides with the minimum of the other, which results in a minimum separation of:

$$D_{min} \approx 0.61 \frac{\lambda_0}{n sin\theta}, \tag{1.16}$$

where λ_0 is the illuminating wavelength, n is the refractive index of the surrounding medium and θ is the angle that the marginal ray form with the optical axis. This is know as the Rayleigh criterion which is frequently used, since it is reasonable, for resolving different peaks, to have one maximum coincide with the other zero. However, there is no physical significance behind this choice, in the sense that there is no physical law that enforces this threshold.

In the case of coherent illumination, the resolution limit was first investigated by Ernst Abbe, and the criterion that carries his name states that the minimum resolvable distance is

$$D_{min} \approx 0.82 \frac{\lambda_0}{n sin\theta}, \tag{1.17}$$

where the quantities are as in eq. 1.16. According to this criterion, the intensity dip between the two diffracted spots is about 26.5 %, which is actually the same dip for the Rayleigh criterion [3].

Both criteria result in a resolution limit that is about half a wavelength; they where extracted however, taking into account the intensity of the diffraction pattern. At the positions where the intensity drops to zero, the phase change abruptly by π, creating a very sharp transition in the phase map. Similar positions might be exploited to identify features and structures below the limit imposed by diffraction. It should be stressed that we do not infer imaging with a resolution below diffraction, rather localization of specific features with high-precision.

Recording the phase information has another distinct advantage, when it comes to the study phase elements. The intensity patterns created by such elements have low contrast, since they only affect the phase of the incoming field and have negligible absorption. For that reason, the phase contrast method was developed by Zernike that translates phase difference into intensity difference and therefore allows for observation of higher contrast intensity variations. This method is based on changing the phase of the 0^{th} diffracted order of a sample, compared to the higher orders. However, since we investigate the phase domain, we can directly see regions having different phase profiles with high contrast.

Beyond phase - spectrally resolved measurements

The phase extraction feature becomes more appealing when we can utilize it within the visible range from λ = 450 nm to 700 nm to study the chromatic behavior of the samples. The relation between the properties of the material and the frequency (consequently and the wavelength) is called dispersion and its source is, within a qualitative approach, the forces that keep the atoms of the material in place; those forces make the polarization of the material, which is the alignment of dipoles inside the material along the axis of the electric field, not instantaneous, thus a dependence on time (and frequency) arises. This change of the properties is shown in eq. 1.2 in the form of $c = \frac{c_0}{n(v)}$, where c_0 is the speed of light in vacuum and $n(v)$ is the refractive index of the material at a given frequency. The relation between refractive index of fused silica and wavelength is shown in Fig. 1.7. It is worth noting that below 0.5 µm the change of the refractive index is large.

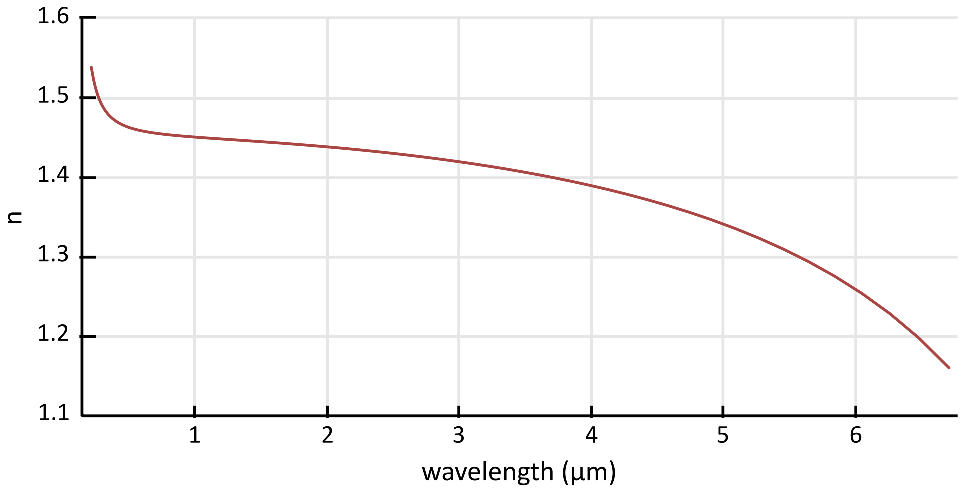

Figure 1.7 – Refractive index of fused silica against wavelength. It is worth noting that the fastest change of the refractive index appears below $\lambda = 0.5\,\mu\text{m}$.

What are we investigating?

Equipped with methods and a tool to extract intensity and phase information at different wavelengths, it is only natural to investigate samples whose functionality and properties are defined by shaping the phase of the illuminating field and the wavelength dependence is of interest.

Chapter 2 describes the instrument set-up and the methods used to record the data. The post-processing of the data is also demonstrated.

Chapter 3 presents a new technique for characterizing microlenses. The focusing effect of a conventional lens is the result of the phase profile that the light acquires as it passes through it. Therefore, having that information can reveal the deviations from the ideal lens. We apply this concept to high-quality microlenses, whose characterization is still challenging.

Chapter 4 focuses on phase elements, which are structures that affect only the phase of the incoming field. Consequently, the phase regime is a natural choice to investigate such structures, since special features arise there, due to the operating principle of the structure.

Chapter 5 investigates the photonic nanojet effect, which is the focusing of light by micron-sized dielectric spheres. The dimensions of those spheres indicate that the focal spot is not created by the propagation of light through the material. Thus we examine its chromatic behavior and record the phase evolution, attempting to better understand and describe the phenomenon.

Chapter 6 studies the response of simple particles (dielectric and metallic spheres) and complex structures (core-shell meta-atoms) that are composed out of the simpler ones, at different wavelengths. We point out the differences and similarities between them and relate them to the spectral response of the individual particles.

Chapter 7 concludes the work. In a few words, the knowledge of some properties of the samples allows us to utilize the phase profile produced by those samples more efficiently, in the sense that we focus on the features produced by the known properties.

As we progress throughout this work, the dimensions of the examined samples shrink; starting from microlenses with dimensions in the order of few hundreds of micrometers, we advance to diffractive optical elements that have a typical size of few tenths of microns. Next comes up the photonic nanojet investigation using microspheres with typical dimension a few microns and we conclude the study with particles of a few hundreds of nanometers. In every case though, we examine features that those samples imprint on the light field, either on intensity or phase, that are much smaller compared to the structures that create them.

Investigating the phase is not a new concept; neither is the study of the chromatic behavior. Their combination however is seldom and restricted to special cases[4, 5, 6, 7]. In this work, we demonstrate that prior knowledge about the structure under study enables the extraction of a multitude of the properties of the sample, efficiently utilizing the information contained in the measured field. This is shown for different cases that while being quite distinct in appearance, they are all governed by the same physical concepts. There are many resources for a more detailed description of the concepts and phenomena described here, [8, 9, 10, 11, 12] for example are widely suggested reading supplies.

Bibliography

[1] J.M. BLACKLEDGE. *Quantitative Coherent Imaging.* Academic Press, London, 1989.

[2] A. V. Oppenheim and J. S. Lim. The importance of phase in signals. *Proceedings of the IEEE*, 69(5):529–541, May 1981.

[3] Max Born and Emil Wolf. Elements of the theory of diffraction. In *Principles of Optics*, chapter 8. Cambridge University Press, seventh (expanded) edition, 1999.

[4] A. Börzsönyi, A.P. Kovács, M. Görbe, and K. Osvay. Advances and limitations of phase dispersion measurement by spectrally and spatially resolved interferometry. *Optics Communications*, 281(11):3051–3061, June 2008.

[5] Daniel X. Hammer, Ashley J. Welch, Gary D. Noojin, Robert J. Thomas, David J. Stolarski, and Benjamin A. Rockwell. Spectrally resolved white-light interferometry for measurement of ocular dispersion. *Journal of the Optical Society of America A*, 16(9):2092–2102, September 1999.

[6] J. Calatroni, A.L. Guerrero, C. Sáinz, and R. Escalona. Spectrally-resolved white-light interferometry as a profilometry tool. *Optics & Laser Technology*, 28(7):485–489, October 1996.

[7] Ki-Nam Joo and Seung-Woo Kim. Refractive index measurement by spectrally resolved interferometry using a femtosecond pulse laser. *Optics Letters*, 32(6):647–649, March 2007.

[8] Joseph W. Goodman. *Introduction to Fourier Optics.* Number McGraw - Hill Series in Electrical and Computer Engineering. McGraw - Hill, 2 edition, 1996.

[9] Eugene Hecht. *Optics.* Pearson Education Limited, fourth edition, 2014.

[10] Bahaa E. A. Saleh and Malvin Carl Teich. *Fundamentals of Photonics.* John Wiley & Sons, Inc., 2 edition, 2007.

[11] K.D. Möller. *Optics.* University Science Books, 1988.

[12] Max Born and Emil Wolf. *Principles of Optics.* Cambridge University Press, seventh (expanded) edition, 1999.

2 Set-up description

The aim of this work is to explore the applications of recording the intensity and phase of the light field, after it passes through a structured, transparent sample. We are targeting samples whose features sizes spread within the range from a few hundreds of micrometers to few hundreds of nanometers.The measurement requirements for resolution and precision can be fulfilled by an interferometric microscope that can be easily modified to accommodate for different illumination and measurement conditions and is capable of running intensity-only measurements with minimum changes [1, 2, 3, 4]. Additionally, we probe the spectral behavior of the examined samples, thus the interferometric arrangement is further enhanced with the capability of recording data at different spectral regions. This novelty greatly increases the capability, in terms of structures or optical phenomena in general, that can be analyzed in detail by the set-up described in this chapter.

2.1 Spectrally adjustable high-resolution interference microscope

The working principle of the set-up is to combine a microscope with a Mach-Zehnder interferometer, which is a flexible design that can be readily used as a conventional microscope by blocking the reference beam. A schematic of the set-up is shown in Fig. 2.1. The Mach-Zehnder interferometer is an amplitude-dividing configuration, so the intensity of the beam entering the interferometer is splitted in two arms, the reference and the object arm, by the first beam-splitter. Each beam then travels along its respective arm; the phase profile of the beam transversing the reference arm remains unchanged, while the signatures of the sample are imprinted on the beam that propagates the object arm and through it. A detail analysis of each arm is given below. The second beam-splitter recombines the two beams and their interference pattern is projected on the detector (CCD sensor, pixel size: 4.65 µm × 4.64 µm, Scion Corporation, CFW-1312M).

A photograph of the actual implementation is shown in Fig. 2.2; the input of the interferometer is at the position of the first beam-splitter (BS1), which splits the incoming amplitude into the reference (solid line) and object (dashed line) arms. Along the reference arm, there are

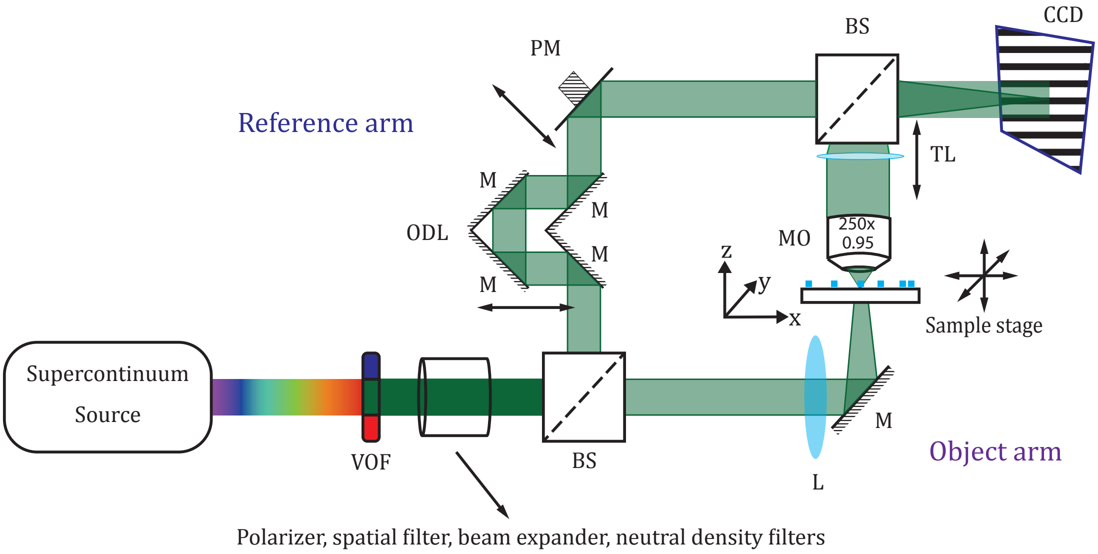

Figure 2.1 – Schematic diagram of the set-up. The interference microscope is based on the Mach-Zehnder design. VOF: variable optical filter, BS: beam-splitter, L: long focal-length lens, M: mirror, MO: microscope objective, ODL: optical delay line, PM: piezo-mirror, CCD: charge-coupled device (camera).

only planar reflective surfaces that do not change the phase profile of the beam, while the object arm contains more optical elements and, most importantly, the sample. The second beam-splitter (BS2) recombines the two beams and the resulting interference is projected on the image sensor of the camera. The various components and their purpose are explained in the following parts. Here, we should point out that, due to the fact that the beams are steered in three dimensions, special care should be taken to preserve the direction of propagation when the $x-y$ plane (parallel to the optical table) changes in order to avoid a change in the state of polarization, an effect often mentioned as *the periscope effect* [5].

2.1.1 Source

In order to probe the spectral behavior of the samples under study, we adjust the (central) wavelength λ_0 of the light impinging on the sample. The important parameters regarding its spectral behavior are the spectral range, the available power and the collimation of the illuminating beam. We use a super-continuum source (SuperK Fianium, NTK Photonics) that has a high-power and collimated output within the visible and the near-infrared spectrum from $\lambda = 0.40\,\mu\text{m}$ to $2.4\,\mu\text{m}$. Subsequently, the output is filtered by a variable optical filter (SuperK VARIA, NKT Photonics), which allows the selection of the transmission peaks within the range of $\lambda = 400\,\text{nm}$ to $840\,\text{nm}$. The NIR part of the power is disregarded by a hot-cold mirror within the filter. The transmission bandwidth can be adjusted from 5 nm to 440 nm. However, this affects the coherence length of light, as will be explained later on. Since we are interested in the quasi-monochromatic response of the samples, we use the narrowest

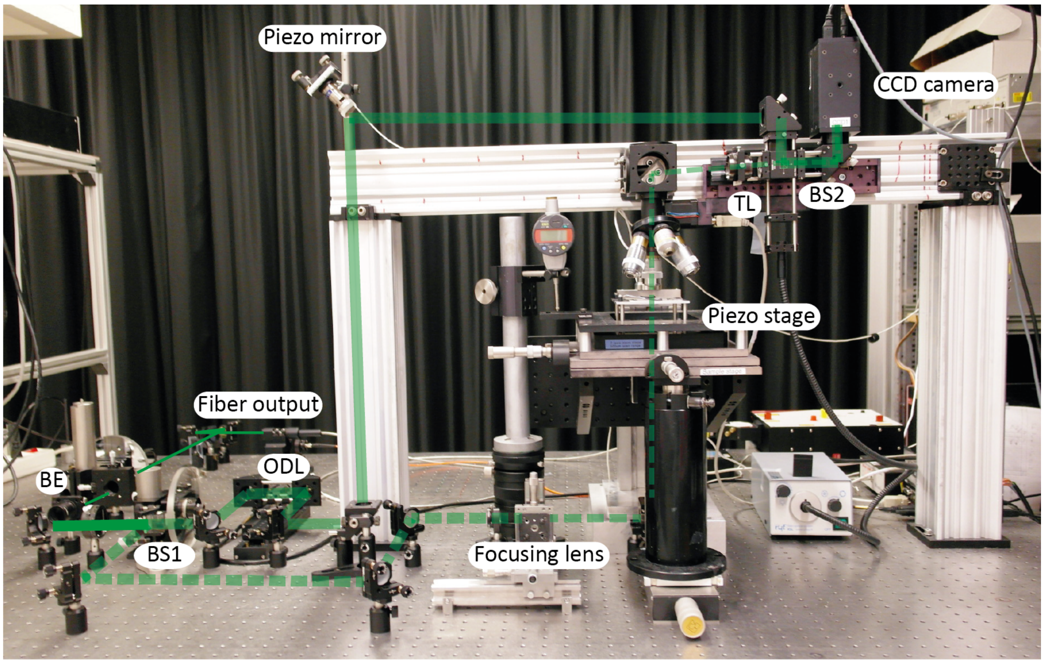

Figure 2.2 – Picture of the actual set-up. BE: beam expander, ODL: optical delay line, TL: tube lens, BS1: beam-splitter, BS2: beam-combiner. The interferometer is defined by the two beam-splitter. The solid line indicates the path of the reference arm, while the dashed line follows the path of the object arm.

bandwidth of the filter, which is effectively $BW \approx 7\,\text{nm}$. Figure 2.3(a) shows the output of the filter when the bandwidth is set to $BW = 440\,\text{nm}$ (effectively the visible spectrum of the source), normalized to its maximum value. The available power depends heavily on the central wavelength, which signifies the importance of spectral power management. In Fig. 2.3(b) the output of the filter is shown for a bandwidth of $BW = 5\,\text{nm}$, as the central wavelength is scanned from $\lambda_0 = 450\,\text{nm}$ to 840 nm. The measured mean full width at half maximum of the transmission peaks is $FWHM \approx 7\,\text{nm}$ and the total power of each peak ranges from 5 mW to 25 mW, depending on the wavelength.

The output of the filter is then coupled into a phtotonic crystal fiber (SuperK CONNECT, FD7), which ensures the highest beam quality and stability, since it delivers a monomode output across all the wavelengths. The output is an almost ideal Gaussian beam (quality factor $M^2 < 1.1$). Although the coupling efficiency is optimized for a single wavelength, the overall transmission remains adequate ($T > 50\%$) for all the wavelengths. Most importantly, the position of the fiber output remains unchanged, thus no realignment of the optics that follow is needed, when selecting a different wavelength. The working principle of the SuperK VARIA tunalbe single line filter (linear high-pass and low-pass filters moving in opposite directions) results in a slight displacement of the beam, which, nevertheless, becomes important after a few reflections. The beam is unpolarized and its diameter within the visible range is $D = 1\,\text{mm}$. Photographs of the variable optical filter and the fiber coupling module are shown in Fig. 2.4.

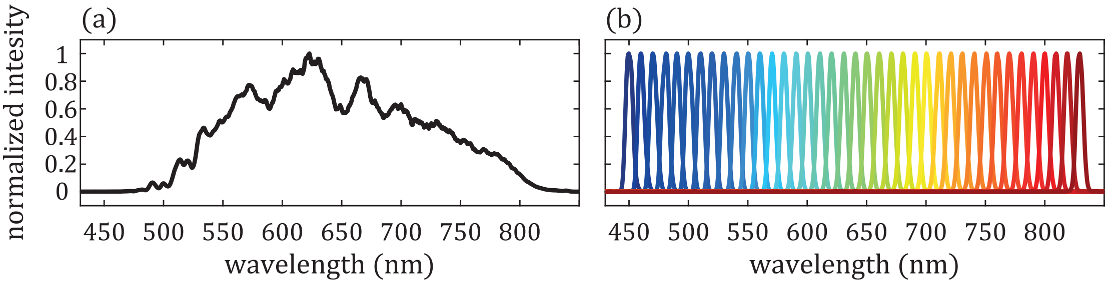

Figure 2.3 – (a) Emission of the source in the visible spectrum. The output power depends heavily on the central wavelength λ_0. (b) filtered output setting the transmission bandwidth at $BW = 5\,\mathrm{nm}$. The central wavelength is scanned from $\lambda = 450\,\mathrm{nm}$ to $840\,\mathrm{nm}$. The measured mean full width at half maximum of the transmission peaks is $FWHM \approx 7\,\mathrm{nm}$.

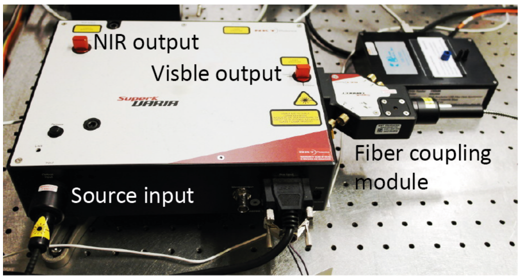

Figure 2.4 – Variable optical filter and fiber coupling module.

2.1.2 Beam shaping

Before entering the interferometer, the parameters of the beam are changed to suit every time the conducted experiment. The beam shaping has to fulfill the following functions:

- align the beam to the optical axis of the set-up,
- adjust the power (avoid saturation),
- clean the beam (spatial filtering),
- adjust the beam diameter (beam expander),
- select a specific angle of (linear) polarization.

First, the beam is aligned to the optical axis of the components, using a perpendicular (figure-4) configuration, shown in Fig. 2.5a, which is more compact compare to the π configuration. Next, a reflective neutral density filter is used to adjust the power of the incoming beam and avoid saturating the detector. After that, the beam is cleaned by a spatial filter.

An achromatic lens with focal length $f = 25\,\mathrm{mm}$ focuses it on a pinhole of diameter $D = 50\,\mu\mathrm{m}$, which allows only the fundamental Gaussian mode to propagate. A second achromatic lens of focal length $f = 200\,\mathrm{mm}$ is placed at a distance equal to its focal length from the pinhole, in order to expand (≈ $x8$) and collimate the beam. The beam-expanding / spatial-filtering module is shown in fig. 2.5b The final beam diameter is ≈ 8 mm, so as to uniformly fill the aperture of the optic components that follow and to illuminate the maximum area of the detector.

Finally, a broadband wire-grid polarizer (MOXTEK), mounted on a rotation stage, is used to linearly polarize the beam at any angle on the plane perpendicular to the propagation axis. This type of polarizer is so thin, that even if its surface is not perfectly perpendicular to the propagation path, the beam displacement due to refraction is negligible. Using a prism polarizer for that purpose would require a much more strenuous alignment process.

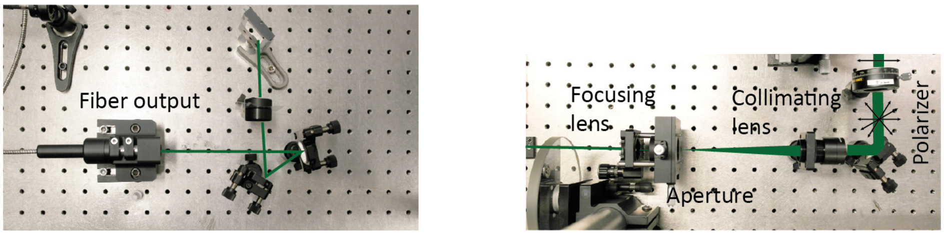

(a) figure-4 configuration

(b) Beam expander

Figure 2.5 – (a) Figure-4 configuration for aligning the beam to the optical axis of the components. (b) Beam expansion. spatial filtering and polarizing components.

2.1.3 Reference arm

Approximately half of the beam power is transmitted through the first beam-splitter into the reference arm. In this arm, the actions that are taken to optimize the interference visibility are the following: adjust the power, compensate for the transmission through the sample (and other optical components of the object arm) and implement the phase shifting interferometry technique, that is described in the next section.

More specifically, a second reflective neutral density filter (Fig. 2.6a) is used to adjust the power and approximately equalize it with the power level of the object arm, thus maximizing the contrast of the interference fringes. This neutral density filter has uniform thickness, therefore it does not change the optical path of the reference arm for different attenuation; this eliminates the need for readjusting the optical delay line, as it will be explained next.

Given that the coherence length L_c decreases for increasing bandwidth $L_c \propto \lambda_0^2/\Delta\lambda$, ($\lambda_0$ is the central wavelength) [6], the maximum optical path difference that still creates interference is some tenths of micrometers. The optical path of both arms changes for every wavelength, due to the dispersion of the various optical components (beam-splitters, lenses, microscope objective), so the purpose of the optical delay line is to keep the optical path difference smaller that the coherence length L_c, thus maximizing the visibility of the fringes. A set of two mirrors, mounted on a precision translation stage (Standa 8MT177-100) compose an optical delay line that compensates the time difference with which the two beams traveling along the two arms reach the detector. This can be done by adjusting the optical path of the reference arm with micrometer precision, thus increasing/decreasing the propagation length. A photograph of the optical delay line is shown in Fig. 2.6b.

The interferometer implements a phase shifting technique, specifically the five-steps algorithm [7], to extract the phase information. To do so, a mirror is mounted on a piezo-stage (Mad City Labs, MCL1946, max range 10 µm) and changes the optical path of the reference arm within the precision of 1 nm (Fig. 2.6c).

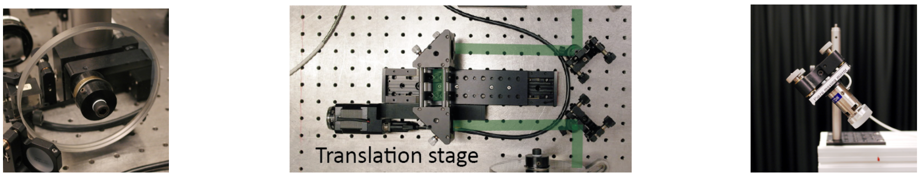

(a) Neutral density filter. (b) Optical delay line (c) Piezo mirror

Figure 2.6 – (a) Neutral density filter that equalizes the power in both arms, without changing the optical path of the reference arm. (b): Optical delay line that keeps the optical path difference shorter that the coherence length L_c. (c): Piezo-mirror that changes the optical path of the reference arm with high precision to implement the phase shifting interferometry technique.

2.1.4 Object arm

The remaining power of the beam entering the interferometer is reflected by the beam-splitter to the object arm to interact with the sample whose phase profile is imprinted on it. In this arm, the following issues are addressed: capturing the most of the available information, conditioning the illumination, positioning of the sample and conducting three dimensional measurements.

Since we investigate micron- and nano-scaled structures, we use objectives with high magnification and high numerical aperture, to achieve the highest resolution. For intensity measurements the resolution of the system is limited by the numerical aperture (at a given wavelength) and higher magnification does not always reveal more detail. There is a trade-off between the field of view and the pixel size that corresponds to the real plane. For a 250x magnification objective for instance, the field of view is ≈ 20 µm × 20 µm; given the pixel size and the magnification of the objective, each pixel of the detector corresponds to ≈ 20 nm in the real space, which is below the diffraction limit of a 0.95 NA objective (roughly 300 nm using the half-wavelength criterion and a central wavelength of $\lambda_0 =$;600 nm that corresponds to the features of the optical filter we use). This effect, termed *empty magnification*, does improve the discretization of the sample projected on the detector but not resolution. The advantages of utilizing this empty magnification will be analyzed in a later chapter, when phase measurements are discussed. Apart from the high-resolution of the objective, we also need them to have the highest aberrations correction. Therefore, we mainly use dry apochromatic objectives (Leica, PL APO, 250x / 0.95, 100x / 0.95, 50x / 0.90) for the measurements. There are more objectives available when large field of view becomes necessary (Leica, N PLAN 20x / 0.4) and for initially locating the region of interest on the substrate (Leica, PL FLUOTAR 5x / 0.15). The highest quality objectives used throughout this work are shown in Fig. 2.7.

(a) 50x (b) 100x (c) 250x

Figure 2.7 – Main high-magnification, high-numerical aperture apochromatic objectives used in this work. All objectives have apochromatic correction and achieve the highest free space numerical apertures.

All the microscope objectives we use are infinity corrected, meaning that the beam that exits from their exit pupil is collimated. This has the advantage that additional optical components can be inserted in the beam path without disturbing the imaging system, however an additional tube lens is needed to create the image of the object at the detector. This lens has unity magnification (1x) and long focal distance (200 mm) and, depending on the manufacturer, may be used to correct any residual aberrations of the objective. Its position is thus important, particularly for creating a plane wavefront in phase recordings. For that reason, the tube lens is mounted on a precision translation stage (Standa 8MT177-100) and, for every wavelength, the position that creates a plane wave-front on the detector (interference with the collimated reference arm) needs to be found. For the magnification of the objective to have the nominal value, the detector must be on the image plane of the tube lens, i.e. at a distance equal to the focal length of the tube lens; therefore, the tube lens and the camera are mounted on the same translation stage and move together.

When phase is not the recorded property, the residual wavefront errors do not affect the image formation and can be thus neglected. The chromatic aberrations are corrected by engineering the dispersion of the materials used in the objective and the tube lens, consequently their distance is not important, since transmission through those components is sufficient for chromatic aberration correction. As a result, for the intensity measurements, the position

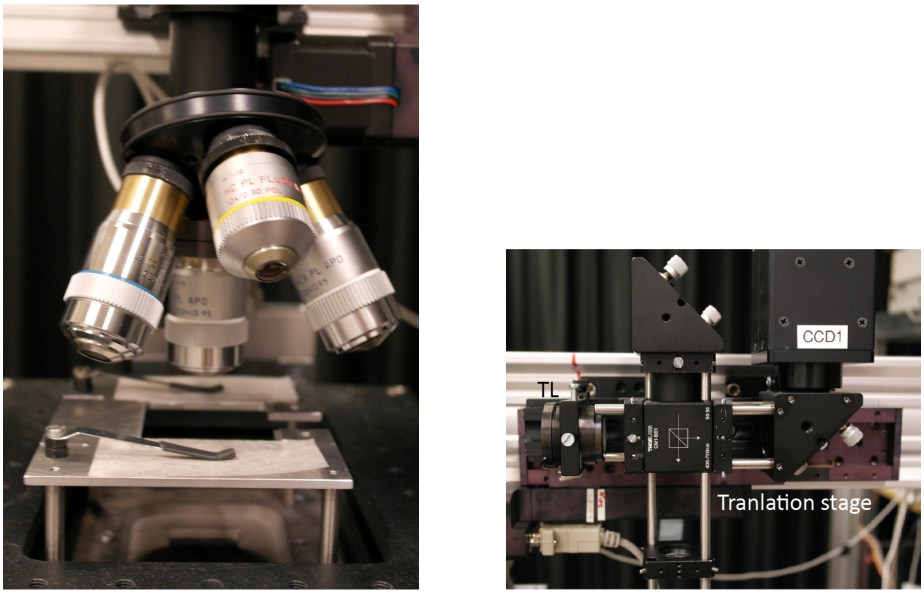

(a) Objective turret

(b) Tube lens and camera stage.

Figure 2.8 – (a): Turret that carries the objectives. (b): Tube lens that captures the output of the objectives and projects it on the CCD camera. the position of the tube lens is important only for the phase measurements.

of the tube lens is irrelevant, as long as it captures uniformly the whole image field (avoid vignetting). This is achieved by keeping the distance between the tube lens and the microscope objective below a limit that is suggested by the manufactures, which is done without any special care. The turret that carries all the objectives is shown in fig. 2.8a and the tube-lens – camera positioning configuration in fig2.8b.

Due to the high magnification of the objectives, the light collection capability is limited and the intensity that reaches the detector might be too low. In order to counteract this problem, we reduce the diameter of the beam, thus the intensity is confined tighter. Consequently, the power density of the illumination is increased; still, we want to approximate the resulting field with a plane wave. To achieve that, we use a long focal distance lens ($f = 500\,\mathrm{mm}$) to focus the light in the focal plane of the 100x and 250x objectives. The diameter of beam is reduced to $D \approx 2\,\mathrm{mm}$ by an aperture placed before the lens. This results in the lens having a numerical aperture of $NA = 2 \times 10^{-3}$ and it creates a (symmetric) beam waist of $W \approx 60\,\mu\mathrm{m}$ (full width at half maximum) at the focal plane, which is larger than the $20\,\mu\mathrm{m} \times 20\,\mu\mathrm{m}$ field of view of the (250x) objective. Moreover, the region of interest that we measure is typically only a small part of the total field of view, typically in the range from few micrometers (250x objective) to few tenths of micrometers (100x objective). Because of the weak focusing of the lens (long Rayleigh distance) and the fact the sample is in the focal plane, the phase of the illumination field is planar and its intensity uniform [8]; therefore, it can be regarded as a plane wave illumination. In the 50x objective case that has a much larger field of view (FoV$\approx 102\,\mu\mathrm{m} \times 102\,\mu\mathrm{m}$) we cannot use the long focal distance lens. Therefore we use an inverse beam expander (beam shrinker) to cancel the effect of the first beam expander and reduce the diameter of the beam again down to about 1 mm. The weak-focusing lens and the aperture are removed. Those components are pictured in Fig. 2.9.

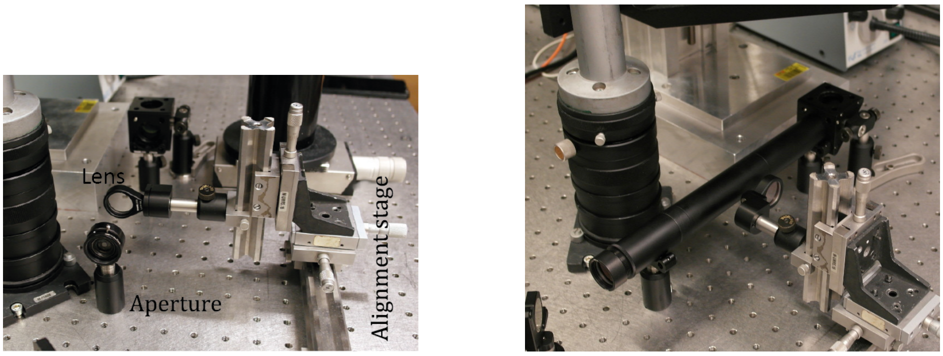

(a) Long focal distance lens

(b) Beam shrinker.

Figure 2.9 – (a): The lens weakly focuses the beam on the sample. (b): Inverse beam-expander, brings the beam diameter down to ≈ 1 mm. The purpose in both cases is to increase the power density of the beam.

The microscope objective and the sample are mounted on a piezo translator (MadCityLabs, MSL3786, 0.2 nm resolution and MSL1945, 1 nm resolution respectively), that allow to position the sample and fine tune the focusing of the imaging system. Additionally, by translating either stage, we can record the scattered field at different distance from the sample, with a nanometer precision, thus creating a fine volumetric representation of the measured quantity around the sample. Recording the full three dimensional electric field (intensity and phase) at any wavelength within the visible spectrum is a unique feature of this set-up that allows us to study the response of a wide variety of samples, as mentioned in the introduction. Both piezo stages are pictured in Fig. 2.10.

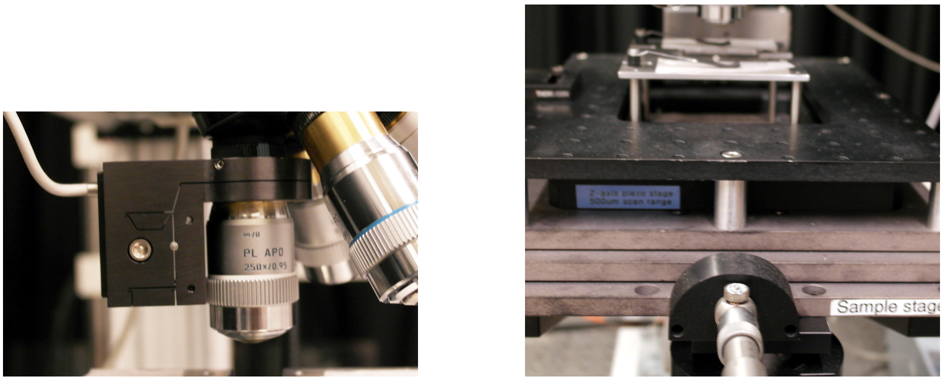

(a) Objective piezo stage

(b) Sample stage piezo stage.

Figure 2.10 – (a): Focusing block. (b): Sample piezo stage. Both stages allow fine-focusing and are used to record the field in a three-dimensional space around the sample.

2.2 Phase shifting interferometry

In order to demonstrate the phase extracting technique, let us assume a two-beam interference created by monochromatic light. Then, the intensity on each pixel (x, y) of the detector can be written as [9]:

$$I(x, y) = I_{\mathrm{dc}}(x, y) + I_{\mathrm{ac}}(x, y) \cos\big(\delta\phi(x, y) + \phi(t)\big), \tag{2.1}$$

where the first term of the sum, $I_{\mathrm{dc}} = I_{\mathrm{ref}} + I_{\mathrm{obj}}$, is the constant, non-interference term of the intensity, the second term, $I_{\mathrm{ac}} = 2(I_{\mathrm{ref}} I_{\mathrm{obj}})^{1/2}$, is the intensity that is modulated due to the interference, $\delta\phi(x, y) = \phi_{\mathrm{ref}} - \phi_{\mathrm{obj}}$ is the phase difference between the two arms at the given pixel position (x, y) and $\phi(t), t = 0...k$ is the phase difference added by translating the piezo mirror. In this equation, the intensities I and the phase difference $\delta\phi$ are unknown, so we need at least three interferograms $t = 0...2$ to fully solve the system. Increasing the number of the recorded interferograms overdetermines the system, making the solution more robust against errors in the induced phase difference $\delta\phi(t)$. We record five instances of the interference pattern, increasing in a step-wise manner the induced phase $\phi(t), t = 0...4$ by $\pi/2$ (90° or $\lambda/4$). This algorithm is known as *Schwider-Hariharran* or five-steps phase shifting interferometry [7], and the solution for the phase difference is:

$$\delta\phi = tan^{-1}\left[\frac{2(I_2 - I_4)}{2I_3 - I_5 - I_1}\right], \tag{2.2}$$

where tan^{-1} is four-quadrant inverse tangent function and I_{k} is the recorded intensity of the interference pattern. This method generates the phase map on each pixel individually, which makes it insensitive to intensity variations across the detector that may arise from pixel response non-uniformity or illumination distribution. Figures 2.11(a)-(e) show the five recorded intensity pattern of the interference of two plane waves at $\lambda = 500\,\mathrm{nm}$. The optical path of reference arm of each interferogram is increased by $\lambda/4$ compared to the previous measurement. Figure 2.11(f) shows the resulting phase map. Please note that the output of the algorithm is bounded within the $(-\pi, \pi]$ interval and needs to be unwrap to find the actual phase values. The unwrapping process will be analyzed in the following section. It has to be pointed out that, in order to induce the phase difference, the mirror is translated by $\lambda/(4\sqrt{2})$ for every interferogram, since it makes an angle of 45° with the propagation axis. This also displaces the beam propagating along the reference arm laterally; however the displacement can be ignored because it is negligible and does not affect the phase result. During the intensity recording, the reference arm is totally blocked since we only need the intensity transmitted through the sample, captured by the object arm, so the position of the optical delay line and the piezo mirror are irrelevant.

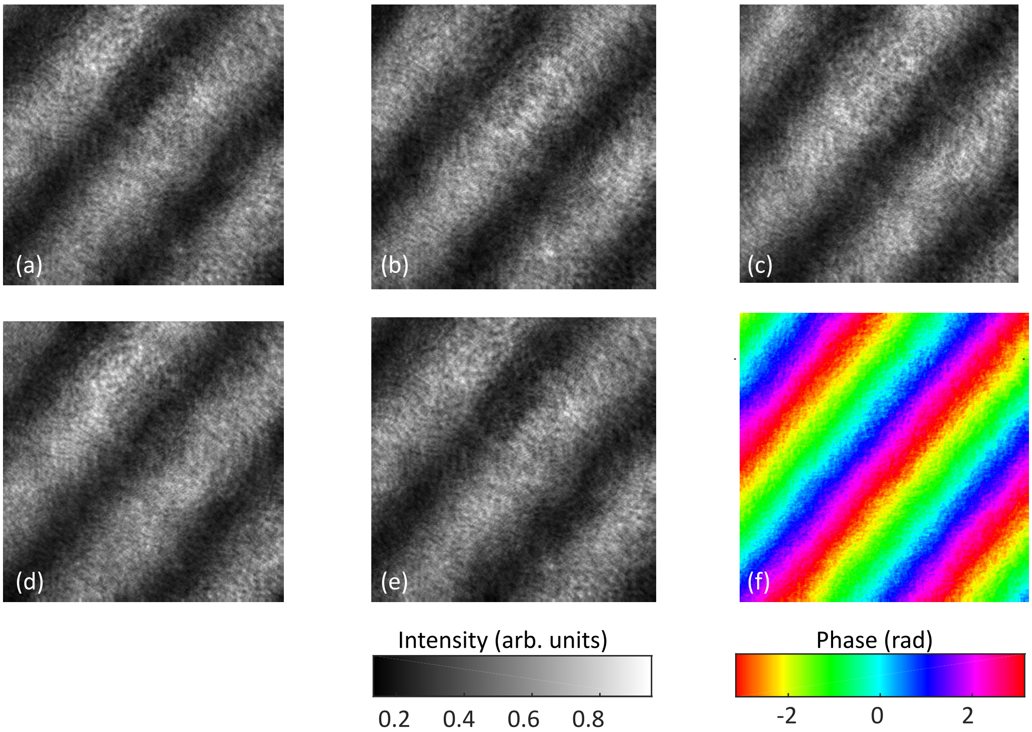

Figure 2.11 – Example of the five steps algorithm. (a)-(e): Interference pattern of two plane waves at $\lambda = 500\,\text{nm}$, as the piezo mirror changes the optical path of the reference arm by $\lambda/4$. (f): Resulting phase map given by eq. 2.2.

2.3 Data extraction

The images recorded by the instrument represent pixel values, e.g. how much energy is impinging on the cross-section of the pixel during the integration time. Calculating the value of the energy requires the knowledge of specific parameters of the camera (quantum efficiency, sensitivity) that are not known with sufficient accuracy and anyhow it is not the purpose of the measurements. We want to record the profile of the field, so it is sufficient to have a linear relation between the recorded value and the energy of the field. This is ensured by avoiding saturation and recording all values at a single wavelength with the same integration time and amplification (gain). In order to compare results obtained at different wavelengths, we apply a normalization process (along with additional processing) that will be explained in detail in the next section. As long as the linearity between the strength of the field and the pixel value is valid, analyzing the intensity data is straight forward.

The situation for the phase extraction however, is different. As indicated by eq. 2.2, the phase is extracted from five intensity images (recorded with the conditions stated above), by the tan^{-1} operator (wrapping operator) whose output is bound within the $(-\pi, \pi]$ interval. We can thus write the recorded phase, restricting to the one dimensional case as:

$$\psi(n) = \mathscr{W}\{\phi(n)\} = \phi(n) + 2\pi k(n), \quad n = 0, 1, \ldots, N-1, \tag{2.3}$$

where $\phi(n)$ is the actual phase, ψ is the wrapped (measured) phase, $\mathscr{W}$ is the wrapping operator, $k(n)$ is an array of integers chosen so that

$$-\pi < \psi(n) \leq \pi, \tag{2.4}$$

and N is the number of pixels. Defining the difference operator Δ as:

$$\begin{aligned} \Delta\phi(n) &= \phi(n+1) - \phi(n), \\ \Delta k(n) &= k(n+1) - k(n), \quad n = 0, 1, \ldots, N-2, \end{aligned} \tag{2.5}$$

it can be shown that the actual phase ϕ can be retrieved from [10]:

$$\phi(m) = \psi(0) + \sum_{n=0}^{m-1} \mathscr{W}\{\Delta\{\psi(n)\}\}. \tag{2.6}$$

The meaning of eq. 2.6 is that the phase can be unwrapped by summing (integrating) the wrapped differences of the measured phase *(Itoh's method)*. It is very important to note however, that this formula was derived under the assumption that:

$$-\pi < \Delta\{\phi(n)\} \leq \pi. \tag{2.7}$$

This condition can be violated if the signal is aliased or the recording has low signal-to-noise ratio (≈ 2), in which cases unwrapping cannot predict the actual phase [11].

Studying the problem for the continuous two-dimensional case, the actual phase at every position can be written as:

$$\phi(\boldsymbol{r}) = \int_C \nabla\psi \cdot d\boldsymbol{r} + \psi(\boldsymbol{r_0}), \tag{2.8}$$

where C is any path that connects the points $\boldsymbol{r_0}$ and $\boldsymbol{r}$ and $\nabla\psi$ is the gradient of ψ. It is known that the value of a line integral

$$I = \int_C \boldsymbol{F}(\boldsymbol{r}) \cdot d\boldsymbol{r} \tag{2.9}$$

depends, generally, not only on the starting and ending points, but on the path C along which the integration is calculated. This, however, cannot be true, since the phase value of the field that we measure is unique. In order for the integral to be independent of the chosen path, the following condition is sufficient:

$$\oint \boldsymbol{F}(\boldsymbol{r})\cdot d\boldsymbol{r} = 0, \tag{2.10}$$

in other words, the integral of $\boldsymbol{F}(\boldsymbol{r}) = \nabla\psi$ around any simple closed path is zero. As it was explained previously, the output of our instrument is two dimensional array of the wrapped phase $\psi(m,n)$ in every pixel position m,n. The shortest closed path is 2×2 window. In order to look for positions that can potentially corrupt the phase unwrapping process, we create the wrapped phase derivative map by:

$$\begin{aligned}
\Delta_1 &= \mathscr{W}\{\psi(m,n+1)-\psi(m,n)\},\\
\Delta_2 &= \mathscr{W}\{\psi(m+1,n+1)-\psi(m,n+1)\},\\
\Delta_3 &= \mathscr{W}\{\psi(m+1,n)-\psi(m+1,n+1)\},\\
\Delta_4 &= \mathscr{W}\{\psi(m,n)-\psi(m+1,n)\}.
\end{aligned} \tag{2.11}$$

If the value of:

$$q = \frac{1}{2\pi}\sum_{i=1}^{4}\Delta_i \tag{2.12}$$

is non-zero, eq. 2.10 does not hold and the position that is encircled by this path (as convention we choose the upper left element $\psi(m,n)$) is called phase residue [12, 13]. The sign of q is the polarity or charge of the residue. In most practical case, the absolute value of $|q| = 1$, which means the along the closed path C, the phase changes by 2π. Higher values mean that the phase accumulated around this point is a multiple of 2π (multiple phase wrapping), that only happens to pathological case though. Those points are related to zeros of the complex function from which the phase was extracted and they are commonly referred to as phase singularities or optical vortexes [14, 15]. We will study them in a later chapter of this work, this part however, sets the methods to detect them. Apart from the actual signal that might create the singularities, phase residues can arise from phase-discontinuities, noise and aliasing.

Since we can identify those problematic points, we can choose appropriate paths to unwrap the phase and balance out those residues. A method that implements this approach is the *Goldstein's branch cut algorithm* [16], that is used in this work. The Matlab code to implement this algorithm was written by Bruce Spottiswoode [17].

A different approach for phase unwrapping relies on finding a phase map that has the minimum distance form the recorded (wrapped) phase values in an L^p- norm sense. For continuous functions, this can be expressed as:

$$J = \epsilon^p = \iint f(\phi_x, \phi_y, x, y)\delta x \delta y, \tag{2.13}$$

where f is

$$f = |\phi_x - \psi_x|^p + |\phi_y - \psi_y|^p, \tag{2.14}$$

where the subscript denotes derivation along the respective axis. When $p = 2$, this becomes the least square error minimizing problem and is reduced to solving the Poisson's equation

$$\nabla^2 \phi = \rho, \tag{2.15}$$

where $\rho = \psi_{xx} + \psi_{yy}$. In this work we use a phase unwrapping method based on weighted and unweighted least-square method from *Ghiglia and Romero* [18] that solves the Poisson's equation in the discrete domain, using a discrete cosine transform (DCT) method. The Matlab code that implements this process was writtern by Muhammad F. Kasim [19]. Figure 2.12 shows, in blue, the phase map extracted in Fig. 2.11(f) along the diagonal (lower right to upper left corner) and in red the unwrapped phase. The wrapped profile is bound within the $(-\pi, \pi]$ range and has discontinuities, while unwrapping the phase restores the continuity of the phase. The unwrapping was done using the unweighted least-square-error algorithm.

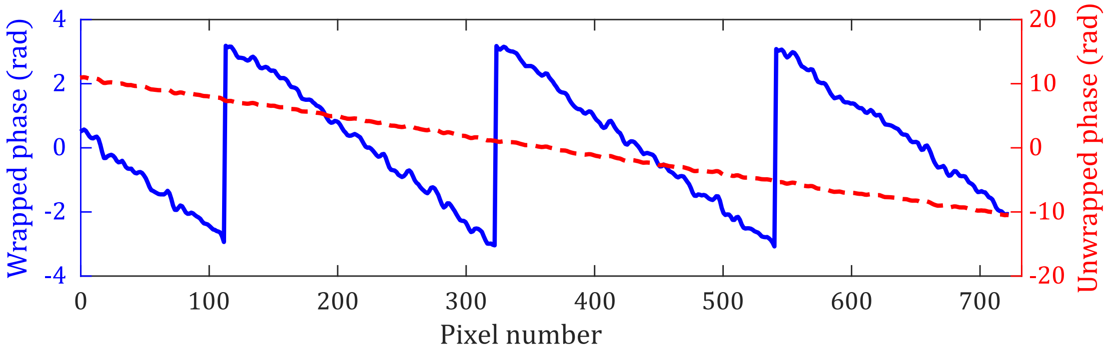

Figure 2.12 – Wrapped (blue) and unwrapped (red) phase profile. The wrapped profile is bounded within the $(-\pi, \pi]$ interval and has discontinuities. Unwrapping the phase gives us the actual value and restores the continuous profile.

2.4 Data recording and processing

This section summarizes the procedure that was followed to record the data and, when necessary, to process them. The aim of the procedure is to ensure the quality of the measurements by respecting the conditions mentioned in sec. 2.3. Usually, the data were post-processed before being used for analysis in order to suppress features that are coming from the background and bias resulting from the set-up.

2.4.1 Intensity

With the reference arm blocked, we only need to take care not to saturate the detector and set the shortest exposure time and lowest gain that allow high signal-to-noise ratio measurements for every wavelength. Having guaranteed those conditions, we record the intensity that is transmitted through the sample under study, either on a single plane or along the propagation axis z, depending on the measurement. After recording the intensity profile with the sample mounted, we remove it and take a single image of the background profile. For the post-processing part, we normalize every recorded image with its mean value (excluding outliers), so all images have the same mean (namely 1) and comparable range of values for different wavelengths. Next, we subtract the normalized background image from every normalized data image. Figure 2.13(a) shows a normalized image of the sample studied in Ch. 4, where a gradient in the illumination field is observed. Next, we record and normalize a background image, without the sample, as shown in Fig. 2.13(b), where the same gradient is present. Taking the difference of the two images, shown in Fig. 2.13(c), produces a more uniform image where the features of the sample are more clearly visible.

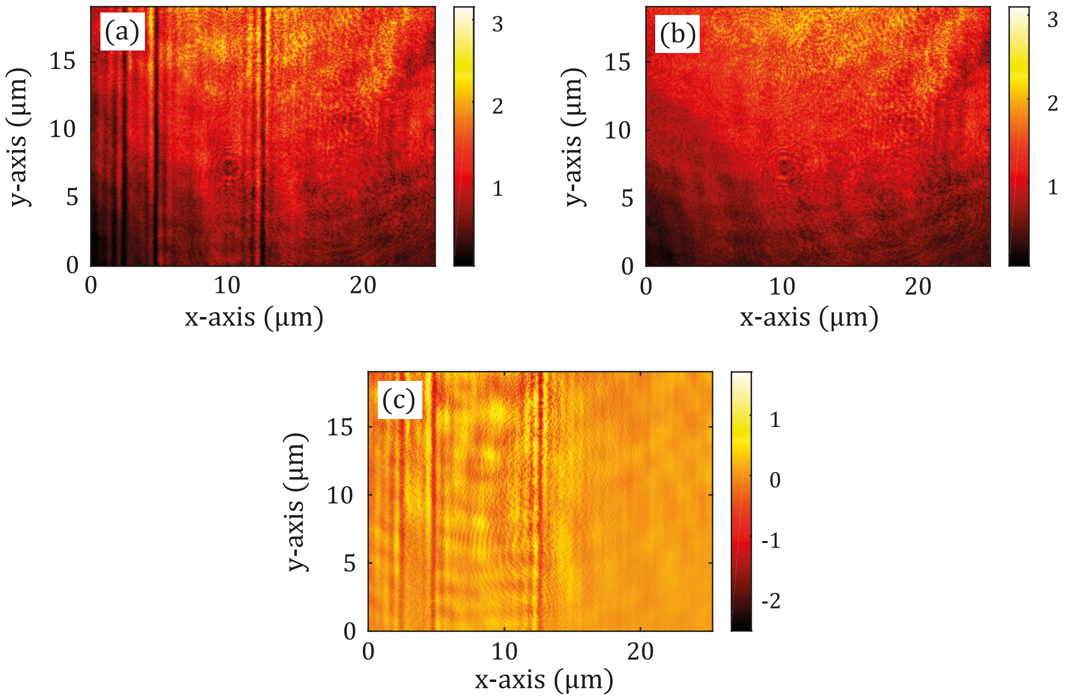

Figure 2.13 – Intensity data post processing. (a): Normalized sample data. (b): Normalized background data. (c): Their difference

This process is derived from the *Through the focus Scanning Optical Microscopy* (TSOM) technique [20, 21] and compensates illumination irregularities and different pixel response and highlights the signal from the background. This processing method results to some pixels acquiring negative values, which should be regarded as the difference from the background image. For the sake of simplicity though, we refer to those processed data as *Intensity* measurements.

2.4.2 Phase

In order to run the phase measurements, we first identify the position of the optical delay line that gives the maximum fringe contrast and the position of the tube lens that produces straight fringes, for the reasons explained in sec. 2.1. This is done for every wavelength for which we record the phase profile. Next, we align the beams of the reference and object arms, so as to produce a single fringe on the detector and five intensity images are recorded, according to the five-steps phase shifting interferometry technique [7]. Again, we take care not to saturate the detector at any of the five images and fix the exposure time. Once the phase profile of the sample is recorded, we record and extract the phase profile of the background. In some cases, the extracted phase maps are filtered using a 5×5 averaging window. Every extracted phase map is subsequently unwrapped, which removes the phase wrapping that arise from the angle between the two interfering beams not being equal to zero. Then, the background phase map is subtracted from the one of the sample and rewrapped in the $(-\pi, \pi]$ interval. The purpose of this rewrapping is to correct any artificial phase-jumps; given that the phase signature of the samples is small, it is very rare to have such phase-jumps after the subtraction of the background. This step has small impact on the final results and is mainly a final safeguard against problematic points created during the previous steps of data-processing. The result is the phase that is induced only by the sample and not from the set-up itself.

Figure 2.14 gives an example of this procedure. Figure 2.14(a) shows the unwrapped phase map of sample shown in the intensity section, where phase variations in regions where the phase should be constant are observed. Next we extract and unwrap the phase map of the background (no sample), as shown in Fig. 2.14(b). From this image we see that the variations observed earlier are also visible in the background. Finally, we subtract these two images and re-wrap the phase difference in the $(-\pi, \pi]$ interval. The result is shown in Fig. 2.14(c), which is again more uniform and highlights the features of the sample. This procedure suppresses any bias or systematic error that comes from the set-up itself, such as a differential response of the pixels on the detector or deviations from a plane wavefront in the incident illumination.

2.4.3 Three dimensional measurement

The benefits of the data processing are better demonstrated on measurements that capture multiple images along z axis and when the useful signal becomes weak. Figure 2.15 shows such an example of a sample studied in Ch. 6. It is a gold nano-particle of diameter $D = 300\,\text{nm}$

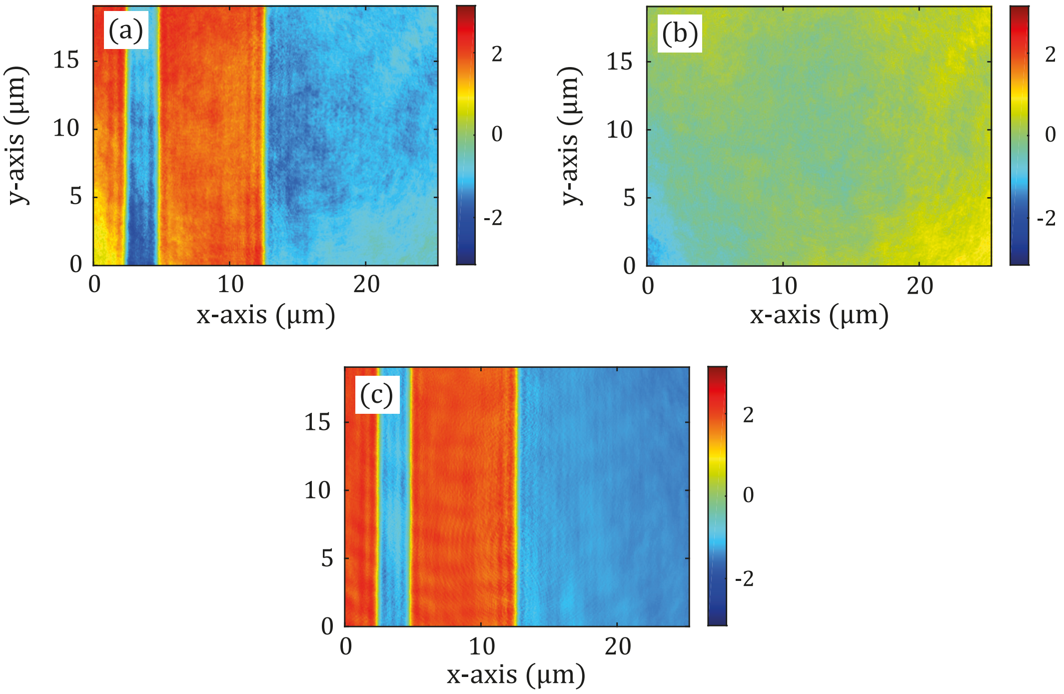

Figure 2.14 – Phase data post processing. (a): Unwrapped phase map of the sample. (b): Unwrapped phase map of the background. (c): Their re-wrapped difference.

illuminated by $\lambda = 600\,\mathrm{nm}$. The intensity and phase data are recorded at several distances along the z-axis (propagation direction). The three-dimensional volumetric representation of the field is created by stacking the recorded images on top of each other. The aforementioned processes are applied to every z-slice and subsequently, a single line was used to create the cross-section. The resulting $x - z$ plane goes through the center of the nano-particle.

It is evident that the background on the camera, appearing here as vertical lines, is considerably suppressed and the self-correlation of the phase values along the z-axis is restored. A final comment should be made on Fig. 2.15(d), where the longitudinal differential phase is plotted. This image shows the phase difference between the measurement and a constant reference (background phase), consequently the advancement of phase due to propagation is not shown. However, the phase accumulated by propagation along z axis in air is given by $2\pi/\lambda z$, and the propagation effect can be restored by enforcing the referential phase to advance accordingly. For visualization purpose the phase values are wrapped along the propagation axis, creating the propagating phase maps that appear in later chapters.

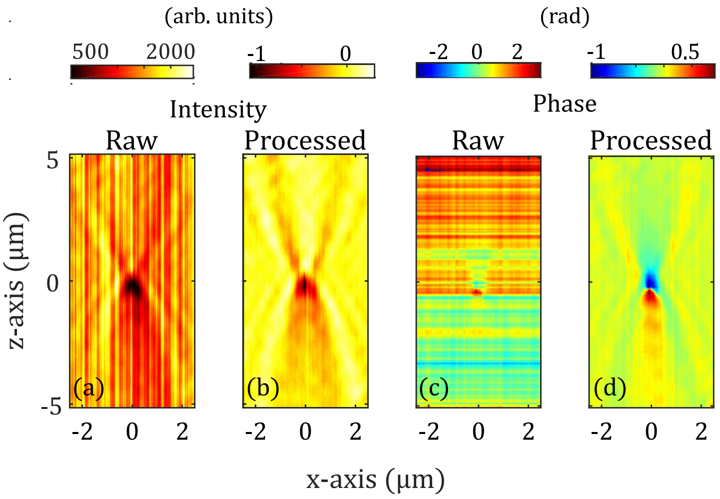

Figure 2.15 – (a)-(b): Comparison between raw and processed data for intensity and (c)-(d) phase. The sample under study is a gold nanoparticle of diameter $D = 300\,\text{nm}$, illuminated by a plane wave at $\lambda = 600\,\text{nm}$. The images show the cross-section in the $x-z$ plane through the center of the particle.

Bibliography

[1] Carsten Rockstuhl, Iwan Marki, Toralf Scharf, Martin Salt, Hans Peter Herzig, and Rene Dändliker. High resolution interference microscopy: a tool for probing optical waves in the far-field on a nanometric length scale. *Current Nanoscience*, 2(4):337–350, 2006.

[2] Myun-Sik Kim, Toralf Scharf, and Hans Peter Herzig. Small-size microlens characterization by multiwavelength high-resolution interference microscopy. *Optics Express*, 18(14):14319–14329, July 2010.

[3] Myun-Sik Kim, Toralf Scharf, Stefan Mühlig, Carsten Rockstuhl, and Hans Peter Herzig. Engineering photonic nanojets. *Optics express*, 19(11):10206–10220, 2011.

[4] Myun-Sik Kim, Toralf Scharf, Stefan Mühlig, Carsten Rockstuhl, and Hans Peter Herzig. Gouy phase anomaly in photonic nanojets. *Applied Physics Letters*, 98(19):191114, 2011.

[5] Ashish Arora and Sandip Ghosh. A twisted periscope arrangement for transporting elliptically polarized light without change in its polarization state. *Review of Scientific Instruments*, 81(12):123102, December 2010.

[6] Max Born and Emil Wolf. *Principles of Optics*. Cambridge University Press, seventh (expanded) edition, 1999.

[7] P. Hariharan, B. F. Oreb, and T. Eiju. Digital phase-shifting interferometry: a simple error-compensating phase calculation algorithm. *Applied Optics*, 26(13):2504–2506, July 1987.

[8] Sidney A. Self. Focusing of spherical Gaussian beams. *Applied optics*, 22(5):658–661, 1983.

[9] Eric P. Goodwin and James C. Wyant. *Field Guide to Interferometric Optical Testing*. SPIE Field Guides. SPIE, 2006.

[10] Kazuyoshi Itoh. Analysis of the phase unwrapping algorithm. *Applied Optics*, 21(14):2470–2470, July 1982.

[11] Dennis W. Ghilia and Mark D. Pritt. *Two-Dimensional Phase Unwrapping Theory, Algorithms and Software*. John Wiley & Sons, Inc., 1998.

[12] J. M. Huntley and J. R. Buckland. Characterization of sources of 2π phase discontinuity in speckle interferograms. *Journal of the Optical Society of America A*, 12(9):1990–1996, September 1995.

[13] J. M. Huntley. Noise-immune phase unwrapping algorithm. *Applied Optics*, 28(16):3268–3270, August 1989.

[14] P. Coullet, L. Gil, and F. Rocca. Optical vortices. *Optics Communications*, 73(5):403–408, November 1989.

[15] N. R. Heckenberg, R. McDuff, C. P. Smith, and A. G. White. Generation of optical phase singularities by computer-generated holograms. *Optics Letters*, 17(3):221–223, February 1992.

[16] Richard M. Goldstein, Howard A. Zebker, and Charles L. Werner. Satellite radar interferometry: Two-dimensional phase unwrapping. *Radio Science*, 23(4):713–720, July 1988.

[17] Bruce Spottiswoode. 2d phase unwrapping algorithms. https://ch.mathworks.com/matlabcentral/fileexchange/22504-2d-phase-unwrapping-algorithms.

[18] Dennis C. Ghiglia and Louis A. Romero. Robust two-dimensional weighted and unweighted phase unwrapping that uses fast transforms and iterative methods. *Journal of the Optical Society of America A*, 11(1):107–117, January 1994.

[19] Muhammad F. Kasim. 2d weighted phase unwrapping. https://ch.mathworks.com/matlabcentral/fileexchange/60345-2d-weighted-phase-unwrapping.

[20] Ravikiran Attota, Thomas A. Germer, and Richard M. Silver. Through-focus scanning-optical-microscope imaging method for nanoscale dimensional analysis. *Optics Letters*, 33(17):1990–1992, September 2008.

[21] Ravikiran Attota and Richard Silver. Nanometrology using a through-focus scanning optical microscopy method. *Measurement Science and Technology*, 22(2):024002, December 2010.

3 New approach for microlens characterization

3.1 Statement of the problem

Microlenses and microlens arrays are crucial components of many high-end devices and they are being adopted into increasingly more fields. They are used in from well-establish configurations, like fiber coupling, to custom illumination devices, like mask-aligners, where performance is of utmost importance [1]. This wide integration has been facilitated by the multitude of fabrication techniques and their constant improvement [2, 3]. Advances in fabrication technology however, goes hand in hand with progress in the characterization and quality assurance fields, since providing insightful feedback for fabrication and performance inconsistencies is crucial for a steady improvement.

There are two main approaches towards those ends; one, which can be termed as physical characterization, aims to measure some geometrical quantities of the microlens, like the radius of curvature or the surface roughness. Widely used techniques to extract that information include optical profilers (e.g. confocal microscopes, coherence scanning interferometry) [4, 5, 6] or mechanical ones (e.g. stylus profilometers). The second approach, which can be described as optical characterization, focuses on evaluating the optical properties of such lenses, like the intensity distribution around the focal spot [7], or the wavefront shaping functionality of the lens. Common techniques of this type include various interferometers, Shack Hartman sensors or point spread function measurements.

All the above-mentioned approaches are well suited for microlenses that have a low numerical aperture and asphericity [8]. As those parameters (numerical aperture, asphericity) increase, they collide with the capabilities of the microscope objectives that can image only a small area, as their numerical aperture (and generally the magnification) increases. This is graphically represented in Fig. 3.1, where we plot the numerical aperture values (and the corresponding magnification) of the objectives we use against the typical field of view achieved by those objectives. The measuring process is meaningful only when the numerical aperture of the microscope objective is larger than that of the examined lens; however, high-performance microlenses lie within the graded area of Fig. 3.1, since they have an increased numerical

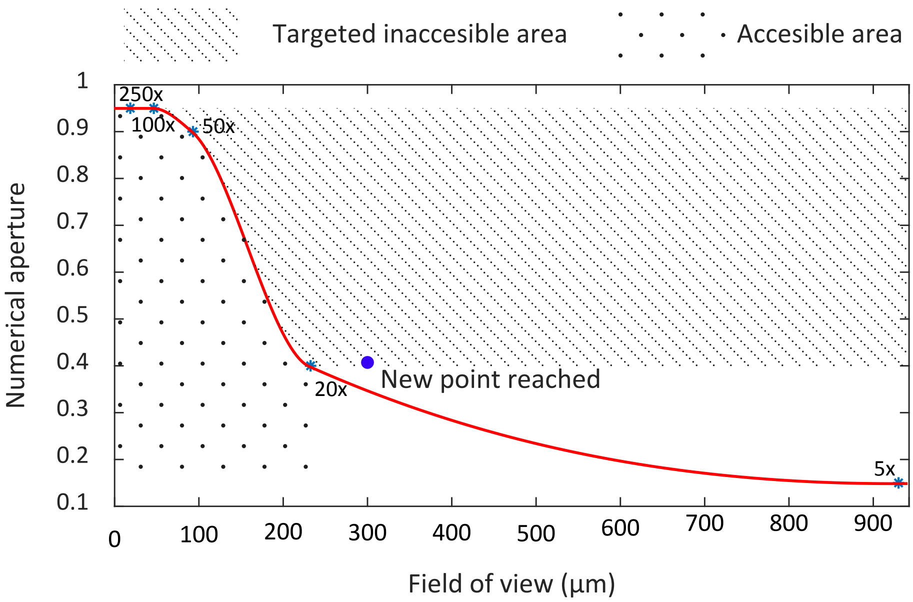

Figure 3.1 – Indicative curve showing the numerical aperture (and the corresponding typical magnification) against the field of view. High performance microlenses can be measured within the area indicated by the dense dots, i.e. with high numerical aperture and a reasonable field of view. The microscope objectives however are better utilized in the sparsely dotted area. Unfortunately, those two regions do not overlap and a workaround is the topic of this chapter. The isolated dot indicates the new point reached by a new method.

aperture and a typical size of few hundreds of micrometers. Therefore, the microscope objective necessary to perform a valid measurement on such a microlens cannot image the whole surface, due to the reduced field of view. Conventional profilometers as well, cannot extract the actual profile of such microlenses, since their edges are too steep. The main goal of this chapter is to solve the conflict between precision and size by utilizing high numerical aperture microscope objectives to carry out the characterization of microlenses at cleverly chosen planes. The idea is explained in more detail below.

We introduce two concepts that are schematically shown in Fig. 3.2 and can be described in the following manner: measuring at the surface of the lens requires the largest field of view, however the intensity at that plane is very uniform. Therefore, we can use low numerical aperture objectives to capture the whole lens, at the cost of reduced lateral resolution, which means that fine features are missed. This can be understood by envisioning the plane waves transmitted through a microlens; they will propagate at large angles, if the numerical aperture is high, thus creating a dense fringe pattern that cannot be resolved by the microscope objective. If this is not the case however, extracting the profile of the lens at this plane is straightforward. Going at the focal plane on the other hand, has the advantage of tight confinement of light, thus small field of view is required and the use of high numerical aperture objective is possible; the dynamic range at this plane needs to be very high (orders of magnitude), making the measurements challenging. Additionally, linking the focal spot to the surface of the lens is very strenuous and can lead to large deviations from the actual surface, since it is a highly complicated reverse-solving problem.

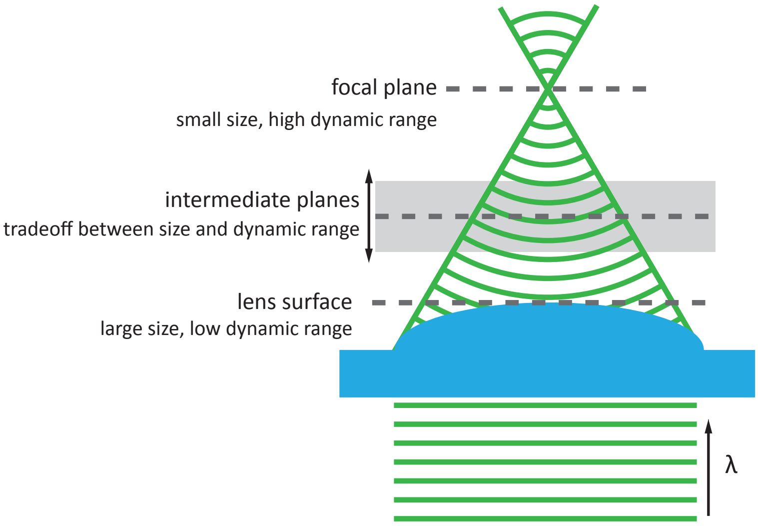

Figure 3.2 – Schematic of the measuring concept. As light passes through the microlens, it is focused at the focal plane. Usually, measurements are run either at the surface of the lens (requires large field of view, but surface reconstruction is straightforward) or at the focal plane (the tight spot size allows high numerical aperture objectives, but the surface reconstruction gets complicated). In this chapter, we investigate the benefits of measuring at an intermediate plane.

As we go from one extreme to the other, there are many intermediate planes, where the trade off between required filed of view and light confinement changes, thus it is expected that at some plane we can use high numerical aperture objectives to measure fields that are relatively uniform and can be used to precisely reconstruct the surface of the lens. Referring again to Fig. 3.1, we use objectives that have high numerical aperture, but instead of capturing the whole surface of a lens, we capture only a part of it and estimate the rest. In order to do that however, we have to rely on models describing the effect of the microlens onto the incoming field, as well as the assumptions they require.

Before we go into the details of the proposed solution however, we present a technique for the characterization of low numerical apertures microlenses using intensity measurements around the focal spot. This will demonstrate the usefulness of the set-up, strengthen its proper functionality and help us explain why some techniques are not applicable to microlenses with a high numerical aperture. Next, we will demonstrate the simple solution, termed *intermediate plane measurement*, to overcome those difficulties, and provide the most complete characterization of microlenses. It should be highlighted that a great portion of this study is attributed to Jeremy Bégueling, who handled all the simulations and the measurements that were not carried out by the interferometric set-up and also provided most of the images shown hereafter.

3.2 Conventional focal spot measurement

We present first the information that can be extracted from the intensity measurement around the focal spot of a low numerical aperture (0.13) plano-convex microlens. The material of the lens is fused silica and is fabricated using photolithography and reactive ion etching. The lens is geometrically characterized by its diameter, which is $D = 240\mu\text{m}$ and its radius of curvature that is $ROC = 424.5\mu\text{m}$. The refractive index of fused silica is $n \approx 1.45$ within the visible range (the exact numbers are given when necessary). Regarding the measurements, we first locate the position of the rim of the lens and then we translate the sample stage, until the focal plane of the microlens approximately coincides with that of the microscope objective. Then, the intensity distribution within a length of $z = 200\mu\text{m}$ is recorded, using a step size of $\Delta z = 250\,\text{nm}$, which is sufficient for intensity measurements. We use an apochromatic 100x microscope objective with a numerical aperture of $NA = 0.95$. The result of such a measurement is shown in Fig. 3.3, where the illuminating wavelength is $\lambda = 800\,\text{nm}$. The highly symmetric shape with respect to both axis x and z indicates low aberrations and an almost diffraction limited performance.

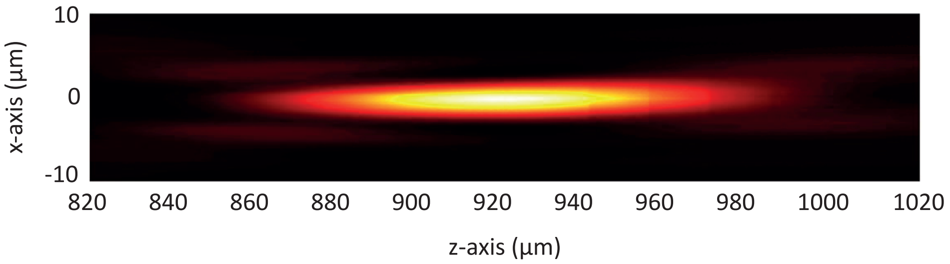

Figure 3.3 – Intensity distribution around the focal plane when a plano-convex microlens is illuminated by $\lambda = 800\,\text{nm}$. The high symmetry of the shape indicates an almost diffraction limited performance.

3.2.1 Focal length and Strehl ratio

The information contained in the measurement is related to the focusing capabilities of the microlens. By plotting the cross-section along z axis for $x = 0\mu\text{m}$, we can identify the focal length and depth of focus, as shown in Fig. 3.4(a). The focal length is identified as the position along the z axis where the intensity acquires its maximum value; in this case it is found $f = 918\mu\text{m}$. The focal length is related to the radius of curvature of the microlens by the formula:

$$f = \frac{ROC}{(n-1)} - h, \tag{3.1}$$

where n is the refractive index of the material of the lens and h is its sag height. The parameters mentioned above lead to the theoretical value of $f = 919.7\mu\text{m}$, which agrees well with the measured value. The depth of focus is defined as the width within which the intensity value is $I \geq 80\%$ of the maximum value [9]. In this case, it is found $DOF_m = 46\,\mu\text{m}$, which is reasonably close to the $DOF_s = 48\,\mu\text{m}$, predicted by simulations.

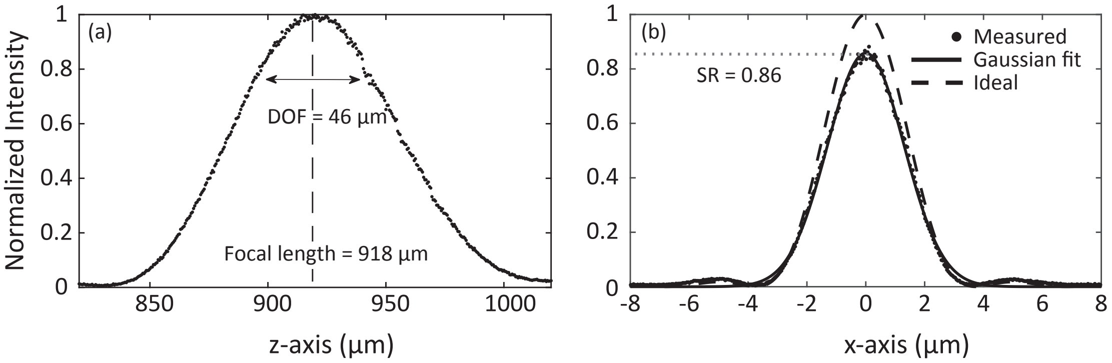

Figure 3.4 – Information extracted by the intensity measurements around the focus: (a) Focal plane ($I = I_{max}$) and depth of focus ($I \geq 80\% I_{max}$). (b): Strehl ratio ($I_{max}^{real}/I_{max}^{ideal}$). Those are the most frequent metrics to asses the quality and performance of lenses.

The cross-section along x on the focal plane ($z = 918\,\mu\text{m}$) can be used to extract the Strehl ratio (SR) of the optical component, which is the most frequently used metric for assessing optical quality. It is defined as the ratio of the maximum measured intensity over that of an ideal system [9] and is given by:

$$SR = \frac{max\{I_{meas}\}}{P_0 \pi \frac{\alpha^2}{\lambda^2 f^2}}. \tag{3.2}$$

Essentially, the denominator is the intensity I_0 in the center of the far-field diffraction pattern of a circular aperture. In this case, α is the radius of the microlens, λ is the illumination wavelength, f is the focal length and P_0 is the total power incident on the camera. We consider $P_0 = 1\,\text{W}$, since we normalize the data. The comparison between the measured and the ideal system is shown in Fig. 3.4(b), where a Strehl ration of $SR = 0.86$ is calculated; this value qualifies this microlens as diffraction limited according to the Maréchal criterion [9].

3.2.2 Chromatic behavior

A novel feature of our experimental set-up is the spectral selectivity, i.e. the ability to run measurements at different wavelengths. This feature is what we utilize in the section to investigate the chromatic behavior of the lens. The performance of the lens depends, among other things, on its refractive index; thus the dispersion of fused silica is responsible for the different behavior at different wavelengths. We illuminate the microlens at the wavelengths

$\lambda = 500\,\text{nm}$, 650 nm and 800 nm where the refractive index of fused silica is $n = 1.4623$, 1.4565 and 1.4533 respectively [10]. The relevant measurements are shown in Fig. 3.5(a) - 3.5(c) for the three wavelengths, respectively.

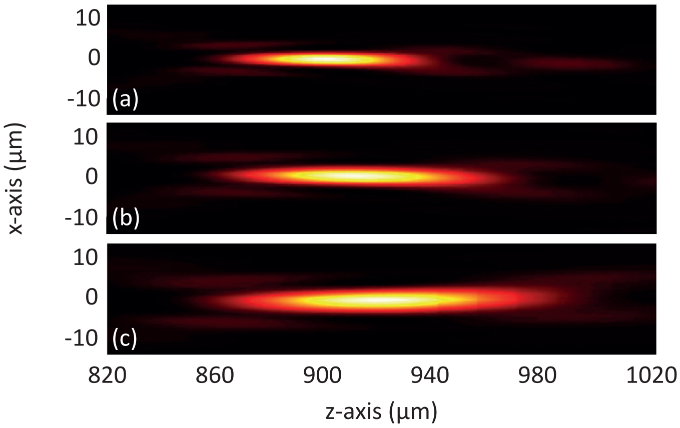

Figure 3.5 – Intensity measurements around the focus for the wavelengths: (a) $\lambda = 500\,\text{nm}$, (b) $\lambda = 650\,\text{nm}$ and (c) $\lambda = 800\,\text{nm}$. The field propagates towards increasing z values. As the wavelength increases, the focal plane (brightest spot) shifts to larger z values.

As was done in the previous section, we use those measurements to extract the focal plane and the Strehl ratio, as shown in Fig. 3.6(a) and 3.6(b).

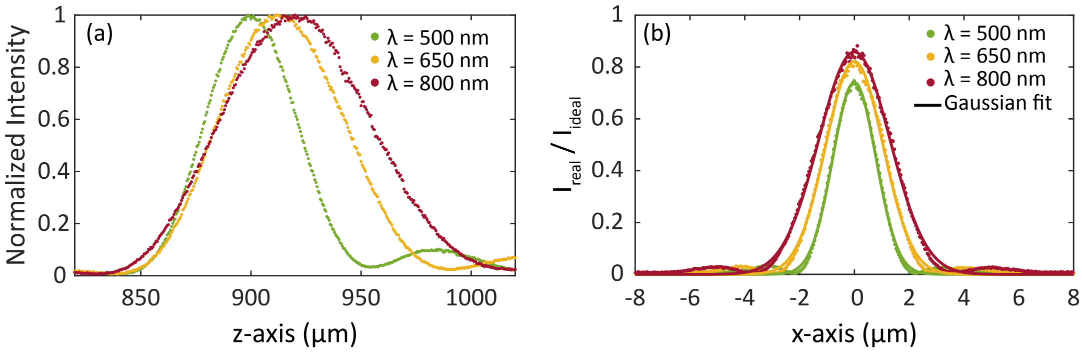

Figure 3.6 – Intensity measurements at the wavelengths $\lambda = 500\,\text{nm}$, 650 nm and 800 nm. (a) Focal length. The peak of the curve, indicating the focal plane, is shifted towards greater z values for longer wavelengths. (b) Strehl ratio. The Gaussian fit approaches the maximum value of 1, which is the ideal value, as the wavelength increases. The measured values agree very well with those predicted by the model and measurements carried out with established techniques (confocal microscopy).

According to eq. 3.1, there is a shift in the focal length position of about $\Delta f \approx 20\,\mu\text{m}$, when the illumination wavelength changes from $\lambda = 500\,\text{nm}$ to $\lambda = 800\,\text{nm}$ [11]. This shift can be seen both in Figs. 3.5 and 3.6(a) as the displacement of the maximum intensity position.

Regarding the Strehl ratio, which is shown in Fig. 3.6(b) for different wavelengths, it can expressed as a function of the wavelength by the formula [9]:

$$SR \approx e^{-\frac{4\pi^2}{\lambda^2} n^2 \Delta z^2}, \tag{3.3}$$

where Δz is the root meas square value of the surface deviation compared to the ideal one. Equation 3.3 shows that the Strehl ratio converges to unity for longer wavelengths, as is indicated in Fig. 3.6(b) as well. The accuracy of those approximations however should be discussed in detailed to better understand when they are applicable and what do they physically mean; with that in mind, we cannot deduce that the lens becomes aberration-free for longer wavelengths, which is the physical interpretation of Strehl ratio. The surface of this particular lens was measured, for comparison purposes, with a confocal microscope, and this measurement showed a deviation of the ideal surface of 32 nm. This value results in a Strehl ratio of $0.71, 0.82$ and 0.88 for the wavelengths $\lambda = 500\,\text{nm}$, 650 nm and 800 nm, respectively. This values are very close with the ones obtained by our measurements, namely $0.74, 0.82$ and 0.86 for the respective wavelengths.

Those results show an established technique for microlens characterization and the proper operation of the instrument. As mention previously however, those measurements are useful for assessing the performance of the microlenses but cannot be traced back to its surface profile; providing feedback about the surface profile however, is the most important objective in terms of fabrication (and consequently performance) optimization. In the next section, we elaborate on the focal spot measurements and demonstrate the principles and functionality of the intermediate plane measurement i.e. measuring the phase profile at a plane between the surface of the lens and its focal plane.

3.3 Novel intermediate plane measurement

In order to achieve high numerical aperture lenses, we need to go beyond the paraxial approximation and use aspheric surfaces to compensate for wavefront aberrations [12, 13]. This however, means that lens design complexity increases, since the optimal shape depends on other parameters of the system, like the position of the object, the aperture size or the apodization [14]. Consequently, the performance of the lens will deteriorate if it is tested under different conditions.

3.3.1 Shortcomings of focal spot measurements

The previously defined Strehl ration in Eq. 3.2 can be also written as [15]:

$$SR = \frac{max\{I_{meas}\}}{P_0 \pi (\frac{NA}{\lambda})^2}, \tag{3.4}$$

where NA is the numerical aperture of the lens under test. Although the formula is quite simple, calculating the numerical aperture of microlenses requires the value of their hard aperture, which is difficult to define for microlenses fabricated at wafer level by photoresist reflow and reactive ion etching [2]. The measurement of the surface of the lens solves this issue, which means though that an additional measurement is needed and the measurements presented previously are not sufficient.

Moreover, the focal spot will be substantially aberrated, if the lens is not designed for plane wave illumination. In this case, the Strehl ratio can be estimated by the approximation [16]:

$$SR = e^{-\sigma^2}, \tag{3.5}$$

where σ^2 is the variance of the phase aberration. This way, we can estimate the Strehl ratio for various numerical apertures, without the need of defining an ambiguous hard aperture. Of course, this method relies on phase measurements, which strengthens our claim for extracting the phase profile at a different plane. We should be careful though, because the illumination conditions of the microlens can give rise to aberrations not related to its performance; this issue will be addressed in the next section.

We emphasize again that the focal spot measurement does not provide any feedback on the fabrication optimization, which is of high practical value. As stated previously, when examining the focal plane, all the surface information of the microlens is compressed within an area with a diameter of a few microns; it is questionable if any relevant information can be extracted by those measurements. We now move on to show how the intermediate plane measurement copes with those issues.

3.3.2 Aberration estimation

Before demonstrating the method itself, we will prove its validity. First, we will show that the aberrations introduced by the testing conditions do not void the method. Let us consider the wavefront produced by an ideal lens under plane wave illumination (testing condition), which can be written as:

$$W_i^{pw} = W_s + \delta W_s. \tag{3.6}$$

Equation 3.6 implies that the total wavefront produced by the ideal lens W_i^{pw} is dominated by the spherical one W_s, which is perturbed by the aberrations induced by the test conditions and are included in the δW_s term.

The wavefront of a real lens with inherent aberrations ΔW under test conditions, can be expressed as:

$$W_l^{pw} = W_s + \Delta W + \delta(W_s + \Delta W) = W_s + \delta W_s + \Delta W + \delta(\Delta W). \tag{3.7}$$

The last term of eq. 3.7 expresses the influence of the testing conditions on the aberrations of the lens and can be considered negligible, compared to the rest of the terms. Solving eq. 3.7 for the inherent aberrations of the lens, we get:

$$\Delta W \approx W_l - (W_s + \delta W_s) = W_l^{pw} - W_i^{pw}. \tag{3.8}$$

The meaning of eq. 3.8 is that we can approximate the inherent aberrations of the lens (the aberrations that will be present even when the illumination conditions are optimized) with the difference of the real measurement (recorded with plane wave illumination) from the wavefront produced by an ideal lens (again, when illuminated by a plane wave). This requires the knowledge of the wavefront of the ideal lens, which poses no problem, since we can either calculate it analytically for plano-convex lenses, or simulate it when the the shape of the lens is more complicated.

3.3.3 Surface extraction

In the framework of ray optics, the phase $\Phi(x, y)$ of thick plano-convex lens with surface profile $z(x, y)$ can be written as:

$$\Phi_0(x, y) = k\left(n + \sqrt{1 + m_x^2 + m_y^2}\right) z(x, y), \tag{3.9}$$

where the slopes of the rays $m_{x,y}$ are analytically determined by the refraction at the lens surface. By obtaining the phase map Φ_m at a known distance $z = z_m$, and subtracting the reference phase Φ_0 from it, allows us to solve for the lens surface:

$$z = \frac{\Phi_m - \Phi_0 + kz_m\left(n - \sqrt{1 + m_x^2 + m_y^2}\right)}{k\left(n - \sqrt{1 + m_x^2 + m_y^2}\right)}. \tag{3.10}$$

Equation 3.10 requires the knowledge of the phase profile Φ_0 at the surface of lens; if we had access to that information, we could directly extract the surface profile though. The motivation of this method is that we cannot capture this information, because of the reduced field of view of the microscope objective required to carry out those measurements. In our approach we assume that Φ_0 is a reference spherical wavefront, obtained by an ideal lens by simulations. The importance of this equations is that it shows that by measuring the phase profile Φ_0 at a known distance z_m, with a defined wavelength (thus defined wavevector k_0) and considering the refractive index of material of lens known, we can extract the surface profile.

3.3.4 Experimental application

The methods described above are applied on a microlens that is fabricated at wafer level using photoresist reflow with subsequent reactive ion etching [2]. This particular lens was selected because it possess one of highest numerical apertures ($NA \approx 0.4$) achievable by this fabrication technique. Its diameter, $D = 300\,\mu\text{m}$, and radius of curvature, $ROC = 150\,\mu\text{m}$, result in a maximum surface slope of about 35°, which is close to the total internal reflection limit, that is 41°.

The phase profile is recorded using a Leica N Plan Achromat, 20x microscope objective of 0.4 numerical aperture, at the distance of $z = 50\,\mu\text{m}$ from the lens vertex and at the wavelength $\lambda = 550\,\text{nm}$. The resulting wrapped phase is shown in Fig. 3.7(a) and the unwrapped profile, along the x axis for $y = 0\,\mu\text{m}$, overlaid with its derivative are shown in Fig. 3.7(b). In the latter figure, it can be seen that the wavefront is convex and converges towards the focal spot within an area of diameter $D = 200\,\mu\text{m}$. Beyond that point, there is a strong dissimilarity to a spherical wave; the abrupt change of the derivative can be used as a convenient way to define the active aperture of the microlens.

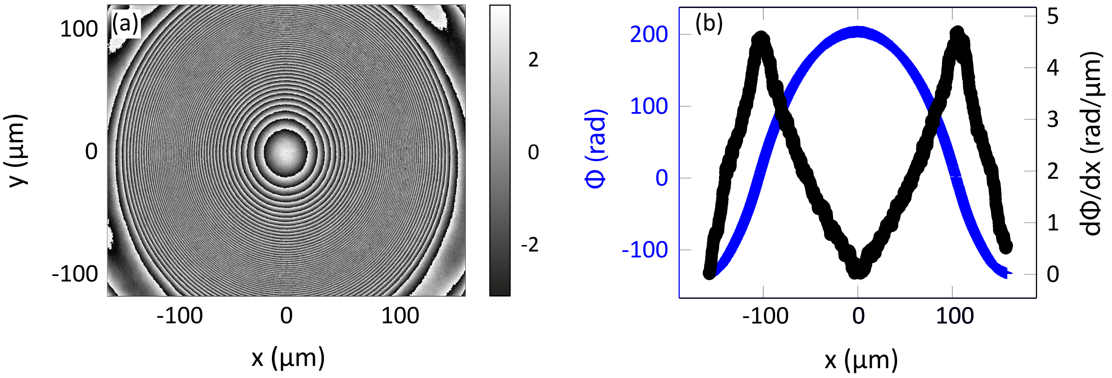

Figure 3.7 – (a): Recorded wrapped wavefront produced by the microlens. (b): (blue) unwrapped phase profile and (black) its derivative, along the x axis at $y = 0\,\mu\text{m}$. The measurement was carried out with an N PLan Apochromat 20x 0.4 NA Leica objective at the wavelength $\lambda = 550\,\text{nm}$ and a distance $z = 50\,\mu\text{m}$ from the vertex of the lens.

This measurement is used to extract the wavefront aberration as is described by eq. 3.8. The deviation from a perfect spherical wavefront and the decomposition of the aberrations into Zernike polynomials are shown in Figs. 3.8(a) and 3.8(b), respectively. The results show that the root meas square value of the wavefront aberration is 0.5 wave and the peak-to-valley value is 2.24 wavefront. It is obvious that the spherical aberration is dominant.

From the same measurement, the surface profile of the microlens is extracted, using eq. 3.10. For comparison purposes, the profile was also measured with a stylus profilometer; the results of both methods were fitted to the standard aspherical equation [14] and their residuals are plotted in Fig. 3.9. In the same figure the target surface is also shown for completeness. The radius of curvature and the amplitude of the residuals for the proposed method and the stylus measurement are $ROC = 152.5\,\mu\text{m}$ and $150.9\,\mu\text{m}$ and $A = 46.1\,\text{nm}$ and $67.5\,\text{nm}$ respectively, which shows good agreement between the two methods, especially for fabrication

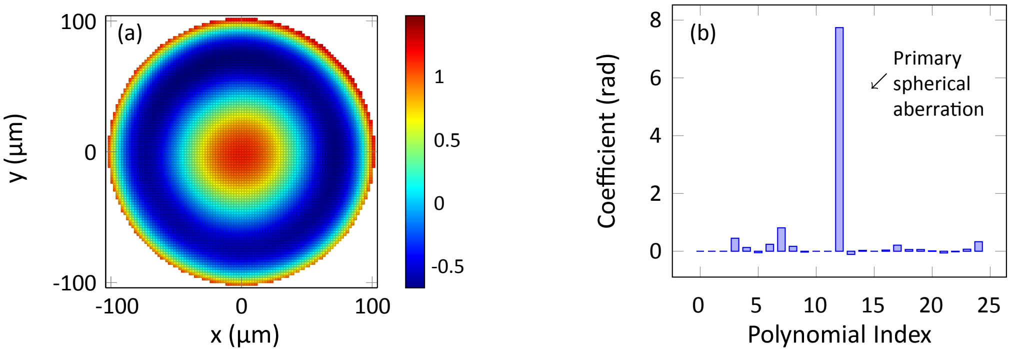

Figure 3.8 – (a): Deviation of the measured wavefront from an ideal spherical shape. (b): Decomposition of the aberration into Zernike polynomials. Root meas square = 0.55 wave, Peak-to-valley = 2.24 waves. Polynomial indices correspond to [17].

optimization purposes.

3.3.5 Restatement of the method

With the results acquired using the new method, we produce measurement results that are consistent with established state-of-the-art techniques and most importantly can be used for fabrication optimization purposes. Here, we attempt a different, qualitative description of the main idea. Assuming that the sought-after information is the profile of lens, we can extract it with high precision if we measure it with a system with high resolving power (numerical aperture in the case of microscope objectives). However, as the size of the lens increases, it not longer fits inside the field of view of the objectives. As we move further away from the lens surface, the same information is contained within a smaller space, as the incoming field is being focused. Extracting the same information requires an even greater resolving power that is not always achievable, thus we capture an averaged contribution of the surface. To the extreme of the focal spot, all the information of the surface is contained in such a confined space, that almost no information about the surface that created it can be extracted. The idea of the intermediate plane measurement is to find a plane at which, on the one hand, the information of the profile of the lens is contained in smaller area, compared to that actual size of the lens. On the other hand, the information we cannot collect can be compensated by numerical methods and the physical constrains of the lens and the fabrication process. To some extend, all the information might be redundant. The criterion we used to choose the plane was to create an uniform illumination across the detector and be confined within this field of view. Although this method was applied on a specific microlens, it is possible to be expanded for a broader range of shapes, which can also be achieved by slight modifications on the set-up. For a further study, the reader is referred to the works of Jeremy Bégueling et al [18, 19].

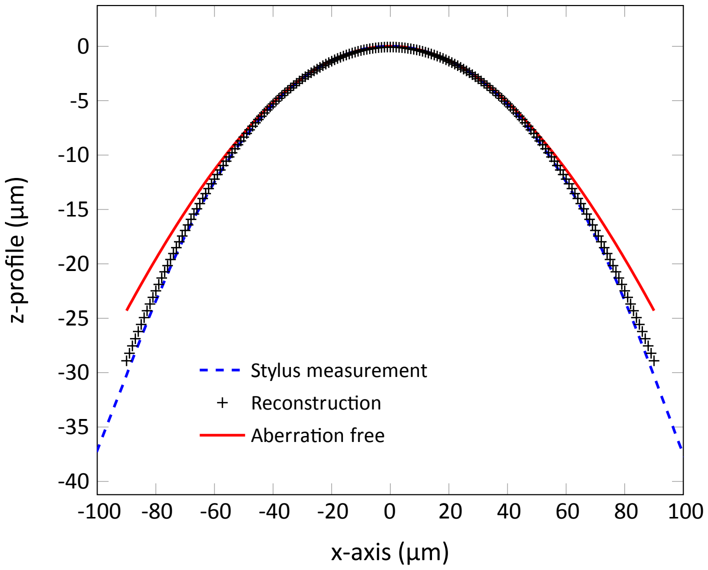

Figure 3.9 – Comparison of the (red) ideal lens profile to those extracted by (dashed blue) stylus profilometry and (black crosses) surface reconstruction from an intermediate plane measurement. The agreement between the intermediate plane measurement and the established profilometry technique is satisfactory, especially for fabrication optimization purposes. The target curve is shown for completeness.

Bibliography

[1] Hans Zappe. *Fundamentals of Micro-Optics*. Cambridge University Press, Cambridge, 2010.

[2] Ph Nussbaum, R Völkel, H P Herzig, M Eisner, and S Haselbeck. Design, fabrication and testing of microlens arrays for sensors and microsystems. *Pure and Applied Optics: Journal of the European Optical Society Part A*, 6(6):617–636, November 1997.

[3] Teng-Kai Shih, Chia-Fu Chen, Jeng-Rong Ho, and Fang-Tzu Chuang. Fabrication of PDMS (polydimethylsiloxane) microlens and diffuser using replica molding. *Materials for Advanced Metallization (MAM 2006)*, 83(11):2499–2503, November 2006.

[4] Stephan Reichelt and Hans Zappe. Combined Twyman–Green and Mach–Zehnder interferometer for microlens testing. *Applied Optics*, 44(27):5786–5792, September 2005.

[5] Johannes Schwider and Oliver R. Falkenstoerfer. Twyman-Green interferometer for testing microspheres. *Optical Engineering*, 34(10):2972–2975, October 1995.

[6] Myun-Sik Kim, Toralf Scharf, and Hans Peter Herzig. Small-size microlens characterization by multiwavelength high-resolution interference microscopy. *Optics Express*, 18(14):14319–14329, July 2010.

[7] Maciej Baranski, Stephane Perrin, Nicolas Passilly, Luc Froehly, Jorge Albero, Sylwester Bargiel, and Christophe Gorecki. A simple method for quality evaluation of micro-optical components based on 3d IPSF measurement. *Optics Express*, 22(11):13202–13212, June 2014.

[8] ISO 14880 Optics and photonics – Microlens Arrays, 2016.

[9] Herbert Gross, Hannfried Zuegge, Martin Peschka, and Fritz Blechinger. *Handbook fo Optical Systems: Volume 3: Aberration Theory and Correction of Optical Systems*, volume 3. WILEY-VCH Verlag GmbH, September 2105.

[10] I. H. Malitson. Interspecimen Comparison of the Refractive Index of Fused Silica*,†. *Journal of the Optical Society of America*, 55(10):1205–1209, October 1965.

[11] Yajun Li and Emil Wolf. Focal shift in focused truncated gaussian beams. *Optics Communications*, 42(3):151–156, July 1982.

[12] Joseph W. Goodman. *Introduction to Fourier Optics*. Number McGraw - Hill Series in Electrical and Computer Engineering. McGraw - Hill, 2 edition, 1996.

[13] James C. Wyant and K. Creath. Basic wavefront aberration theory for optical metrology. *Applied Optics and Optical Engineering*, 11, 1992.

[14] Herbert Gross, Hannfried Zügge, Martin Peschka, and Fritz Blechinger. Special Correction Features. In *Handbook of Optical Systems*, pages 431–593. John Wiley & Sons, Ltd, 2015.

[15] Max Born and Emil Wolf. Principles of Optics: Electromagnetic theory of propagation, interference, and diffraction of light. *Science*, 146(3648):1154, November 1964.

[16] Virendra N. Mahajan. Strehl ratio for primary aberrations in terms of their aberration variance. *Journal of the Optical Society of America*, 73(6):860–861, June 1983.

[17] Larry N. Thibos, Raymond A. Applegate, James T. Schwiegerling, and Robert Webb. Standards for Reporting the Optical Aberrations of Eyes. *Journal of Refractive Surgery*, 18, October 2002.

[18] Jeremy Béguelin, Michail Symeonidis, Wilfried Noell, Reinhard Voelkel, and Toralf Scharf. Assessing microlens quality based on 3d irradiance measurement at the focal spot area. volume 10678, May 2018.

[19] Jeremy Béguelin, Michail Symeonidis, Wilfried Noell, Reinhard Voelkel, and Toralf Scharf. Towards a complete and meaningful characterization of high NA microlenses by high resolution interference microscopy (to be submitted).

4 Intensity and phase profile study of diffractive optical elements

4.1 Motivation of the study

Analysis of the interference pattern of two optical beams is an established method for extracting detailed information about a sample under test (refractive index, thickness, deformation, etc.) [1]. Several methods have been demonstrated to measure surface topography [2], motion [3, 4], living tissues [5, 6] or to extract three-dimensional data for biological samples [7]. Those techniques use the phase information to extract various parameters of the examined samples, however the phase information is not directly related to their functionality. This chapter deals with components that function readily in the phase regime, thus the resulting phase information is a direct representation of their functionality.

More specifically, we explore the intensity and phase features of the light field transmitted through an optical sample that predominately acts on the phase of the incoming field. Examples of such devices are diffractive optical elements (DOEs) or phase masks [8]. These devices are being increasingly widely adopted to perform various optical functions, including focusing [9], beam-splitting [10], beam shaping [11], etc. The focus of this chapter is brought into a specific family of phase elements, namely the binary phase elements that are designed to induce π phase to the transmitted light at specified positions in the optical aperture, thus realizing the desired optical functionality [12].

The motivation of the work is to ensure the fabrication quality of produced components in an efficient way. Turning to phase measurements is only natural when discussing about phase elements. The idea is to find specific points of the measured data that can indicate the position of the walls of the examined phase step, since this is the most important fabrication parameter. We apply this idea into two scenarios: measuring the size of the phase step and tracking the displacement of the component. This approach has the added benefit of simultaneously verifying the functionality of the component.

4.2 Sample description

4.2.1 Diffractive Optical Element

The samples we investigate are binary diffractive optical elements made of fused silica ($n = 1.45$ at $\lambda = 633\,\text{nm}$). They consists of 20 ridges and grooves, each with a different width, periodically repeated every $\Lambda = 200\,\mu\text{m}$. The height of the fused silica ridge is $h \approx 0.7\,\mu\text{m}$, thus creating a $\Delta\phi = \pi$ phase difference at the operating wavelength of $\lambda = 633\,\text{nm}$ between the fused silica ridge and the etched groove. A schematic drawing of the sample is shown in Fig. 4.1. A part of the sample is shown in intensity and phase imaging in Figs. 4.2(a) and 4.2(b) respectively. On the image we can see starting from left to right: part of a groove, whole ridge, whole groove, part of another ridge. The data that were used to produce the images show have been treated as described in chapter 2. The area within the black dashed rectangles is used for the analysis described in the following sections.

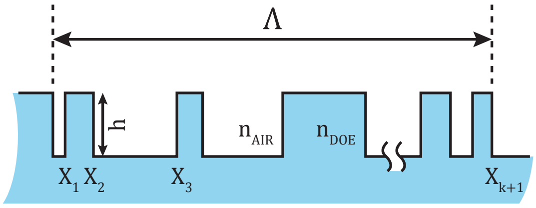

Figure 4.1 – Schematic diagram of the binary diffractive optical element. It consists of 20 ridges and grooves in a fused silica substrate, yielding a spatially varying phase delay for light propagating through the device. The height of the ridges is $h \approx 0.7\,\mu\text{m}$, so as to induce $\Delta\phi = \pi$ phase difference at the operating wavelength of $\lambda = 633\,\text{nm}$. This pattern is repeated every $\Lambda = 200\,\mu\text{m}$. The point X_i corresponds to the position of the i^{th} edge between a ridge and groove.

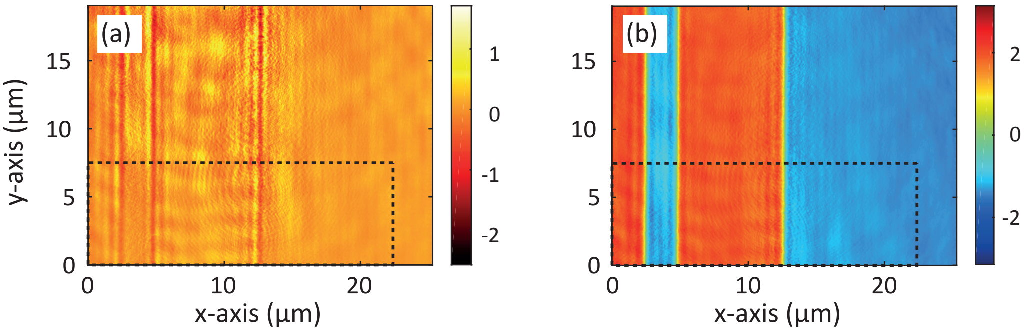

Figure 4.2 – Sample overview, after processing. (a): Intensity, (b): Phase. The region within the dashed rectangle was used for our analysis. From left to right the sample begins with a groove and then the regions alternate, ending in a ridge.

These elements are fabricated by electron-beam lithography and dry etching to create a chromium etch mask, and then by reactive ion etching to obtain fused silica surface relief phase structures. According to the manufacturer, the variability of the feature widths is expected to be approximately ±100 nm. A series of five devices were produced, each with an incrementally increasing nominal feature width of $\Delta x = 40$ nm, increasing for the ridge and decreasing for the groove.

4.2.2 Modeling

In order to understand the expected optical characteristics of this device, we first simulate the electric field transmitted by this structure using a *Rigorous Coupled Wave Analysis* (RCWA) electromagnetics solver [13, 14, 15]. We compute the electromagnetic field diffracted by a phase element with 4 edges located at points X_i and total length of $l = 23.74$ µm, which corresponds to a portion of the fabricated device. The illumination is taken to be a normally incident plane wave with wavelengths $\lambda = 480$ nm and 633 nm, in order to study the spectral differences as well. The incident light is polarized at 45° with respect to the x axis, so there is an electric field component both parallel and perpendicular to the groove axis, corresponding to the experimental configuration. The intensity and phase correspond to the vector sum of the two components perpendicular to the propagation direction, $I = |E_\mathrm{x}|^2 + |E_\mathrm{y}|^2$ and $\Phi = \angle\left\{\frac{1}{\sqrt{2}}(E_\mathrm{x} + E_\mathrm{y})\right\}$.

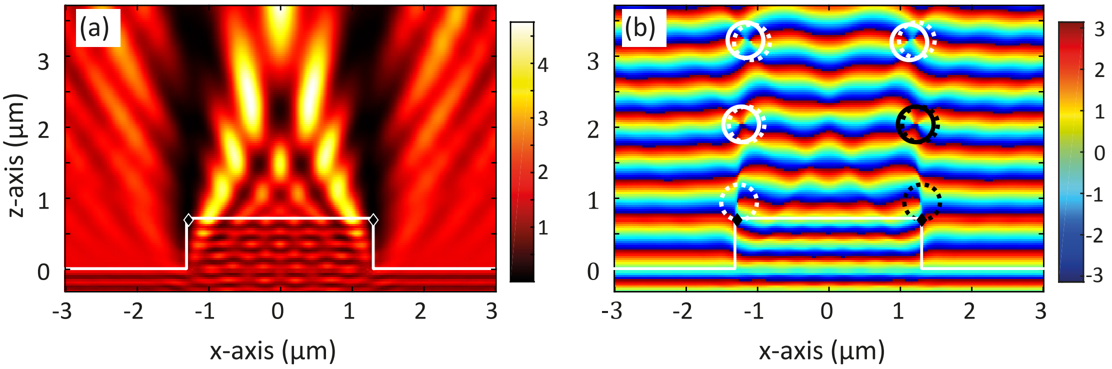

Figure 4.3 – (a) Intensity and (b) phase results for a region of the simulated structure. The width of the ridge is $W = 2.6$ µm and the illumination wavelength is $\lambda = 480$ nm.

The intensity and phase of the transmitted field immediately after propagation through the device are shown in Figs. 4.4 and 4.3 for the wavelengths of $\lambda =$ 480 nm and 633 nm, respectively. In both figures, panel (a) shows the intensity map of the transmitted field, while panel (b) depicts the phase map. For clarity, only the region around a single ridge of width $w = 2.6$ µm is shown. The surface profile of the fused silica substrate and ridge is indicated by the white line. Considering the intensity maps shown in Figs. 4.3(a) and 4.4(a), we see that there is a null in the intensity above the edges of the ridge. This appears to be the narrowest just above the top of the ridge, especially for the $\lambda = 633$ nm case, as at higher z-positions the interference of various diffraction orders produces a more complex intensity distribution. As will be discussed in more detail below, finding a minimum in an intensity profile measured just above the ridges of the structure enables approximate identification of the location of

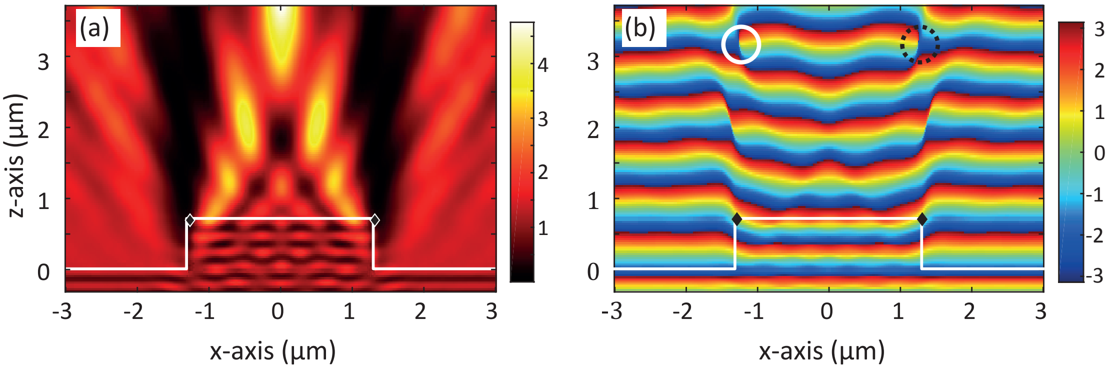

Figure 4.4 – (a) Intensity and (b) phase results for a region of the simulated structure. The width of the ridge is $W = 2.6\,\mu\text{m}$ and the illumination wavelength is $\lambda = 633\,\text{nm}$.

the edges between the ridges and grooves. Those points are indicated by the black diamonds in Figs. 4.3(a) and 4.4(a). Alternatively, the phase maps as shown in Figs. 4.3(b) and 4.4(b) provide two different methods for identifying these edge positions. The first one relies on the fact that there is a phase jump between the regions above the ridge and above the groove. This characteristic is not surprising, as this device is designed to operate in this fashion and produce phase jumps of half-wavelength. The position where the phase value equals to the median of the two distinct phase levels gives us an excellent approximation of the actual position of the edges, as is shown by the black diamonds in Figs. 4.3(b) and 4.4(b).

Another possible approach to measure structural details by identifying special phase features is indicated by the circles drawn on Figs. 4.3(b) and 4.4(b), which show the positions of phase singularities. At these points, the diffracted light interferes destructively, creating a single position where the field is exactly zero [16]. Since there is no amplitude, the phase cannot be defined; these points are commonly called phase singularities or phase residues [17]. In our example, each edge creates a singularity that is sensitive to the polarization of the incoming field. The phase changes by 2π around those points, similar to optical vortices [18]. Their position can be localized, in principle, with arbitrary precision, as singular phase features are not subjected to the diffraction limit.

Phase singularities

At this point, we will slightly deviate from the main narrative, in order to demonstrate the behavior of the phase singularities with respect to polarization and illuminating wavelength. To that end, we show the simulated phase maps of the transmitted light for the two wavelengths ($\lambda = 480\,\text{nm}$ and 633 nm) in Figs 4.5 and 4.6 respectively. For the $\lambda = 480\,\text{nm}$ case, the shown polarization angles are $\theta = 90°$, Fig. 4.5(a), when the electric field is perpendicular to the invariant axis of the step, y axis and $\theta = 0°$, Fig. 4.5(b), when the electric field is parallel to the y axis. For the $\lambda = 633\,\text{nm}$ case, the two angles of polarization, with respect to the y axis, are

$\theta = 90°$ and $\theta = 50°$[1]; the respective results are shown in Figs. 4.6(a) and 4.6(b). The reason for choosing those angle will become apparent in the following analysis.

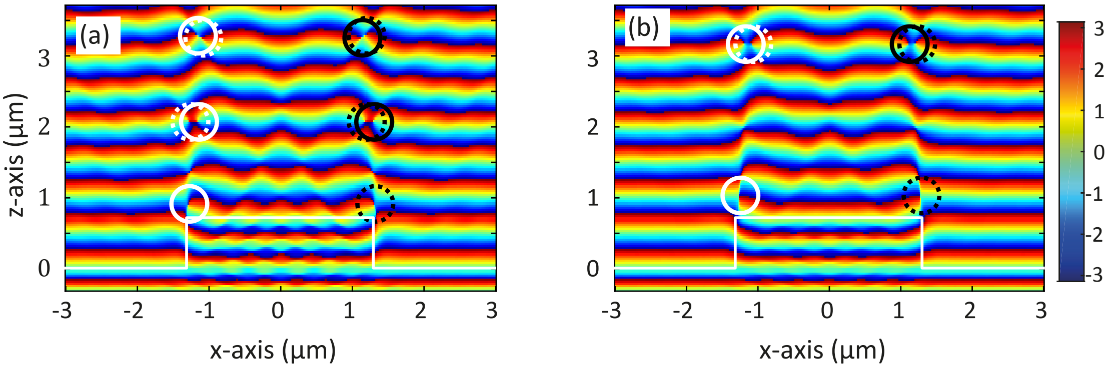

Figure 4.5 – Simulated phase profiles for incoming polarization at (a): $\theta = 90°$ and (b): $\theta = 0°$ at $\lambda = 480$ nm. The circles indicate the positions of the phase singularities. The white line indicates the position of the phase step.

Starting with the $\lambda = 480$ nm case, we observe that each edge creates a certain number of singularities along the z direction. Comparing Figs 4.5(a) and 4.5(b), we see that in the first case the singularities appear in 3 zones along the z axis, but only 2 remain in the latter one. Also, the singularities have moved to slightly higher positions. Comparing those images to Fig. 4.3(b), we see that the phase profile changes very little with respect to polarization, at this wavelength. The disappearance of the singularities indicates that when the electric field is parallel to the edges of the structures, the diffracted field is not strong enough to perfectly cancel out the incoming field and create the singularities at those positions.

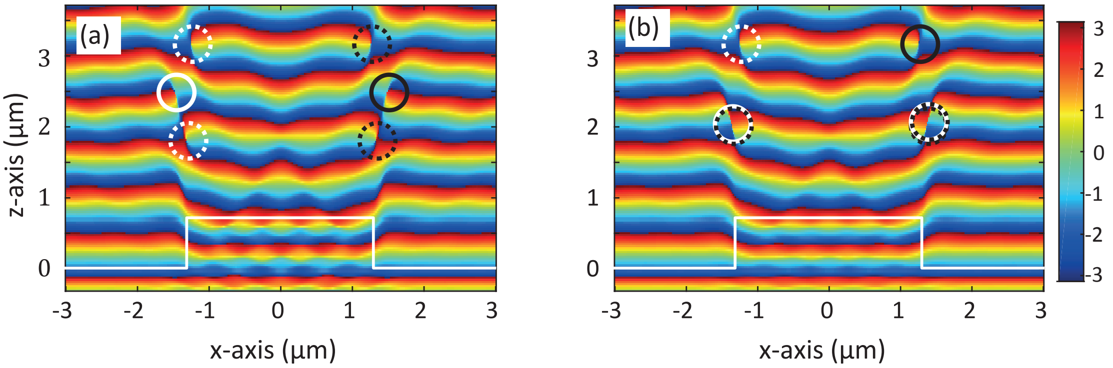

Figure 4.6 – Simulated phase profiles for incoming polarization at (a): $\theta = 90°$ and (b): $\theta = 50°$ at $\lambda = 633$ nm. The circles indicate the positions of the phase singularities. The white line indicates the position of the phase step.

---

[1] for $\theta < 45°$, there is almost no change in the phase results. Since the $\theta = 45°$ case is shown in Fig. 4.4(b), we chose the smallest angle before the results become invariant

Those effects can be better seen in Figs. 4.6(a) and 4.6(b), which shows the corresponding case for $\lambda = 633\,\text{nm}$. At a polarization angle of $\theta = 90°$ we notice again that each wall creates 3 singularities that are found in distinct positions along the z axis. As the electric field tends to become parallel to the walls, the singularities approach each other, as can be seen from Fig. 4.6(b) that depicts the singularities for a polarization angle of $\theta = 50°$. At a certain polarization angle around 50°, two singularities with opposite charges overlap and annihilate. The total charge becomes 0 and the singularity in no longer detectable. This is however, a highly unstable situation, as any slight perturbation will change the positions of the singularities [19]. As was the case for the $\lambda = 480\,\text{nm}$, when the polarization angle is further reduced, the diffracted field is not strong enough to cancel out the incoming field, thus not all the singularities are created, as seen also in Fig. 4.4(b). It should also be mention that at shorter wavelengths, more singularities are created, since light is stronger diffracted and the field has finer details.

Nevertheless, we choose to work with $\lambda = 633\,\text{nm}$, because it is the operation wavelength of the structure, thus it visualizes its optical function, and because we achieve better measurement quality, as will be shown later.

Returning to the main subject, we note that the analysis of the numerical results provided us with several methods for locating the approximate position of the edges of the the ridge using either the intensity or phase maps. Moreover, these characteristics are likely to be particularly pronounced with this structure, as it is engineered to have a $\Delta\phi = \pi$ phase difference. However, since the incident light is polarized at 45°, the singularities appear at greater z values, consequently their detection requires longer measurements along the z-axis. This fact increases both the recording and processing time, therefore in section 4.3, we choose to focus on measurements that are taken in a single plane. An example profile of the intensity and phase from the simulation data presented in Figs. 4.3 and 4.4 at $z = 0.7\,\mu\text{m}$—at the top of the ridge—is shown in Fig. 4.7(a) and 4.7(b), respectively.

As can be seen in Fig. 4.7, both the lateral position of the minima in an intensity profile or the phase jumps in a phase profile are suitable to identify the location of the edges between the ridges and grooves of this structure, with an accuracy of $+10\,\text{nm}$ to $-30\,\text{nm}$. The inset shows the fine details of the intensity profile, which in principle could improve accuracy, but that cannot be resolved by the optical system. Although the middle-crossing underestimates the width by 20 nm and the intensity minimum by 10 nm, the values are still within the expected experimental accuracy. Thus, we conclude that locating the minima in an intensity profile or the jumps in a phase profile taken just above the surface of the structure are both appropriate methods to approximately identify the locations of the edges of the ridges on this structure.

4.2.3 Preliminary measurements

To compare with the simulation results, we first perform a three-dimensional scan of a corresponding region of the sample. Images of a ridge with nominal width $w = 2.6\,\mu\text{m}$ are taken. The sample is then translated along the z-axis (propagation direction), with a step of 65 nm

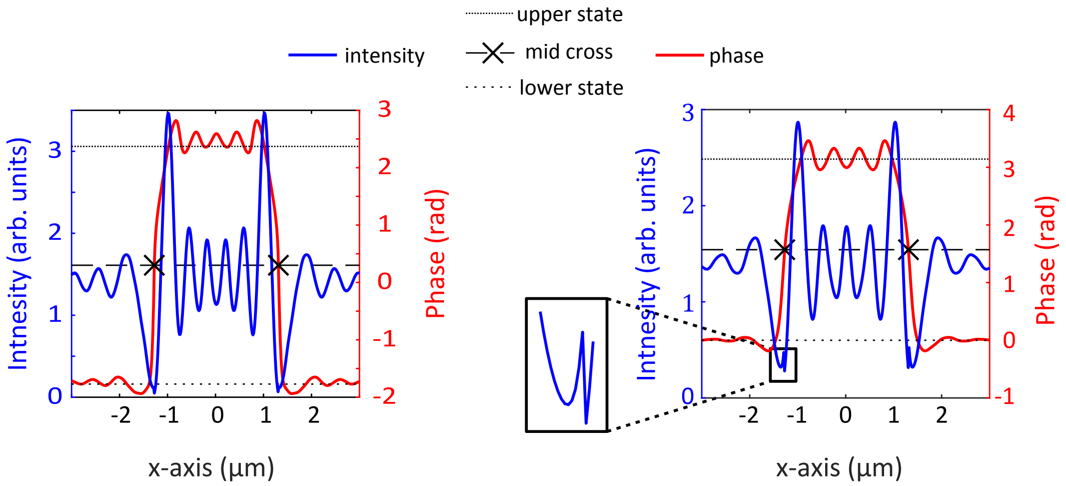

Figure 4.7 – Simulated intensity (blue) and phase (red) profiles at $z = 0.7\,\mu\text{m}$ for wavelengths (a): $\lambda = 480\,\text{nm}$ and (b): $\lambda = 633\,\text{nm}$. Both the minimum in the intensity profile and the middle-crossing point in phase profile localize the edge with an accuracy of $+10\,\text{nm}$ to $-30\,\text{nm}$. The inset shows a detailed view of the intensity profile that cannot be resolved by the optical system.

and 33 nm for the intensity and phase, respectively. At each position we record both quantities and subsequently, we create the three dimensional representation of the field by stacking the recorded slices on top of each other. The results of the measurements are shown in Figs. 4.8 and 4.9 for $\lambda = 480$ nm and 633 nm, respectively. In both figures, panel (a) shows the intensity map and panel (b) the phase map. The cross-sections are averaged over 10 slices of the $x-z$ plane to reduce the noise, corresponding to $\approx 190\,\text{nm}$ along y-axis (the structure is invariant along this direction). The solid white line represents the surface of the fused silica substrate and ridge.

Comparing Figs. 4.8 and 4.9 to Figs. 4.3 and 4.4, we see that the experimental measurements agree very well with the simulations in the air region above the structure. It should be noted that the measured data inside the structure cannot be compared to the simulated results. The reason is that in the latter case we have the exact form of the field inside the structure, while in the former case we image through a non-flat structure. Most pertinent to this work is the dark bands in the intensity map located above the edges of the ridge, and the phase steps in the phase maps also located above the edges of the ridge. The experimental set-up also captures the predicted phase singularities (indicated by circles), as well as some additional ones (indicated by gray circles). We should not forget that the singularities appear in low intensity regions. However, the inherent behavior of the structure is not the only cause of singularities; low signal to noise ratio can create phase differences that appear as singularities. The large numbers of the non-predicted singularities indicates the low signal to noise ration for that wavelength in that region. This is attributed to the reduced power output of the source and the low sensitivity of the detector at the wavelength of $\lambda = 480\,\text{nm}$. This is another important reason for working at the operational wavelength of the device ($\lambda = 633\,\text{nm}$), where

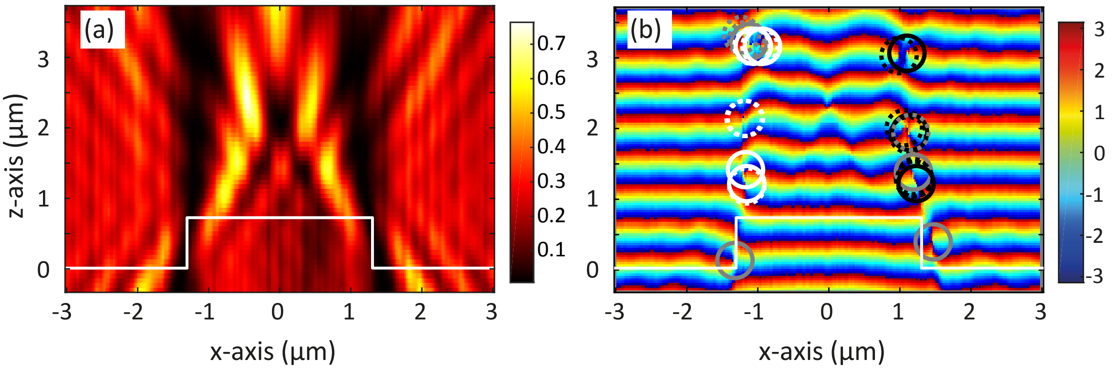

Figure 4.8 – Measurement of (a) intensity and (b) phase maps as measured using the high-resolution interference microscope to image a section of the diffractive optical element with illumination at 480 nm. An average of 10 slices of the $x-z$ plane is presented. The white line represents the surface of the fused silica substrate and ridge. The circles indicate the position of the phase singularities.

the quality of the measurements is better.

The higher measurement quality is evident from the better agreement of the singularities between simulation and experiment at the operational wavelength. Nevertheless, any slight deviation of the measurement from the simulation (e.g. differences in singularity positions), is understandable since the simulated results were not spatially filtered to emulate the low-pass behavior of the microscope objective. Moreover, the simulations were carried out with a strictly monochromatic illumination, while the measurements were performed with an illumination bandwidth of ≈ 10 nm. As was mentioned previously, inside the fused silica region (below the white line in Fig. 4.9), the simulation and experimental results differ significantly. In the simulation results, it is possible to compute the field intensity and phase exactly, whereas in the experimental results, we shift the focal plane of the microscope below the material interface, but must still image through the non-flat surface of the sample. Evidently, the instrument is unable to effectively image below the structured surface of the sample. In any case, this area is not needed for the interpretation of the results.

We can now proceed to determine the ridge and groove (not shown) widths using both the intensity and phase maps for each z plane shown in Fig. 4.9 as a function of the focal plane position. These results are shown in Figs. 4.10(a) and 4.10(b), for the measured width of the ridge and groove, respectively, using the intensity (blue) and phase (red) data. The procedure for measuring the dimensions using the recorded data is explained in more detail below. As shown in Fig. 4.10, the intensity and phase results are close when the top surface of the ridge is in focus (height = 0.7 µm). The phase profile is more sensitive to defocusing; nevertheless, close to the focal plane (±100 nm), the deviation is smaller than 50 nm. Consequently, for this sample we conclude that if we wish to record a two-dimensional image in a single z plane, we will attempt to position the focal plane of the imaging system at the surface of the ridges in

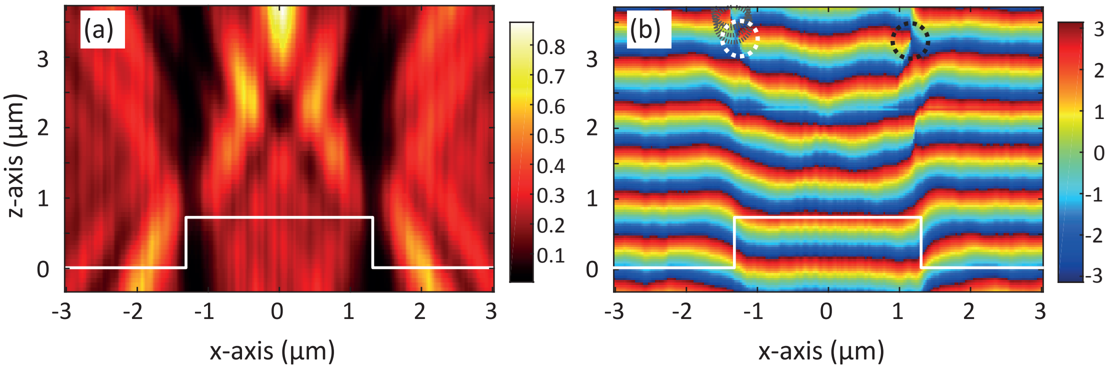

Figure 4.9 – Measurement of (a) intensity and (b) phase maps as measured using the high-resolution interference microscope to image a section of the diffractive optical element with illumination at 633 nm. An average of 10 slices of the $x-z$ plane is presented. The white line represents the surface of the fused silica substrate and ridge. The circles indicate the position of the phase singularities.

the sample.

4.3 Measurement results

We now apply the instrument and methodology to characterize the size and position of the ridge and groove features. Both methods, utilizing the intensity and phase profiles extracted from images taken at a single z-plane located at the surface of the sample, are explored.

4.3.1 Profile extraction

Figures 4.11(a) and 4.11(b) show a region of the maps in intensity and phase, respectively, presented in Figs. 4.2(a) and 4.2(b) (as indicated by the dashed rectangles). Figures 4.11(c) and 4.11(d) show the averaged line profile along the groove axis, y, for the intensity and phase, respectively. Averaging over 400 lines in the image mitigates the effects of noise. Based on the simulation results described in Section 4.2, we observe the expected minima in the intensity profile in Fig. 4.11(c), as well as the expected steps in the phase profile of Fig. 4.11(d). In addition, as expected, the phase difference in the phase steps is within ±1% of π.

The minima in intensity, indicated by the magenta asterisks in Fig. 4.11(c) are found by simply finding the location of the minimum value, around the expected position of the edge. For the middle-values localization in the phase profiles, indicated by the blue x'es, the function `midcross` of *Matlab* [20] was used. Using those points, we measure the width of the ridge to be 2.31 µm / 2.30 µm and of the groove 7.89 µm / 7.86 µm for intensity and phase respectively, compared to the nominal values of 2.44 µm and 7.50 µm.

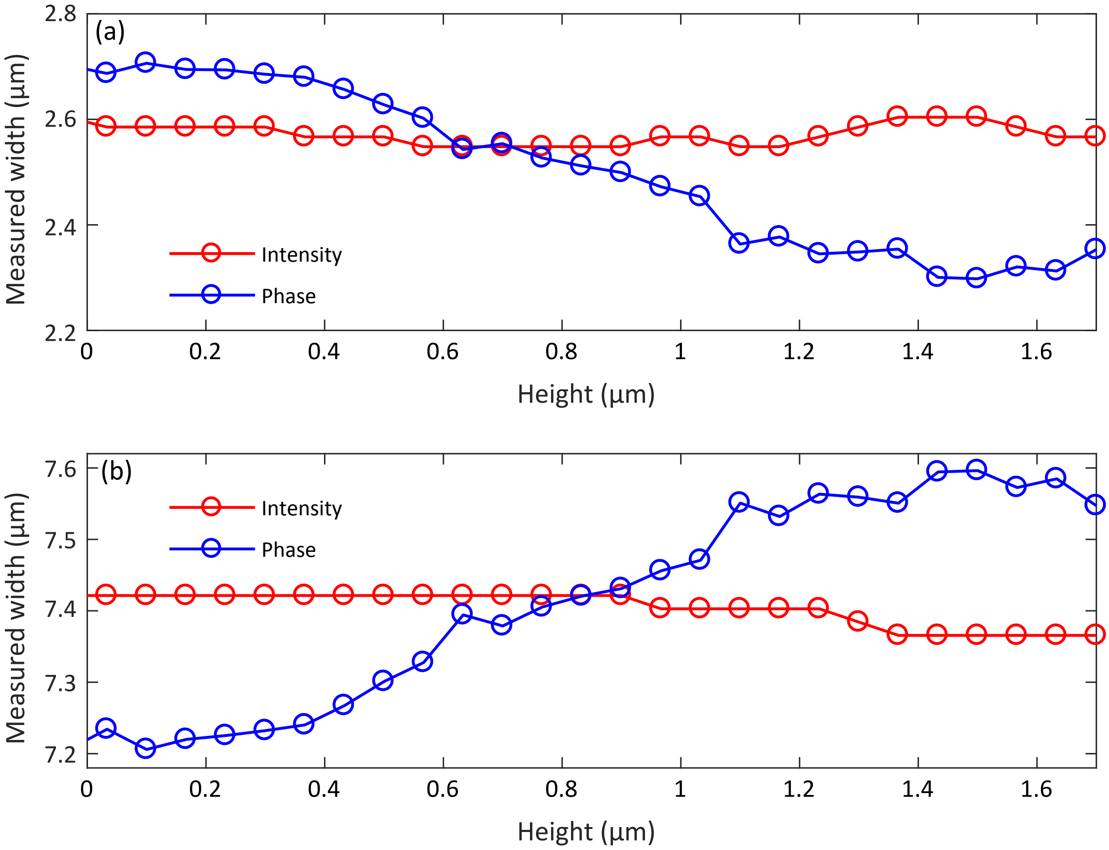

Figure 4.10 – Measured width of the ridge (a) and groove (b) as a function of the focal position. The results agree near the top surface of the ridge.

4.3.2 Feature Size Determination

The positions of the edges of the ridges and grooves are determined using the methods described above, namely by locating the positions of the minima in the intensity profiles and by finding the middle-crossing points in the phase profiles. Here, we image a region of the sample containing one ridge and one groove, and estimate the width of each feature. This measurement is repeated five times on different samples with a slightly different ridge and groove width, as described in Section 4.2. The nominal widths of each feature for the five samples are shown in Tables 4.1 and 4.2. The measured intensity and phase profiles for the five structures, averaged over 500 lines from the original image, are shown in Fig. 4.12. For each profile, the distance between adjacent points of interest (minima/phase jumps) is computed, approximating the width of each ridge or groove. These results are also presented in Tables 4.1 and 4.2.

Both methods, using the intensity and phase images, yield width values for the ridges which are slightly higher than the nominal values, and widths for the grooves which are slightly lower. However, all of the measured widths are within approximately 0.22 µm of the nominal values.

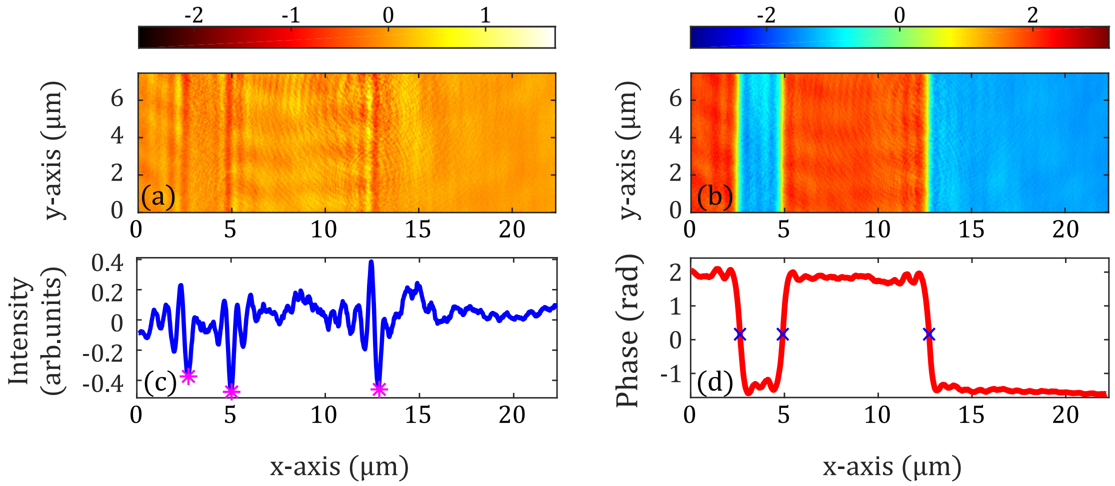

Figure 4.11 – Intensity (a) and phase (b) images of a region of the sample (indicated by the dashed rectangles in Figs. 4.2(c) and (f), respectively). (c), (d): Averaged profiles along 400 lines of the y-axis for the intensity and phase records respectively.

Table 4.1 – Nominal and measured widths of device ridges

$Width - Ridge(\mu m)$					
		$(Intensity)$		$(Phase)$	
$Sample$	$Nominal$	$Measured$	$Difference$	$Measured$	$Difference$
1	2.44	2.66	0.22	2.58	0.14
2	2.48	2.70	0.22	2.62	0.14
3	2.52	2.72	0.20	2.63	0.11
4	2.56	2.77	0.21	2.70	0.14
5	2.60	2.81	0.21	2.77	0.17

In addition, the positions determined by the two methods agree to within approximately the tolerance stated above. Moreover, in most cases the width values found using the phase images are slightly closer to the nominal values than those using the intensity images.

4.3.3 Displacement

Next, we observe the position of the sample feature edges after laterally translating the sample by a known value. This experiment allows us to quantify the precision with which the edge displacement can be traced in the intensity and phase measurements. To achieve this, the sample was mounted on a piezo stage (PI P-517.3CL, movement precision 1 nm) that translated the sample along the x-direction relative to the first measurement (denoted as displacement 0). After each translation step, the intensity and phase profiles were recorded and the exact displacement was verified by the sensor of the piezo stage, which is used in closed-loop operation. Along the y (invariant) direction, 800 rows of the image are averaged to produce

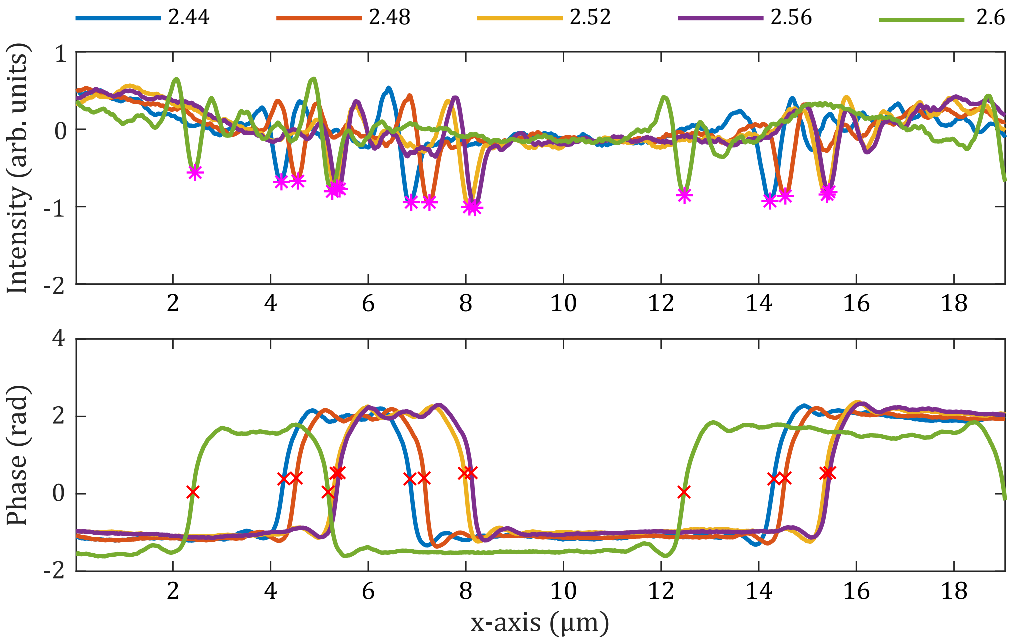

Figure 4.12 – Intensity (top) and phase (bottom) profiles of the five measured structures. Edges between ridges and grooves are observed as minima in the intensity profiles (indicated by magenta asterisks), and as jumps in the phase profiles (indicated by red x'es).

the intensity and phase measurement profiles shown in Figs. 4.13(a) and 4.13(b), respectively. In the intensity profiles, the edges between ridges and grooves are associated with intensity minima. The positions of these minima are found, and indicated by magenta asterisks in Fig. 4.13(a). For each profile, a total of three minima are identified, corresponding to the three edges in the original image. The displacement of each edge relative to the first measurement (noted as displacement 0.00) are computed, and the average displacement for each case is shown in Table 4.3. For the phase profiles, the positions of the edges are associated with phase jumps. The mid-point of each such phase jump is observed, as indicated by the red x'es in Fig. 4.13(b). The displacement of each of the three edges is computed, and averaged as also shown in Table 4.3.

Table 4.2 – Nominal and measured widths of device grooves

		$Width-Groove(\mu m)$			
		$(Intensity)$		$(Phase)$	
$Sample$	$Nominal$	$Measured$	$Difference$	$Measured$	$Difference$
1	7.50	7.35	−0.15	7.46	−0.04
2	7.46	7.29	−0.17	7.39	−0.07
3	7.42	7.33	−0.09	7.41	−0.01
4	7.38	7.25	−0.13	7.35	−0.03
5	7.34	7.22	−0.12	7.29	−0.05

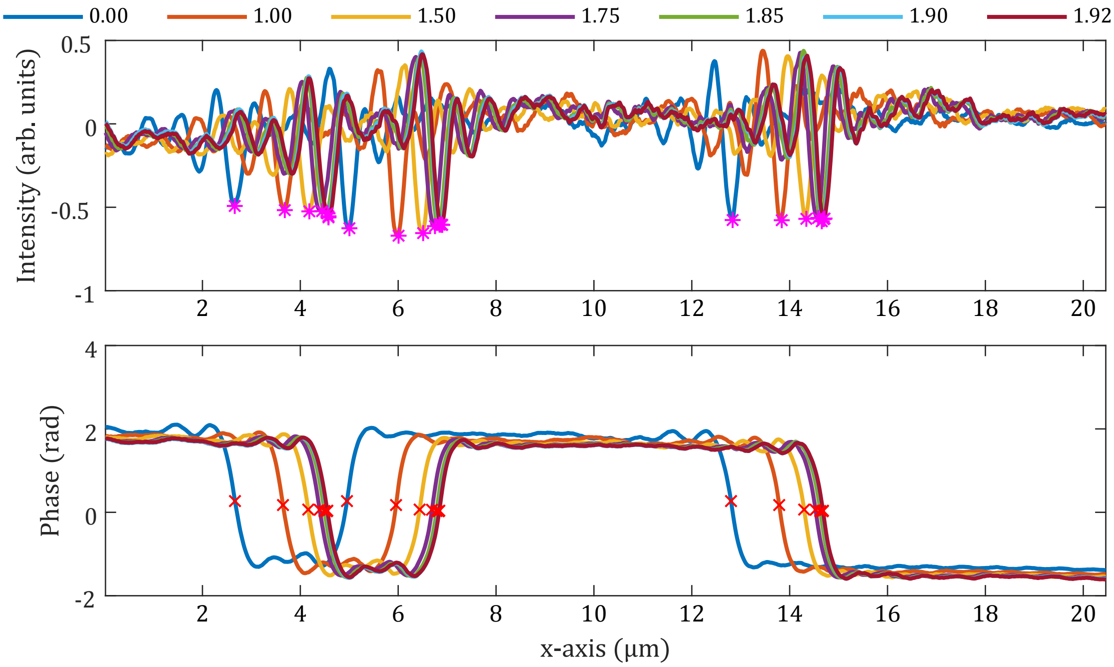

Figure 4.13 – Intensity (top) and phase (bottom) profiles averaged over 800 lines of the captured image, for seven different translational positions along the x-axis, as indicated in the legend (in μm). Edges between ridges and grooves are observed as minima in the intensity profiles (indicated by magenta asterisks), and as jumps in the phase profiles (indicated by red x'es).

In addition to the displacements measured using both the intensity image and the phase image, Table 4.3 also shows the offset (in nm) of each measurement, as well as the percentage deviation from the nominal value. Of note is the fact that each measurement is within approximately 50 nm or 2.5% of the nominal displacement value. Comparing the two methods, the positions of the edges are found to agree within the tolerance of approximately 50 nm, although the intensity image seems to provide a slightly lower deviation than the phase image in most cases shown. However, the method used in analyzing the intensity images incorporates a peculiarity of a binary diffractive optical element, where a phase change of π is expected between a ridge and groove. In cases where exact destructive interference might not be expected at such an edge, the phase image may prove to be more reliable. More broadly, comparing Figs. 4.13(a) and 4.13(b), we can see that the phase approach provides a more distinct indication of the sample edges, and thus might be expected to be more tolerant to noise. Finally, while admittedly referring to a single sample with a known profile and desirable characteristics such as a π phase step between a ridge and groove, under these conditions analysis of both the intensity and phase measurements is able to observe and quantify translational displacements of the sample with sensitivity on the order of 50 nm, well below the classical diffraction limit.

Table 4.3 – Measured and nominal edge displacement

	Nominal Displacement (μm)					
	1.00	1.50	1.75	1.85	1.90	1.92
$Intensity$						
$Displacement(\mu m)$	1.01	1.51	1.76	1.85	1.88	1.90
$Offset(nm)$	11	13	11	4	-15	-23
$Deviation(\%)$	1.06	0.85	0.62	0.21	0.80	1.19
$Phase$						
$Displacement(\mu m)$	0.99	1.49	1.73	1.83	1.87	1.88
$Offset(nm)$	-10	-8	-18	-23	-26	-36
$Deviation(\%)$	1.04	0.51	1.04	1.25	1.35	1.87

4.4 Conclusion

In this work we record the intensity and phase maps of the light transmitted through a binary phase element that is designed to induce a π phase delay between its ridges and grooves. This phase difference creates specific features in both the intensity and phase profiles, which we use to localize the position of the edges of the ridges and grooves. More specifically, using both numerical and experimental results, we show that the minima in the intensity profiles and jumps at the phase profiles approximately indicate the positions of these edges. We also observe experimentally phase singularities that provide a possible alternative method for edge localization, although they require three-dimensional scanning measurements. Based on the experimental and simulation results for this particular device (having a π phase step when operated at the design wavelength of $\lambda = 633\,\text{nm}$), we determine that an image taken in a single z-plane located at the top of the ridges (i.e. at the upper surface of the structure) can provide useful information about the position of the feature edges using either the intensity or phase methods.

From the position of the edges, we calculate the widths of the material ridges and also track the displacement of the structure. Using this method, we estimate the dimensions of the structure with an accuracy of approximately 220 nm and we measure sample displacements as small as about 50 nm. Comparing the two methods—intensity and phase—for this specific sample and with this instrument, we find that both approaches are approximately equivalent in terms of resolution. It is likely, however, that the π phase step found in this device makes the intensity contrast at the feature edges particularly stringent due to destructive interference. We expect that for devices with different or multiple phase steps, the phase mapping method would be more robust and better able to image the feature edges within such a device.

Also, we illuminate at the intended wavelength of operation of the sample, namely $\lambda = 633\,\text{nm}$, in order to optimize the optical performance of the device. However, the instrument is able to operate at a range of optical wavelengths, facilitating the investigation of optical phenomena such as phase singularities, as well as permitting the characterization of samples designed to operate at other wavelengths. In addition, this instrument is able to capture both conventional and interferometric (phase-resolved) images, facilitating the characterization of a broad range of optical samples, in particular those for which phase plays an important role in their functionality. The volume of measurements acquired thus far, allow us to claim the usefulness of our method for quality control of binary diffractive optical elements. To reach the ultimate limit of reducing the localization uncertainty within a single pixel projected on the object plane, more investigations are needed.

Bibliography

[1] Eric P. Goodwin and James C. Wyant. *Field Guide to Interferometric Optical Testing.* SPIE Field Guides. SPIE, 2006.

[2] Peter de Groot. Principles of interference microscopy for the measurement of surface topography. *Advances in Optics and Photonics*, 7(1):1, March 2015.

[3] W. Hemmert, M. S. Mermelstein, and D. M. Freeman. Nanometer resolution of three-dimensional motions using video interference microscopy. In *Technical Digest. IEEE International MEMS 99 Conference. Twelfth IEEE International Conference on Micro Electro Mechanical Systems (Cat. No.99CH36291)*, pages 302–308, January 1999.

[4] Christopher Fang-Yen, Seungeun Oh, Yongkeun Park, Wonshik Choi, Sen Song, H. Sebastian Seung, Ramachandra R. Dasari, and Michael S. Feld. Imaging voltage-dependent cell motions with heterodyne Mach-Zehnder phase microscopy. *Optics Letters*, 32(11):1572–1574, June 2007.

[5] Arnaud Dubois, Laurent Vabre, Albert-Claude Boccara, and Emmanuel Beaurepaire. High-resolution full-field optical coherence tomography with a Linnik microscope. *Applied Optics*, 41(4):805–812, February 2002.

[6] Mona Mihailescu, Mihaela Scarlat, Alexandru Gheorghiu, Julia Costescu, Mihai Kusko, Irina Alexandra Paun, and Eugen Scarlat. Automated imaging, identification, and counting of similar cells from digital hologram reconstructions. *Applied Optics*, 50(20):3589–3597, July 2011.

[7] Wonshik Choi. Tomographic phase microscopy and its biological applications. *3D Research*, 3(4):5, October 2012.

[8] Vladimir Katkovnik, Mykola Ponomarenko, and Karen Egiazarian. Lensless broadband diffractive imaging with improved depth of focus: wavefront modulation by multilevel phase masks. *Journal of Modern Optics*, 66(3):335–352, February 2019.

[9] Madeleine B. Fleming and M. C. Hutley. Blazed diffractive optics. *Applied Optics*, 36(20):4635–4643, July 1997.

[10] Arash Sabatyan and Babak Fathi. High-efficiency arrays of any desired optical beams using modified grating-based elements. *Optical and Quantum Electronics*, 50(9):338, August 2018.

[11] Luiz Goncalves Neto, Patricia S.P. Cardona, Giuseppe Antonio Cirino, Ronaldo Domingues Mansano, and Patrick B. Verdonck. Design, fabrication, and characterization of a full complex-amplitude modulation diffractive optical element. *Journal of Micro/Nanolithography, MEMS, and MOEMS*, 2(2):96–104, April 2003.

[12] Yakov G. Soskind. *Field Guide to Diffractive Optics*, volume FG21 of *SPIE Field Guides*. SPIE, 2011.

[13] M. G. Moharam, Eric B. Grann, Drew A. Pommet, and T. K. Gaylord. Formulation for stable and efficient implementation of the rigorous coupled-wave analysis of binary gratings. *Journal of the Optical Society of America A*, 12(5):1068–1076, May 1995.

[14] Philippe Lalanne and G. Michael Morris. Highly improved convergence of the coupled-wave method for TM polarization. *Journal of the Optical Society of America A*, 13(4):779–784, April 1996.

[15] Philippe Lalanne and Marie Paule Jurek. Computation of the near-field pattern with the coupled-wave method for transverse magnetic polarization. *Journal of Modern Optics*, 45(7):1357–1374, July 1998.

[16] Carsten Rockstuhl, Martin Salt, and Hans Peter Herzig. Theoretical and experimental investigation of phase singularities generated by optical micro- and nano-structures. *Journal of Optics A: Pure and Applied Optics*, 6(5):S271–S276, May 2004.

[17] Vladimir P Tychinsky. Superresolution and singularities in phase images. *Physics-Uspekhi*, 51(11):1161, 2008.

[18] Gregory J. Gbur. *Singular Optics.* Number Series in optics and optoelectronics. Taylor & Francis, 2017.

[19] Mark R. Dennis, Kevin O'Holleran, and Miles J. Padgett. Chapter 5 Singular Optics: Optical Vortices and Polarization Singularities. In E Wolf, editor, *Progress in Optics*, volume 53, pages 293–363. Elsevier, January 2009.

[20] MathWorks midcross documentation web-page.

5 Photonic nanojet study

5.1 Phenomenon description

The creation of a high-intensity spot at the shadow side of a dielectric microsphere illuminated by a plane wave was known as early as 2000 [1]. The interest in this phenomenon increased around 2004, when simulations of microspheres and microcylinders showed that it enhances the resolution of imaging systems beyond the classical diffraction limit and the back-scattering of nanoparticles [2]. This effect is referred to as photonic nanojet since. It is claimed to be non-evanescent propagating field, that can maintain a sub-wavelength full-width at half-maximum beam-width over a wavelength of propagation distance. The narrowest beam-width is often claimed to be narrower than the classical diffraction limit and since it is not a resonant phenomenon, it appears for a wide range of sizes. Once the desired size is chosen, the only constrain is that the refractive index contrast between the material and the background medium must be less than 2:1, otherwise the brightest spot appears inside the micro-sphere/cylinder.

Those properties make photonic nanojet a promising candidate for a wide range of applications, most prominent imaging and sensing. Before that however, it is necessary to study the phenomenon in terms of focusing and chromatic behavior, since those are the most useful properties of any imaging system. Although the focusing effect is similar to that of a ball-lens, the way it is created is different. For the ball-lens case, it is the propagation through the material and the shape of the lens that creates the spherical phase profile that focuses the light on the focal spot; for the photonic nanojet case though, the phase profile is created by the modes that are excited in the microsphere. Since the chromatic aberration is governed by the dispersion and thus the optical length of the material at different wavelengths, it is interesting to study the chromatic behavior of a phenomenon that is not created by propagation. Moreover, there is not a commonly accepted definition of the photonic nanojet regime. Studying the phase evolution is an alternative way to examine this problem This is the reason why we study the chromatic behavior and the focal spot of photonic nanojets.

5.2 Experiment preparation

This section briefly describes the used materials, the measuring process and the simulation method. Combining intensity and phase information provides new insight of the evolution of the phenomenon; this allows us to differentiate between the different regimes of refraction (conventional ball-lens focusing), defraction (photonic nanojet) and scattering (sub-wavelength particles) and identify their quantitative and qualitative differences. As an additional benefit, we also study how the different wavelengths affect the focusing effect.

5.2.1 Sample Preparation

The microspheres (Thermo Scientific) are made of fused silica for a diameter of (300 ± 6) nm, borosilicate glass for diameters of (2.0 ± 0.4) µm, (5.0 ± 0.5) µm, (10 ± 1) µm and (20 ± 1) µm and soda lime glass for diameters of (42.0 ± 1.1) µm and (100.0 ± 2.8) µm; their refractive index is 1.46, 1.56 and 1.52 at a wavelength of 589 nm respectively. A small amount of the spheres in powder form was dropped on a glass coverslip and beside it, a droplet of isopropanol. Using a second coverslip, the spheres were dispersed by gently sliding the two cover-glasses against each other. In the case of the 100µm spheres, they were just dropped on the slide, since they agglomerate much less. Although the position of the spheres is random, it is easy to find isolated ones for all the sizes, as shown in Fig. 5.1.

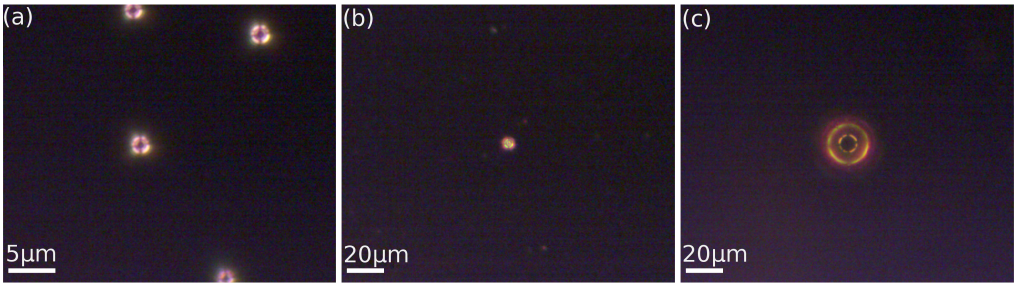

Figure 5.1 – Darkfield images of isolated microspheres of (a): 100x objective, $D = 2$ µm, (b): 20x objective, $D = 10$ µm and (c): 20x objective, $D = 20$ µm. Although the deposition process is random, finding isolated spheres is highly probable.

5.2.2 Measuring process

The area containing the spheres was first located with a low-magnification objective (10x) and once an isolated sphere was spotted the high magnification objectives were used (50x and 250x). The selected sphere was brought into focus, using white-light incoherent illumination, as shown in fig, 5.2. An image was taken with the sphere in focus in order to determine its dimension and consequently the sphere was brought in the starting position of the measurement (0.3 µm: focal plane, 2 µm and 5 µm: bottom of the spheres, 10 µm: middle of the spheres, 20 µm and 40 µm: top of the spheres, 100 µm: 14 µm for the top surface of the spheres). We choose a different starting position for the various sizes to ensure that the focal plane lies within the scanning range of the piezo-stage and can be reached within a reasonable scan-length. This was done for every wavelength, so as to ensure that every measurement starts from the same z plane. The only exception was the 100 µm diameter sphere; since the sphere is larger than the field of view of the measurement objective (50x), the plane in the middle of the sphere was identified at rim position and subsequently the center of the field was brought into the field of view, using the $x - y$ manual micro-translator. This process introduces higher uncertainties compared to the mechanical instability of the piezo-stage, that is why it was carried out only for the measurement at the first wavelength and the following measurements were taken without re-calibrating the reference plane.

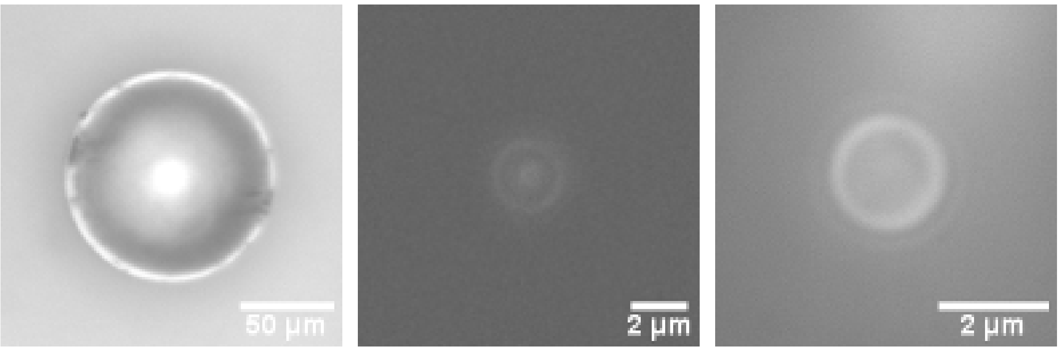

(a) $D = 100$µm sphere, 10x objective
(b) $D = 2$µm sphere, 50x objective
(c) $D = 2$µm sphere, 250x objective

Figure 5.2 – Best focus of different spheres, using appropriate objectives. Similar images for every sphere were used to have the same reference plane for all measurements.

Once the sphere has been place to the initial position, the intensity distribution along the propagation directions is measured and the focal plane is identified on the z axis, where the intensity is maximum. In order to ensure that the recorded intensity and phase, that are captured with a time difference of several minutes, correspond to the same z plane, we also run some test measurements, where we recorded the phase of the light field in the same volume. An example of such a measurement is shown in Fig. 5.3.

Most of the measurements however, were used to identify the focal distance of microspheres and capture the focal plane both in intensity and phase. For that reason, only the intensity was capture in a volumetric way, since it is straightforward to locate the focal plane from that data. Once the focal plane was known, the phase was recorded only on that plane, as shown in Fig. 5.4.

5.2.3 Simulation method

The simulations for this section were carried out using the surface integral formulation. Briefly, combining the vectorial wave equation with the dyadic Green's functions, the electric field integral equation and the magnetic field integral equation can be formulated. Those equations

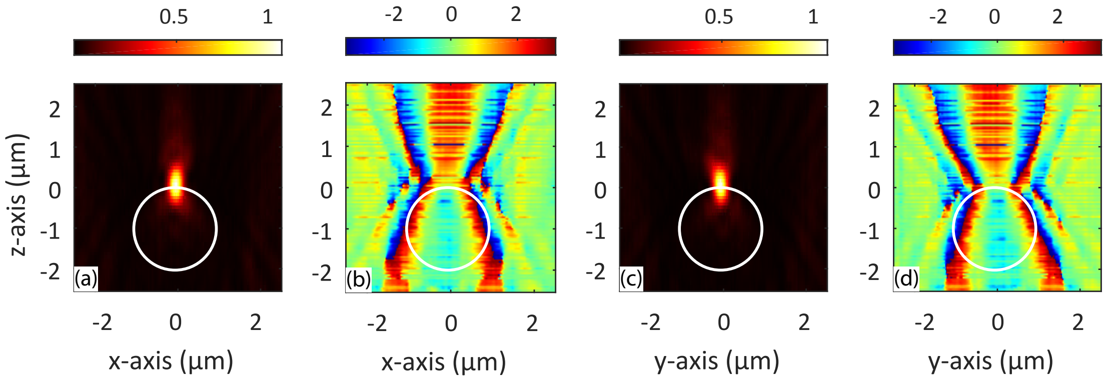

Figure 5.3 – Three dimensional measurement cross-sections. (a): intensity along x axis. (b): phase along x axis. (c): intensity along y axis. (d): phase along y axis. Those measurements were used to verify to z axis correspondence between intensity and phase data.

express the electric and magnetic fields in terms of the equivalent electric and magnetic surface currents. In a two-region space, one containing the scatterer and the other the known sources, those equivalent currents induce the same physical effects as the scatter, without representing actual current flowing on its surface; their knowledge allows us thus to calculate subsequently the total field in every position in space. The problem now becomes how to calculate the equivalent surface currents induced by the incoming field. In order to do that, the method of moments is utilized, specifically the scatterer is divided in a triangular mesh and essentially the strength of the currents on each edge of the mesh is calculated, for a given excitation. In this particular example, after finding the equivalent surface currents, we calculate the electric and magnetic field at a distance of $z = 10\,\mu\text{m}$ along the propagation direction from the center of the sphere. Subsequently we calculate the Fourier transform of the field and spatially filter out all components whose k vectors cannot be captured by the objective due to the limitation of the numerical aperture. Finally, we back-propagate the field within a given volume, which corresponds to the measured volume, and calculate the field by means of inverse Fourier transform on the filtered field.

5.3 Chromatic study

Chromatic aberrations arise from the change of the properties of the material of the lens at different wavelengths. The most important are [3]:

1. Longitudinal (axial) aberration, which caused the focal plane position to change.
2. Secondary spectrum, which is the residual error, when the axial aberration is corrected for two wavelengths.
3. Lateral color, which is caused by difference in magnification for different wavelengths.

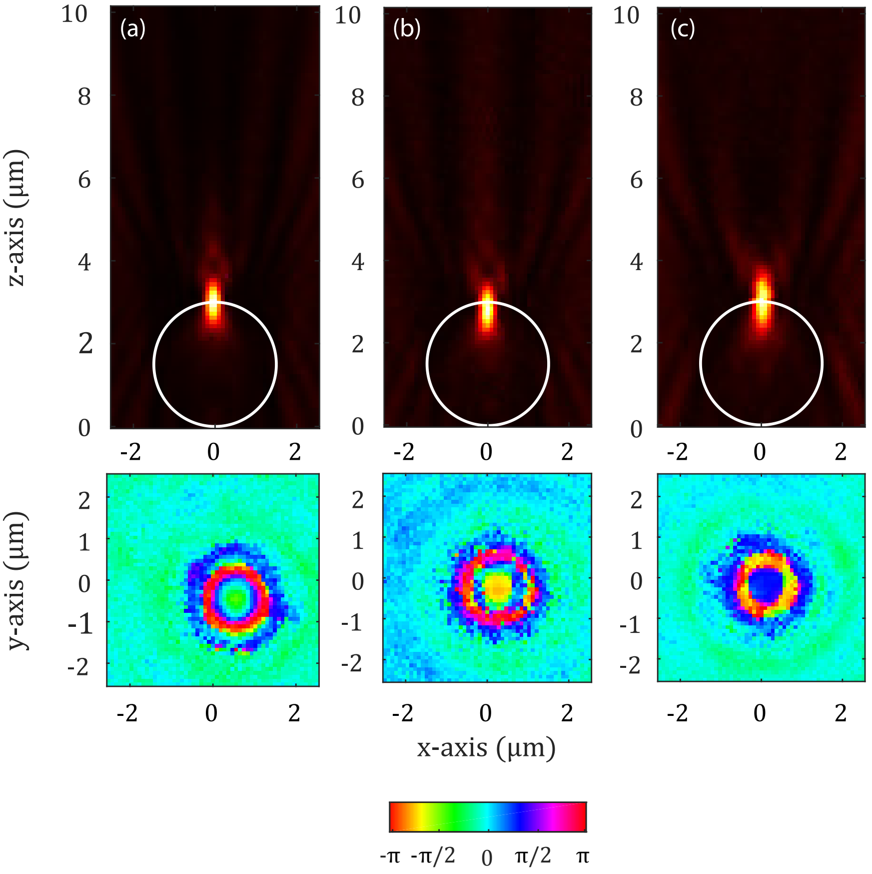

Figure 5.4 – Measurement example of a 3µm in diameter sphere for the wavelengths (a): 480 nm, (b): 532 nm and (c): 633 nm. Top row: Intensity cross-section along the center of the sphere and in the direction of propagation . Bottom row: Phase measurement on the focal plane. The slight offset of the bright spot at 532 nm is due to the measurement process (see section 5.2.2 for more details).

4. Spherochromatism, which is the variation of the spherical aberration at different wavelengths.

In this work we study the first and third case, because they have the dominant effect on the focal spot position and size. We measure the focal length at the wavelengths $\lambda =$ 480 nm, 532 nm and 633 nm, that are commonly used for apochromatic objectives corrections [3], to examine the longitudinal aberration; we also measure the focal spot at the same wavelengths to investigate the magnification dependence on the wavelength. It should be noted that the measurements are limited by the objective corrections. As mentioned before, we use an apochromatic objective, that offers the best chromatic and spherical aberrations corrections within the visible. Still, we limit the measurements in the spectral range from 480 nm to 650 nm to ensure that we are within the best corrected spectral range of the instrument.

5.3.1 Longitudinal Aberration and Secondary Spectrum

Using the paraxial approximation, it can be shown that the effective focal length f, measured from the top of a ball-lens is given by [4]:

$$f = \frac{nR}{2(n-1)} - R, \tag{5.1}$$

where n is the refractive index of the lens, R is its radius and the surrounding medium is assumed to be air. Considering two different wavelengths, λ_1 and λ_2, the difference in the focal length can be found, using Eg.5.1, as:

$$\Delta f = \frac{R}{2} \frac{-\Delta n}{(n_1-1)(n_2-1)}, \tag{5.2}$$

where $\Delta f = f_2 - f_1$, $\Delta n = n_2 - n_1$ and the subscripts refer to the different wavelengths. Taking an N-BK7 ball-lens of 100 µm in diameter for example, at the wavelengths $\lambda_1 = 450\,\text{nm}$ ($n_1 = 1.5253$) and $\lambda_2 = 808\,\text{nm}$ ($n_2 = 1.5106$), the focal shift is found: $\Delta f = 1.37\,\mu\text{m}$. Given the fact that the highest numerical aperture of such a lens is about 0.55, the focal shift is smaller than the depth of focus ($\approx 1.65\,\mu\text{m}$), so such a component can be considered achromatic. In Fig. 5.5 we plot the back focal plane of four spheres of different size, namely $D = 2.2\,\mu\text{m}$, 6.1 µm, 42.2 µm and 106 µm, as predicted by eq. 5.1 (dotted line) and as measured (solid line). We see that for the two smallest spheres the change in the focal distance is negligible, and becomes more pronounced as the size of the sphere increases. The solid lines are the best (linear) fit to the recorded values. Please note that the measurement for the small spheres starts from their bottom surface, as previously described. In order to extract the back focal length, the diameter of the spheres is subtracted from the distance until the maximum intensity plane. This results in the negative values because of the following reasons: a) estimation of dimension of the particle, b) focusing errors, c) depth of focus of objective, and d) discretization of measurement along propagation direction.

Another way to represent this information is shown in Fig. 5.6, where the back focal length for 3 different wavelengths is plotted against the radius of the spheres. We note that for spheres of diameter $D \leq 6\,\mu\text{m}$ the focal spot appears practically on their surface, while it moves to larger z values as the size of the spheres increases. This feature can be used to define the photonic nanojet regime, namely when the focal plane moves more that 1 µm from the surface of the sphere. In this example, this would put the limit of the photonic nanojet around a diameter of $D \approx 7\,\mu\text{m}$. The inset of Fig. 5.6 shows the same information for a larger range of diameters and is consistent with the predicted behavior; the focal plane moves away from the surface of the sphere in general, and for a specific diameter, the shortest wavelengths are focused closer to the surface.

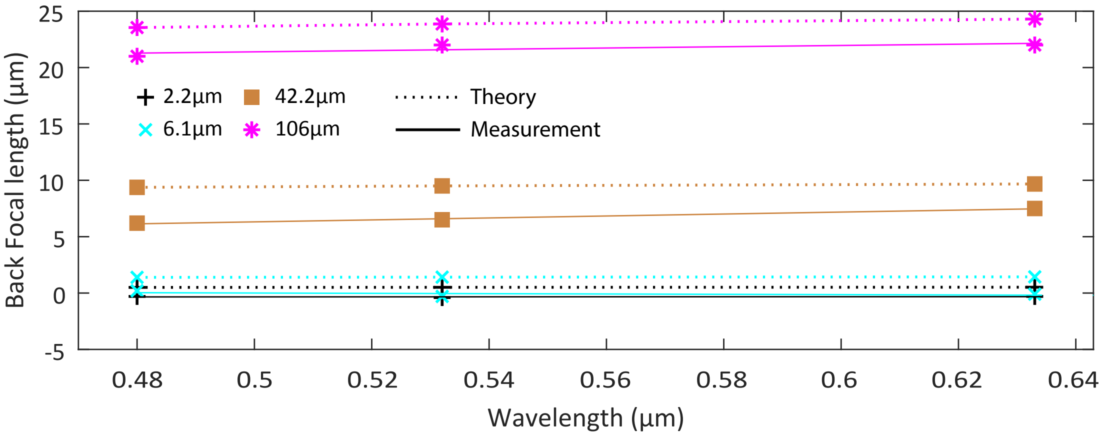

Figure 5.5 – Back focal length value according to (dotted line) theory and (solid line) measurement against wavelength, for spheres of different diameter. The solid lines are best fits to the experimental points. The focal plane shift is negligible for the small spheres and becomes more pronounced as the diameter of the sphere increases.

5.3.2 Lateral Colour Aberration

In order to investigate the lateral colour aberration, we measure the full width at half maximum of the maximum intensity spot and show the results in Fig. 5.7. In this figure, the measured spot size along the x (polarization direction) and y axis for 3 different wavelengths against the diameter of the sphere is plotted. As expected, the spot size is proportional to the wavelength [5]. We also note, that for spheres with $D < 20\,\mu\text{m}$, the spot size remains almost constant, and it is actually limited by the resolution of the imaging system; this indicates that photonic nanojets have a high numerical aperture, comparable with that of the used (50x/0.9) objective. As the diameter becomes larger, so does the spot size and becomes resolvable by the imaging system, indicating a drop in the numerical aperture as well. Moreover, the measured spot size along the two different directions x and y are not equal, which is the asymmetry due to polarization.

5.4 Focal plane study

In this section, we investigate the focal spot created by two different microspheres – one with diameter $D = 2\,\mu\text{m}$ and another with $D = 0.3\,\mu\text{m}$ – for different wavelengths ($\lambda = 500\,\text{nm}$, 600 nm and 700 nm). Those wavelengths span most of the visible spectrum and they do not need to coincide with those traditionally used for chromatic studies of lenses, since we are interested in a different aspect of the phenomenon. The larger sphere lies within the photonic nanojet regime and gives a completely evolved focal spot; the smaller sphere however operates in the scattering regime and affects the incoming light only weakly. Therefore we can extract some qualitative and quantitative information about the behavior of the spot size as we change the operating regime. Understanding the weak effect of the small spheres is also important,

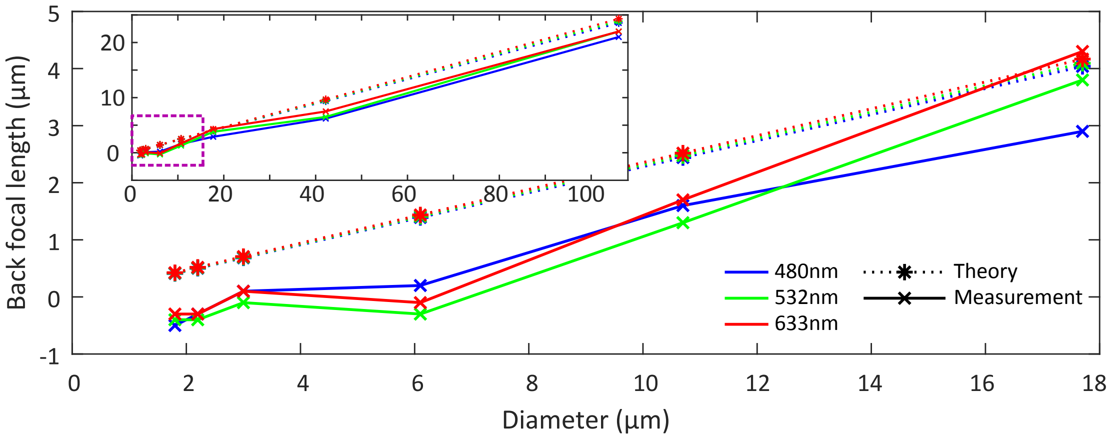

Figure 5.6 – Back focal length value for 3 different wavelengths, according to (dotted line) theory and (solid line) measurement, against the diameter of the spheres. The solid lines are a guide to the eye, connecting the measurement points (crosses). At $D \approx 7\,\mu\text{m}$ the focal plane moves clearly away from the surface of the sphere, which can define the photonic nanojet regime. The inset shows the same information for a larger range of diameters, showing consistent behavior.

because we will study particles having comparable sizes later on. First we simulate the field within a volume around the scatterer, as described before, and then we identify the focal plane as the z position, where the intensity acquires its maximum value. We only show this plane here. The incident illumination, both in simulation and experiment, is polarized along the x axis.

5.4.1 First sample: 2 micrometers sphere

Simulations – 2 micrometers

The simulations results are shown in Figs. 5.8 - 5.10 for $\lambda =$ 500 nm to 700 nm respectively. For the intensity case, we fit each cross-section to the Airy disk function:

$$A(\rho) = \left| 2\frac{J_1(\rho)}{\rho} \right|^2, \tag{5.3}$$

where ρ indicates the position on the observation plane, in order to visualize their similarity. The size of the focal spot is calculated from the simulated intensity values, using the full width at half maximum criterion. In the case of the phase, we want to identify the area, where the phase has minimal fluctuations, since those areas are found within consecutive disk of the Airy pattern. In order to do that, we first calculate the derivative of the wrapped phase and then we locate the points, where the derivative is close to the maximum value. An ellipse is then fitted to those points, whose diameters give the spot size in phase. We used the points that are above 90% of the maximum value (solid black ellipses) and those that lie between

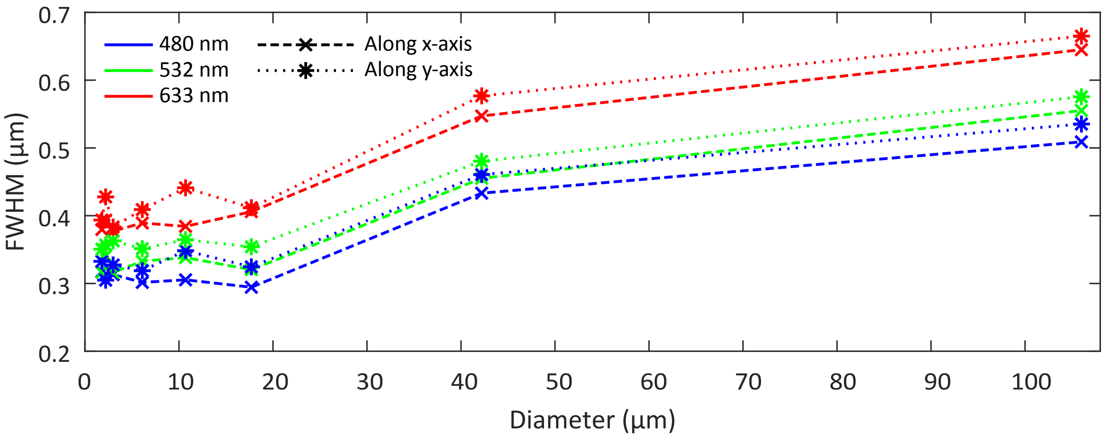

Figure 5.7 – Measured spot size for 3 wavelengths along the (dashed line) x and (dotted line) y axis against the diameter of the spheres. For spheres of $D < 20\,\mu\text{m}$ the spot size measurement is diffraction-limited, indicated a high numerical aperture, which drops for larger spheres. The spot size is proportional to the wavelength and asymmetric, due to polarization.

20% – 90% (dashed white ellipses).

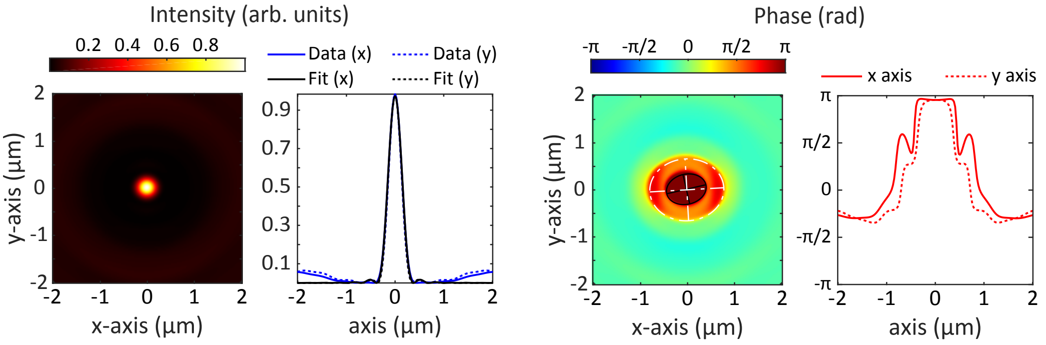

(a) Simulated intensity at focal plane.

(b) Simulated phase at focal plane.

Figure 5.8 – Simulation results for a dielectric sphere of diameter $D = 2\,\mu\text{m}$ at the wavelength of $\lambda = 500\,\text{nm}$. (a): Intensity. (Left): focal plane. (Right): Cross-section along x and y axis and the respective Airy function fits. (b): Phase. (Left): focal plane. (Right): Cross-section along x and y axis.

All the cross-sections are summarized in Fig. 5.11, where the intensity and phase profiles are shown along both directions for the wavelengths of $\lambda = 500\,\text{nm}$ to 700 nm in panels (a) - (c) respectively. We note that the phase profiles have more pronounced asymmetry compared to the intensity ones. Additionally, the shoulders of the phase profile appear at the positions where the intensity drops to zero, which is expected to create a distinct point. Also, comparing the phase profiles, we note that the shape is easier distinguishable among the different wavelengths as well; the amount of the accumulated phase also changes, with more than π at $\lambda = 500\,\text{nm}$ to $\pi/2$ for the wavelengths of $\lambda = 600\,\text{nm}$ and 700 nm. At shorter wavelengths, the optical path inside the sphere is longer, both due to the higher refractive index and the larger

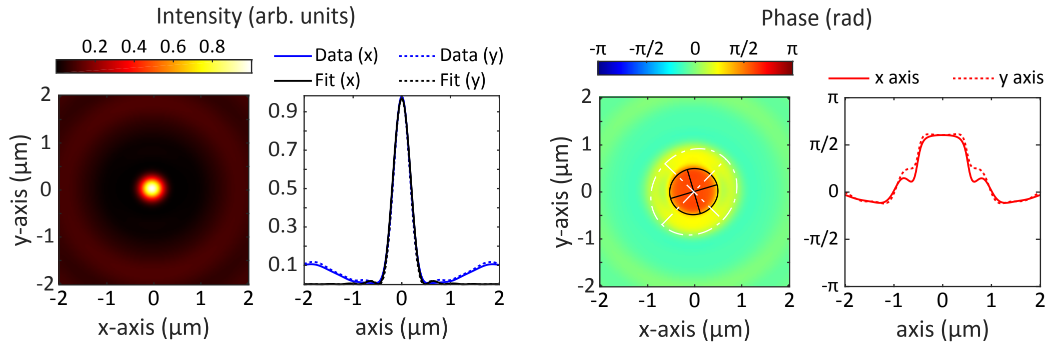

(a) Simulated intensity at focal plane.

(b) Simulated phase at focal plane.

Figure 5.9 – Simulation results for a dielectric sphere of diameter $D = 2\,\mu\text{m}$ at the wavelength of $\lambda = 600\,\text{nm}$. (a): Intensity. (Left): focal plane. (Right): Cross-section along x and y axis and the respective Airy function fits. (b): Phase. (Left): focal plane. (Right): Cross-section along x and y axis.

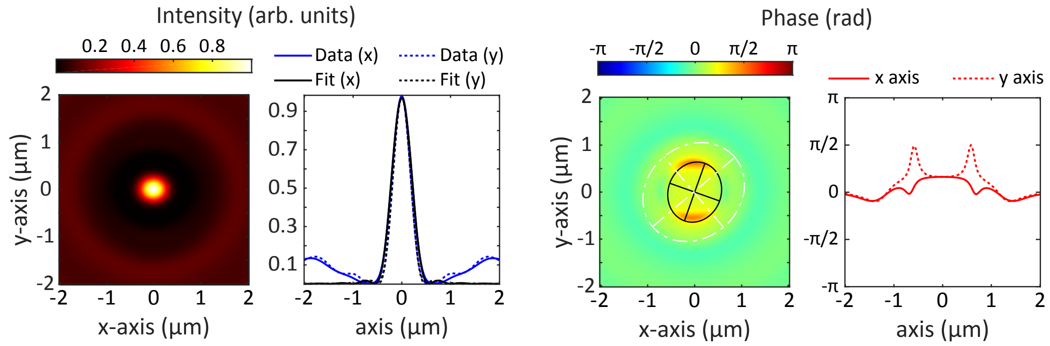

(a) Simulated intensity at focal plane.

(b) Simulated phase at focal plane.

Figure 5.10 – Simulation results for a dielectric sphere of diameter $D = 2\,\mu\text{m}$ at the wavelength of $\lambda = 700\,\text{nm}$. (a): Intensity. (Left): focal plane. (Right): Cross-section along x and y axis and the respective Airy function fits. (b): Phase. (Left): focal plane. (Right): Cross-section along x and y axis.

size of the sphere relative to the wavelength; the accumulated phase of the light as it passes through the sphere is expected to be reduced. It is worth noting that the changes in the phase profiles are more pronounced, compared to the intensity ones, as the wavelength increases, i.e. we move towards the scattering regime.

Measurements – 2 micrometer

Figures 5.12 to 5.14 show the measurements results for the wavelengths of $\lambda = 500\,\text{nm}$ to $700\,\text{nm}$ respectively, where the raw data are used. As was described previously, the intensity profile was fitted to an Airy function, while the phase spot was initially determined by the derivative of the wrapped phase. Because of the noise in the captured data though, the intervals that were used to identify the greatest slope of the phase had to be determined for

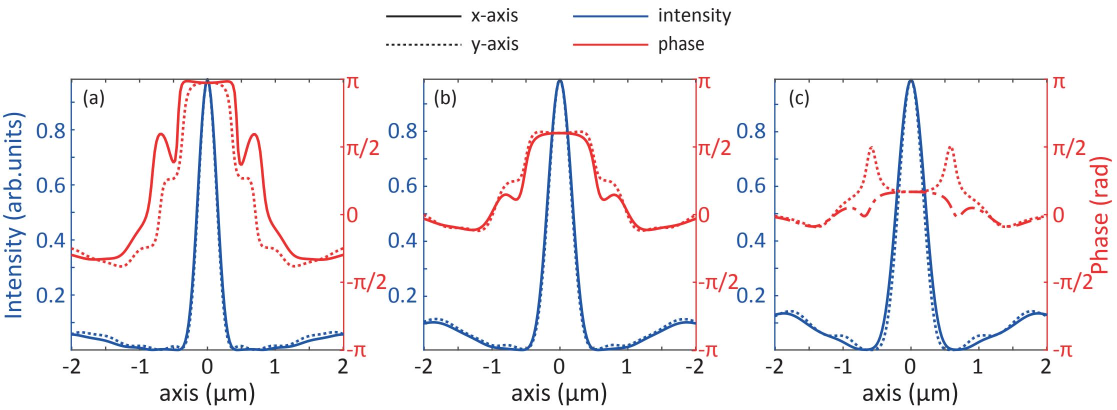

Figure 5.11 – Comparison of simulated results of a $D = 2\,\mu\text{m}$ sphere at wavelengths (a): $\lambda = 500\,\text{nm}$, (b): $\lambda = 600\,\text{nm}$ and (c): $\lambda = 700\,\text{nm}$.

each wavelength individually. For that reason, we chose to extract the spot size in phase using the minima values of the cross-sections. Since the simulations do not show such points, we used their derivatives to find the positions of the shoulders and that is the spot size we kept for comparison purposes.

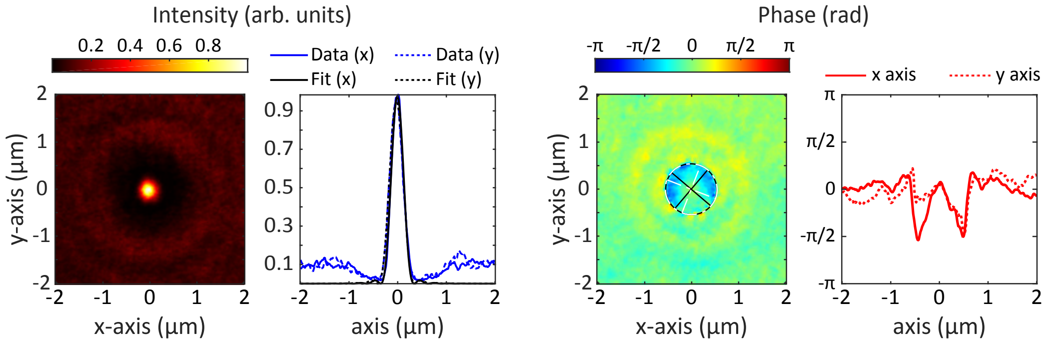

(a) Measured intensity at focal plane.

(b) Measured phase at focal plane.

Figure 5.12 – Measured results for a dielectric sphere of diameter $D = 2\,\mu\text{m}$ at the wavelength of $\lambda = 500\,\text{nm}$. (a): Intensity. (Left): focal plane. (Right): Cross-section along x and y axis and the respective Airy function fits. (b): Phase. (Left): focal plane. (Right): Cross-section along x and y axis.

The measured cross-sections along the two directions x and y for the wavelengths $\lambda = 500\,\text{nm}$ to 700 nm are shown in Fig. 5.15(a) - 5.15(c) respectively. The phase profiles are more symmetric, compared to simulations of Fig. 5.11. We note however, that the distinct points of the phase coincide with the minima of the intensity. Also, the shape of the phase profile at $\lambda = 700\,\text{nm}$ is distinct from the other two cases, which have similar shapes.

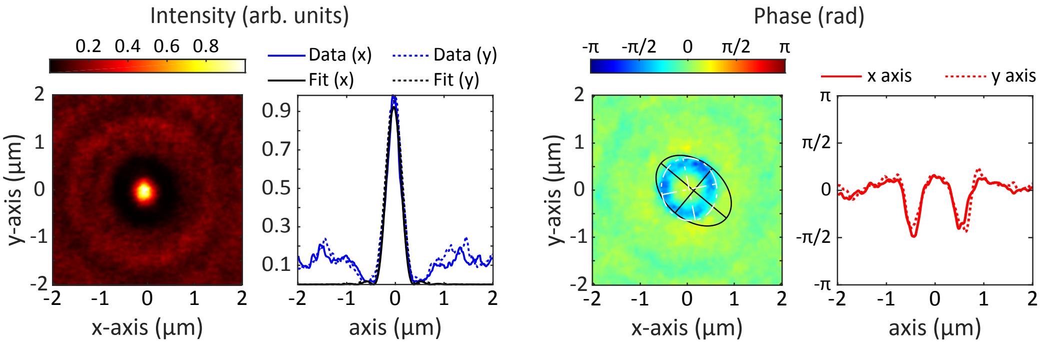

(a) Measured intensity at focal plane.

(b) Measured phase at focal plane.

Figure 5.13 – Measured results for a dielectric sphere of diameter $D = 2\,\mu m$ at the wavelength of $\lambda = 600\,nm$. (a): Intensity. (Left): focal plane. (Right): Cross-section along x and y axis and the respective Airy function fits. (b): Phase. (Left): focal plane. (Right): Cross-section along x and y axis.

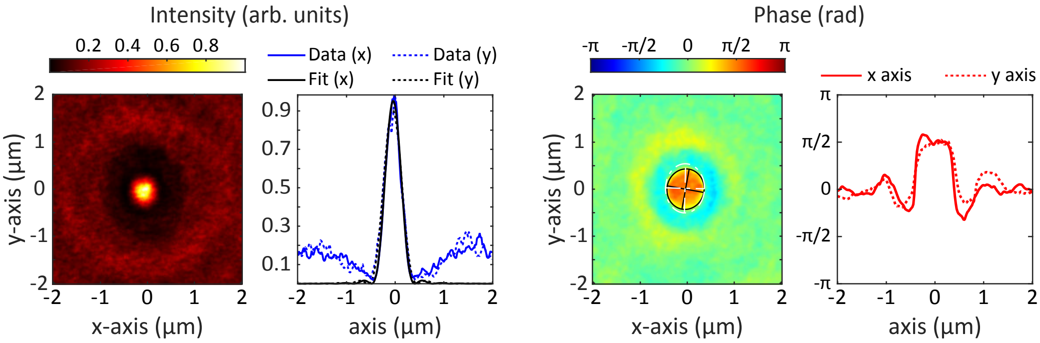

(a) Measured intensity at focal plane.

(b) Measured phase at focal plane.

Figure 5.14 – Measured results for a dielectric sphere of diameter $D = 2\,\mu m$ at the wavelength of $\lambda = 700\,nm$. (a): Intensity. (Left): focal plane. (Right): Cross-section along x and y axis and the respective Airy function fits. (b): Phase. (Left): focal plane. (Right): Cross-section along x and y axis.

Spot size comparison – 2 micrometers

The extracted focal spot sizes are summarized in tables 5.1 and 5.2 for the x and y axis respectively. The last column contains the ratio of the simulated values over the measured ones, to quantify how closely each domain (intensity and phase) corresponds to the simulations. The asymmetry of the focal spot is captured by the measurements as well. It is curious that the recorded spot size is, at times, smaller than the simulated one, although uncertainties in the exact dimensions and the refractive index of the measured sphere could attribute such small variations.

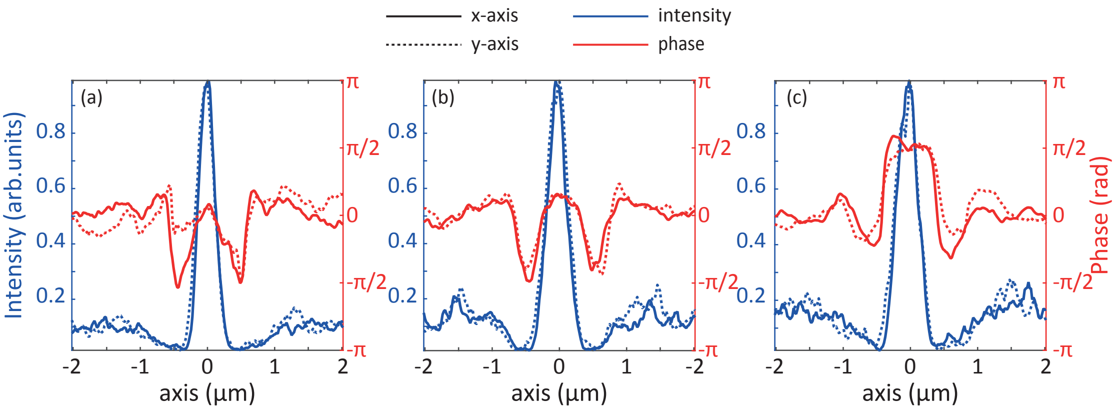

Figure 5.15 – Comparison of measured results of a $D = 2\,\mu\text{m}$ sphere at wavelengths (a): $\lambda = 500\,\text{nm}$, (b): $\lambda = 600\,\text{nm}$ and (c): $\lambda = 700\,\text{nm}$.

Table 5.1 – Spot size along x for the $2\,\mu\text{m}$ sphere

	Spot Size (μm)					
	Intensity		*Phase*		*Ratio*	
λ (nm)	*Sim*	*Exp*	*Sim*	*Exp*	*Int*	*Phase*
500	0.316	0.286	0.878	0.934	1.10	0.94
600	0.397	0.316	1.028	0.934	1.26	1.10
700	0.457	0.366	1.354	1.140	1.25	1.19

5.4.2 Second sample: 0.3 micrometers sphere

Simulations – 0.3 micrometers

The simulated results of the case of the sphere with diameter $D = 0.3\,\mu\text{m}$ are shown in Figs. 5.16 - 5.18. We should point out that a constant value has been subtracted from every intensity profile, to make its minimum value zero. This can also be seen from the Airy disk fits, that are translated along the intensity axis, indicating a constant term added to the eq. 5.3. This allows us to use the full width at half maximum criterion to calculate the spot width, otherwise the intensity value does not reach 50 % of its maximum value. The region of the flattest phase

Table 5.2 – Spot size along y for the $2\,\mu\text{m}$ sphere

	Spot Size (μm)					
	Intensity		*Phase*		*Ratio*	
λ (nm)	*Sim*	*Exp*	*Sim*	*Exp*	*Int*	*Phase*
500	0.300	0.315	0.727	0.990	0.95	0.73
600	0.377	0.369	0.978	1.121	1.02	0.87
700	0.401	0.382	1.154	1.308	1.05	0.88

was estimated as described previously, for the $D = 2\,\mu\text{m}$ case. However, the change is so little and the profile resembles a bell, so, in the end the minima of the profiles were used for the phase spot size calculation. In order to ease the comparison with the measured profiles, the minimum phase value was set to zero, which corresponds to the data processing procedure.

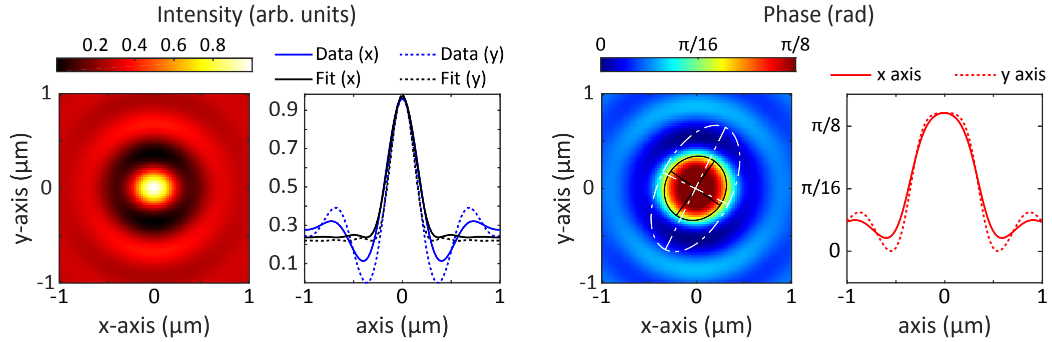

(a) Simulated intensity at focal plane.

(b) Simulated phase at focal plane

Figure 5.16 – Simulated results for a dielectric sphere of diameter $D = 0.3\,\mu\text{m}$ at the wavelength of $\lambda = 500\,\text{nm}$. (a): Intensity. (Left): focal plane. (Right): Cross-section along x and y axis and the respective Airy function fits. (b): Phase. (Left): focal plane. (Right): Cross-section along x and y axis.

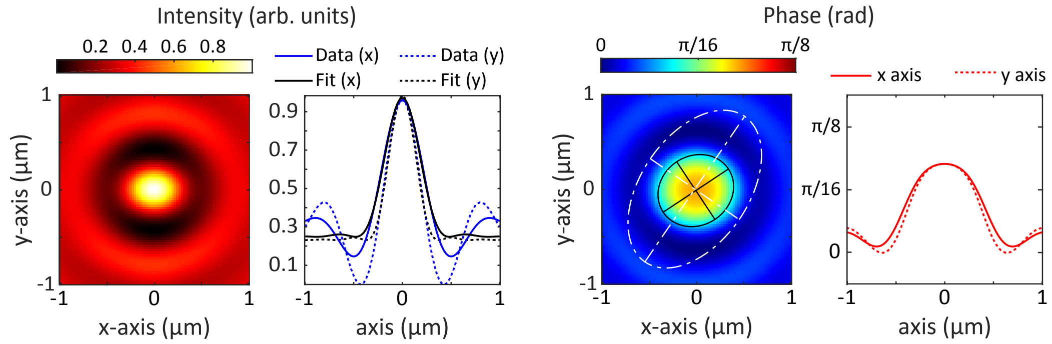

(a) Simulated intensity at focal plane.

(b) Simulated phase at focal plane.

Figure 5.17 – Simulated results for a dielectric sphere of diameter $D = 0.3\,\mu\text{m}$ at the wavelength of $\lambda = 600\,\text{nm}$. (a): Intensity. (Left): focal plane. (Right): Cross-section along x and y axis and the respective Airy function fits. (b): Phase. (Left): focal plane. (Right): Cross-section along x and y axis.

Figure 5.19 summarizes all the simulated results; the intensity and phase profiles are shown along both directions for the wavelengths of $\lambda = 500\,\text{nm}$ to $700\,\text{nm}$ in panels (a) - (c) respectively. Regarding the intensity, we note that the asymmetry is more pronounced. This is not the case for the phase profiles, which look similar and have, generally the same shape. Additionally, the phase variation is much smaller and the phase shoulders do not coincide with the minima of the intensity. That is not surprising, since the intensity does not drop to zero, it is only the result of the specific representation. The intensity does not drop to zero, because the sphere is so small that it cannot induce enough phase retardation for complete

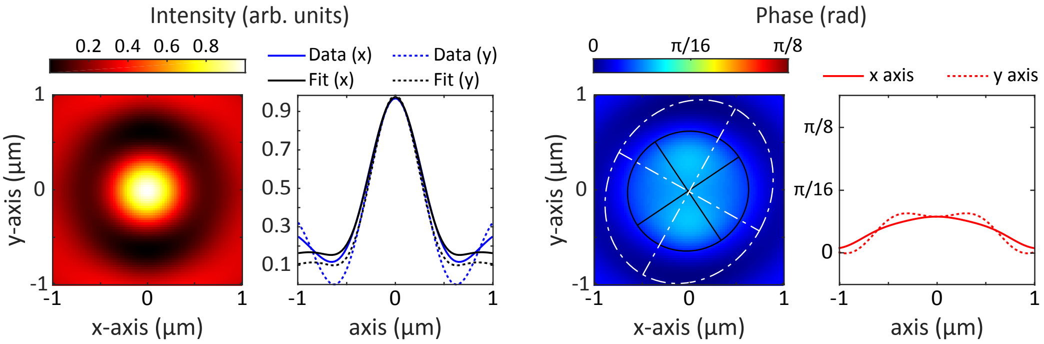

(a) Simulated intensity at focal plane.

(b) Simulated phase at focal plane.

Figure 5.18 – Simulated results for a dielectric sphere of diameter $D = 0.3\,\mu\mathrm{m}$ at the wavelength of $\lambda = 700\,\mathrm{nm}$. (a): Intensity. (Left): focal plane. (Right): Cross-section along x and y axis and the respective Airy function fits. (b): Phase. (Left): focal plane. (Right): Cross-section along x and y axis.

destructive interference to take place. The focusing effect is not fully developed, thus the Airy pattern is superimposed on a constant value and the intensity never drops to zero.

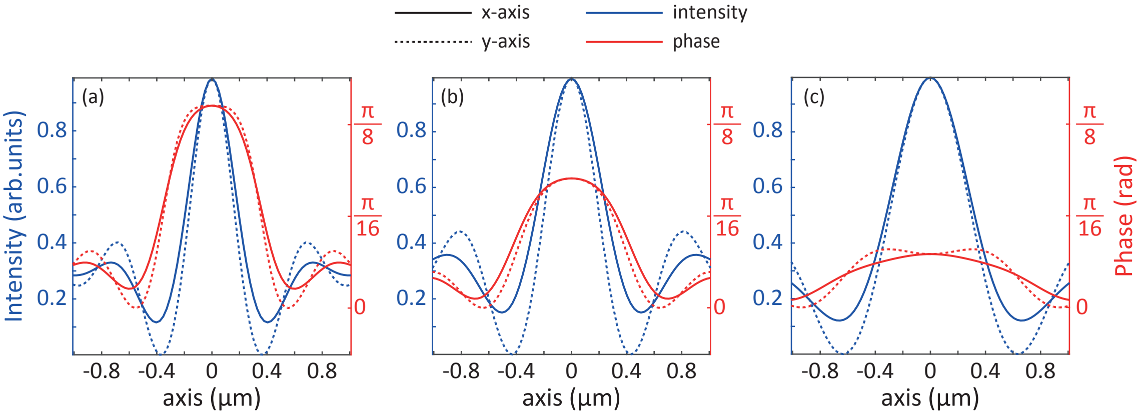

Figure 5.19 – Comparison of simulated results of a $D = 0.3\,\mu\mathrm{m}$ sphere at wavelengths (a): $\lambda = 500\,\mathrm{nm}$, (b): $\lambda = 600\,\mathrm{nm}$ and (c): $\lambda = 700\,\mathrm{nm}$.

Measurements – 0.3 micrometers

The measurements results for the $0.3\,\mu\mathrm{m}$ sphere are shown in Figs. 5.20 to 5.22 for $\lambda = 500\,\mathrm{nm}$ to $700\,\mathrm{nm}$ respectively. In this case however, the signal was too weak, so that data where processed according to the procedure described in chapter 2. Additionally, the minimum value was set to zero, so as the data to be represented in the same way as it was done for the simulations. The Airy disk fit again indicates this fact by the constant term that need to be added. As far as the phase is concerned, we show again the ellipses that were fitted using the maximum wrapped phase derivatives values. However, for the purpose of defining the phase spot size, the maxima values were used for the same reasons described in the simulation part.

Of note is also the very small variation in the phase values, that is comparable to the simulated results.

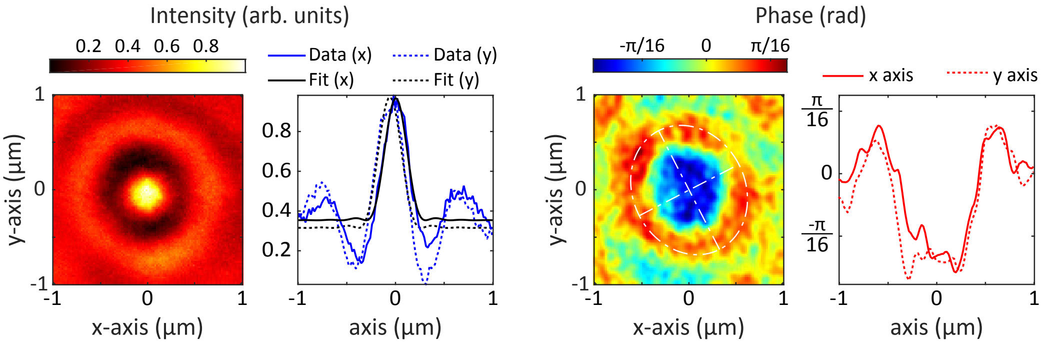

(a) Measured intensity at focal plane.

(b) Measured phase at focal plane.

Figure 5.20 – Measured results for a dielectric sphere of diameter $D = 0.3\,\mu\text{m}$ at the wavelength of $\lambda = 500\,\text{nm}$. (a): Intensity. (Left): focal plane. (Right): Cross-section along x and y axis and the respective Airy function fits. (b): Phase. (Left): focal plane. (Right): Cross-section along x and y axis.

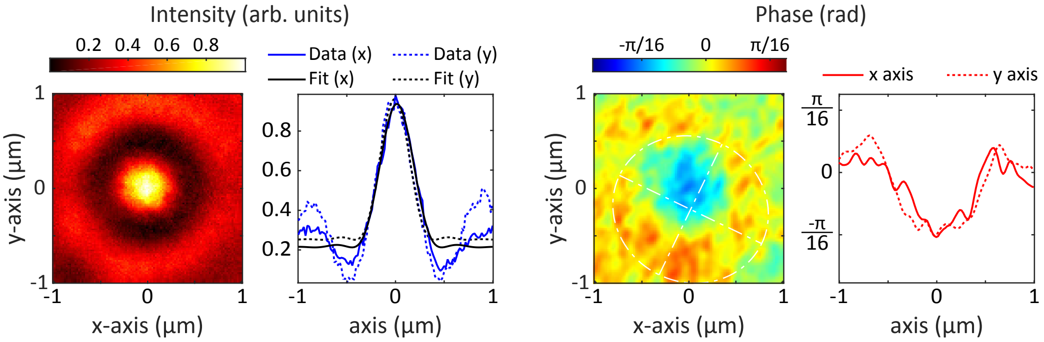

(a) Measured intensity at focal plane.

(b) Measured phase at focal plane.

Figure 5.21 – Measured results for a dielectric sphere of diameter $D = 0.3\,\mu\text{m}$ at the wavelength of $\lambda = 600\,\text{nm}$. (a): Intensity. (Left): focal plane. (Right): Cross-section along x and y axis and the respective Airy function fits. (b): Phase. (Left): focal plane. (Right): Cross-section along x and y axis.

We summarize the measured cross-sections along the two directions x and y for the wavelengths $\lambda =$;500 nm to 700 nm Fig. 5.23(a) - 5.23(c) respectively. As was mentioned previously, the asymmetry, especially in the phase profiles, is much reduced compared to the $D = 2\,\mu\text{m}$ case. The lobes of the intensity and the phase variations are comparable to those shown in the simulation case, as is the fact that the distinct points (maxima) of the phase profiles do not coincide with the minima of the intensity.

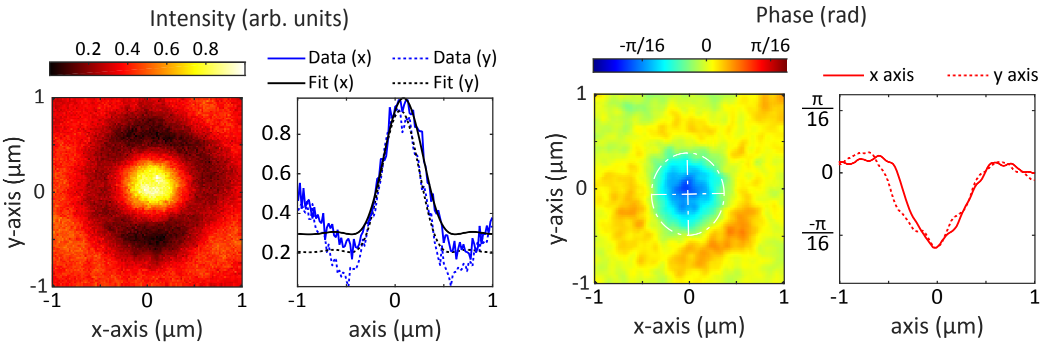

(a) Measured intensity at focal plane.

(b) Measured phase at focal plane.

Figure 5.22 – Measured results for a dielectric sphere of diameter $D = 0.3\,\mu\text{m}$ at the wavelength of $\lambda = 700\,\text{nm}$. (a): Intensity. (Left): focal plane. (Right): Cross-section along x and y axis and the respective Airy function fits. (b): Phase. (Left): focal plane. (Right): Cross-section along x and y axis.

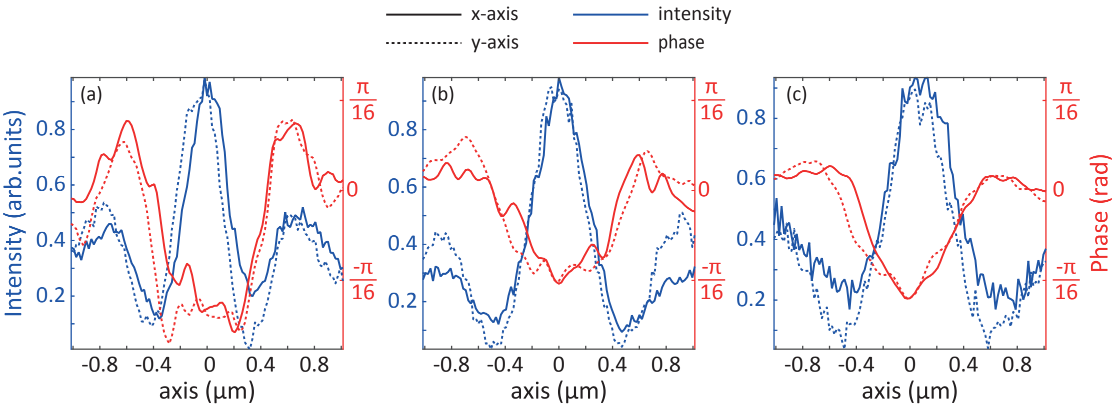

Figure 5.23 – Comparison of measured results of a $D = 0.3\,\mu\text{m}$ sphere at wavelengths (a): $\lambda = 500\,\text{nm}$, (b): $\lambda = 600\,\text{nm}$ and (c): $\lambda = 700\,\text{nm}$.

Spot size comparison – 0.3 micrometers

The extracted values of the spot size are summarized in tables 5.3 and 5.4 along the x and y axis respectively. As was the case with the sphere of diameter $D = 2\,\mu\text{m}$, the measured spot size is smaller than the simulated one, especially along the polarization axis x. However, the difference is a few tenths of nanometers and since we are examining a single measurement, we cannot conclude any trends.

5.5 Photonic nanojet conclusions

The shown results can be summarized in the following fashion. Regarding the chromatic behavior of the phenomenon, all the sphere studied in this work can be regarded as achromatic, in the sense of focal plane shift. However, a limit can be set at spheres with diameters smaller

Table 5.3 – Spot size along x for the 0.3 µm sphere

	Spot Size (µm)					
	Intensity		*Phase*		*Ratio*	
λ (nm)	*Sim*	*Exp*	*Sim*	*Exp*	*Int*	*Phase*
500	0.391	0.356	1.211	1.126	1.10	1.08
600	0.519	0.474	1.413	1.164	1.09	1.21
700	0.637	0.580	2.000	1.201	1.10	1.67

Table 5.4 – Spot size along y for the 0.3 µm sphere

	Spot Size (µm)					
	Intensity		*Phase*		*Ratio*	
λ (nm)	*Sim*	*Exp*	*Sim*	*Exp*	*Int*	*Phase*
500	0.332	0.365	1.110	1.183	0.91	0.94
600	0.401	0.453	1.262	1.352	0.89	0.93
700	0.593	0.522	1.867	1.352	1.14	1.38

that $D \approx 7$µm, that focus the incoming beam on their surface. The spot size evolution is diffraction limited for larger diameters, indicating a high numerical aperture of the photonic nanojets. As the diameter is increased beyond the diameter of $D > 20$µm, the spot size is increased (Fig. 5.7), indicating a reduced numerical aperture, which is expected to continue diminishing, until it reaches the ball-lens focusing.

Examining the focal plane of small spheres reveals that for spheres having a diameter in the range of a few microns, creates a focal spot that resembles the Airy function. Consequently, the intensity profile remains similar, and does not indicate any change in the behavior. However, the phase map is more sensitive to polarization and wavelength, as was shown in the simulations for the $D = 2$µm sphere. The experiments also showed a change of the profiles, that is more pronounced in the phase regime, indicating a qualitative alternation in the evolution of the behavior. In order to study the behavior of a scattering object and compare it to the defractive nature of the photonic nanojet, we move to smaller diameters, namely $D = 0.3$µm. In this case, we acquired qualitatively different results, both in simulations and experiments, compared to the larger diameter sphere. In the intensity regime, that was demonstrated by the fact that the intensity does not go zero, the focal spot is superimposed to a constant value. Still, the intensity profile resembles the one acquired from the $D = 2$µm sphere. The phase profiles on the other hand, show an overall different shape. Using the shape of the phase profiles might be a more precise way to set a lower limit to the photonic nanojet regime and the crossing to the scattering behavior. The agreement between the simulated and measured results is mainly seen in the general trend of the measurements and not in the details. A way of defining the phase spot size more accurately can help in this regard. The study of the $D = 0.3$ µm sphere, which operates in the scattering regime, also showed how weakly it affects the incoming illumination and the challenges it poses to recording and analyzing the data. We address those challenges in the next chapter, where we examine particles and structures of similar dimensions (≈300 nm) and show how we can deduce some properties of the particles from the scattered field.

Bibliography

[1] H.-J. Münzer, M. Mosbacher, M. Bertsch, J. Zimmermann, P. Leiderer, and J. Boneberg. Local field enhancement effects for nanostructuring of surfaces. *Journal of Microscopy*, 202(1):129–135, December 2001.

[2] Zhigang Chen, Allen Taflove, and Vadim Backman. Photonic nanojet enhancement of backscattering of light by nanoparticles: a potential novel visible-light ultramicroscopy technique. *Optics Express*, 12(7):1214–1220, April 2004.

[3] Herbert Gross, Hannfried Zuegge, Martin Peschka, and Fritz Blechinger. *Handbook fo Optical Systems: Volume 3: Aberration Theory and Correction of Optical Systems*, volume 3. WILEY-VCH Verlag GmbH, September 2105.

[4] Myun-Sik Kim, Toralf Scharf, Stefan Mühlig, Martin Fruhnert, Carsten Rockstuhl, Roland Bitterli, Wilfried Noell, Reinhard Voelkel, and Hans Peter Herzig. Refraction limit of miniaturized optical systems: a ball-lens example. *Optics Express*, 24(7):6996–7005, April 2016.

[5] Sylvain Lecler, Yoshitate Takakura, and Patrick Meyrueis. Properties of a three-dimensional photonic jet. *Optics Letters*, 30(19):2641–2643, October 2005.

6 Single nano-sized particles study by scattered light

6.1 Introduction to the examined particles

The concept of materials that possess negative permittivity ϵ and permeability μ was first proposed by Veselago [1], more than forty years ago, and gave birth to the field of meta-materials. Since then, the field has made tremendous progress and has expanded to include any artificially fabricated material whose response can be engineered according to some design. The response is shaped by changing, on a length-scale smaller than the wavelength of operation, the topography of the structure, most of the times consisting of simpler building blocks.

Naturally, the first meta-materials were demonstrated at microwave frequencies [2] and were periodic, non-isotropic structures, fabricated by top-down techniques. The advances in nanofabrication, especially combining different materials, allowed to downscale those structures to operate at optical frequencies[3, 4], however the fabrication challenges remain. The techniques used for the fabrication (electron beam lithography, focused ion beam milling) are slow, expensive and limited to planar structures[5, 6]. Fabricating real three-dimensional materials with such techniques adds alignment problems and the end results is very sensitive to fabrication errors. What is more, the anisotropy remains, since those structures are essentially stratified media.

Those problems were addressed with the development of bottom-up techniques, based on chemical engineering or self-assembly methods. Such methods can be used to fabricate real three dimensional, isotropic materials with the trade-off of limited control over the macroscopic arrangement of the final structure [7]. In a strongly diluted scenario, the response of the bulk self-assembled metamaterials can be derived directly from the response of its constituent meta-atoms [8, 9]. This means that, by understanding the response of a single meta-atom, the response of the whole three-dimensional metamaterials can be understood. That is the purpose of this study. The most promising candidates are isotropic meta-atom in the form of core-shell cluster meta-atom [10]. They consists of a dielectric spherical core, surrounded by plasmonic nanoparticles, that are attached on the core in an isotropic, yet disordered fashion. For the optimization of the fabrication process, the assessment of the structure is necessary, which is mostly done by imaging the sample with electron microscopy. Resonance properties are usually measured by the transmission through a diluted solution.

Frequently used imaging techniques include electron microscopy (SEM, TEM) or near-field microscopy (SNOM). The former techniques reveal the structural integrity of the sample, they cannot capture its optical properties though. The near-field microscopes, although they show the geometry and the optical response of the sample, they tend to be slow and strenuous to carry out. Lastly, characterization through transmittance shows the optical properties, but it cannot link the individual to the collective response. In this chapter, we use optical interference microscopy, as implemented by our set-up, to characterize and differentiate between individual nano-sized particles and meat-atoms. We capture the intensity and phase information of the transmitted field, onto which the optical properties of the sample are imprinted, utilizing the spectral resolution of our set-up a well. A high magnification objective allows us to study single meta-atoms that are frequently inaccessible. We start by demonstrating the measurement technique using simple dielectric and metallic spheres and then we move on to study the core-shell cluster meta-atom, by comparing the results with simulations and the simple structures.

6.2 Methodology description

Within the framework of this study, we show a time-efficient and convenient method for a complete characterization of individual meta-atoms. Once this is achieved, the characterization of assemblies of meta-atoms or meta-surfaces in general can follow. For this purpose, we need to record the information contained in the scattered field of such an object. In the following sections, we will describe the samples preparation, the experimental measurement concept, as well as the detailed description of the simulation procedure.

6.2.1 Sample preparation

Three types of nano-particles will be studied:

- Silica microsphere (purchased from microParticles GmbH) with diameter $D = 304\,\text{nm}$,
- Gold sphere (purchased from Sigma-Aldrich) with diameter $D = 300\,\text{nm}$ and
- Core-shell clusters (meta-atoms), which are fabricated in University of Geneva, using a self-assembly method and have a diameter of $D \approx 310\,\text{nm}$.

Images of the studied nano-partilces, acquired by atomic force microscopy, are shown in Fig. 6.1. Regarding our meta-atom of choice, the core-shell cluster, it is composed of a silica core of diameter $D = 310\,\text{nm}$ (purchased from Bangs Laboratories Inc.), covered with gold nanoparticles of diameter $D = 20\,\text{nm}$. An example of this structure is shown in Fig. 6.2, which is taken using transmission electron microscopy. Those plasmonic nanoparticles are fabricated according to the conventional Turkevich method [11]. Briefly, in a round bottomed flask, 600 mL of an aqueous solution of Tetrachloroauric (III) acid (0.25 mM) are heated at 120 °C under vigorous magnetic stirring. When the boiling temperature is reached, the gold is reduced by quickly adding 15 mL of aqueous sodium citrate solution (0.03 M). In about 15 min, the solution color slowly turns from yellow to deep red, resulting in the full reduction of the gold salt into isotropic and monodisperse gold nanoparticles. The self-assembly technique benefits from the electrostatic interaction between the constituent materials. For this reason, it is necessary to alter the surface chemistry of the silica microspheres in order to impart a positive charge, thus inducing an electrostatic attraction to the gold nanoparticles, which are negatively charged, as a result of their fabrication method. To achieve that, 0.5 mL of the microspheres are added to 2 mL of a 5% (v/v) solution of N-[3-(trimethoxysilyl)propyl]ethylenediamine in ethanol and stirred for 30 min. The solution is then centrifuged at 4000 rpm for 10 min to remove the excess of organosilane, which is then replaced by the same volume of ethanol. To produce core-shell clusters, 10 µL of the functionalized silica core sphere solution is added to 40 mL of the gold nanoparticles solution while vigorously agitating. The adsorption of the gold nanoparticles is immediate, as evidenced by the rapid color change from red to blue [12]. All the samples we considered here are deposited on a glass microscope slide using the blade-coating technique, so as to place individual particles well separated from their neighbors [13]. The preparation and deposition of the samples were carried out by Rossella Grillo. Because of the randomness in the positions of the samples, only a few measurements were carried out on each sample, in order to demonstrate the functionality and working principle of the proposed technique. This also makes it impossible to image the measured samples with non-conventional imaging techniques, such as SEM or AFM. Arranging the samples in a well-defined grid is the next step to ease the measurements and to enable us to match the results to the corresponding sample.

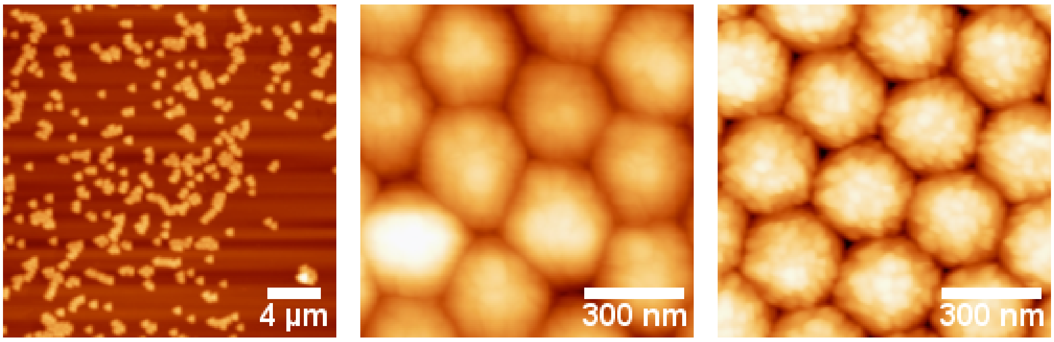

(a) Silica spheres (b) Gold spheres (c) Meta-atom

Figure 6.1 – Atomic force microscopy images of: (a) Silica spheres deposited by blade-coating. There are regions of higher and lower density of particles. (b) Closely packed gold spheres, deposited by dip coating. (c) Meta-atoms directly after fabrication. Images courtesy of Rossella Grillo.

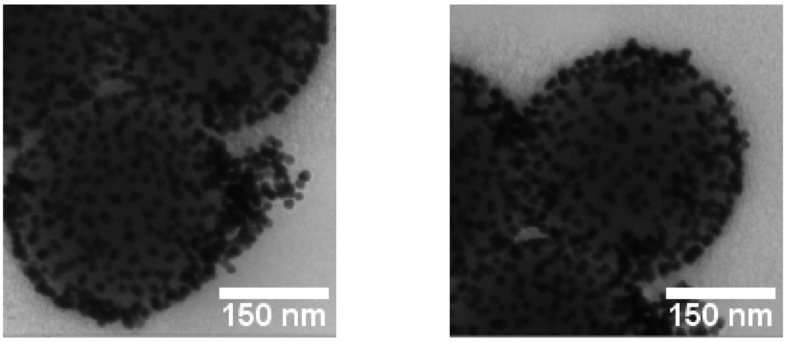

(a) Core-shell meta-atom sample 1

(b) Core-shell meta-atom sample 2

Figure 6.2 – Transmission electron microscopy of core-shell meta-atom. Images courtesy of Rossella Grillo.

6.2.2 Measurement concept

First, we verify the applicability of the measurement procedure by presenting the results acquired for a silica microsphere. Such microspheres are used as the core of the more complex meta-atom. Additionally, we compare the recorded results with simulations to show the validity of the measurement concept. In Figs. 6.3(a) and 6.3(c), the recorded intensity and phase are shown. We image the cross-section of each measurement along the center of the sphere in the direction of propagation, since this region is used to characterize the particles. The solid line indicates the value of intensity and phase along the $x = 0\,\mu\text{m}$ line. The measurements were generally carried out at four different wavelengths, namely at 450 nm, 500 nm, 600 nm and 700 nm to investigate the spectral response of the samples. In Fig. 6.3 we present results at a wavelength of 450 nm. In panels (b) and (d) of the same figure, the corresponding simulated intensity and phase results are plotted. The simulations will be described further below.

The information about the scatterer is encoded in its scattered field, so our purpose is to retrieve the complete information of the total field, which is the intensity and phase. It is clearly seen that both the intensity and the phase are modulated along the central line, which is shown in more detail in Figs. 6.6 and 6.7 for intensity and phase data, respectively. There, the spectral dependent response along the $x = 0\,\mu\text{m}$ line is shown. As we move the sample along the propagation direction, the relative intensity and the phase difference between the incident and scattered field change, and their interference creates the observed modulation effect [14]. The modulation in intensity is used for volumetric tracking of nanometer-sized biological samples [15] and conventional nano- and microparticles [16]. Although those techniques are holographic measurements in principle, they only utilize the intensity to infer the desired parameters, which has, nevertheless, the benefit of enabling fast time-resolved imaging [17]. In our case, we additionally record the modulation of the phase of the total field and use the combined information to compare the measured response of the sample, when illuminated by a plane wave, to the simulated response. We study only the static properties of the sample,

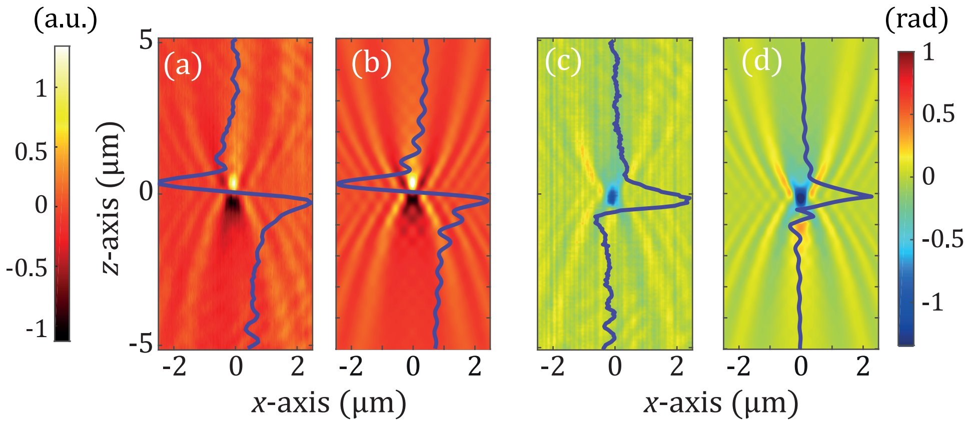

Figure 6.3 – Measured (left) and simulated (right) results of (a), (b) intensity and (c), (d) phase profile of a silica microsphere of diameter $D = 304\,\text{nm}$, when illuminated by plane wave at wavelength of $\lambda = 450\,\text{nm}$. The cross-section is along the x-axis in the middle of the particle and along the propagation direction (z-axis).

so we can afford the increased recording time that the phase extraction requires.

The intensity and phase modulation is strongest at the central line, which is the reason why we use it for comparison purposes. The optical properties of the scatterer (absorption and induced phase) are translated into the scattered field, thus each sample creates, in principle, a different profile. In the following we describe the procedure put in place to obtain these results from the measured raw data.

6.2.3 Simulations

In order to better understand the response of the various structures, we simulate them and also take into account the finite optical resolution of the measuring system imposed by the limited numerical aperture. We implement a plane wave decomposition [18] to have an accurate comparison to the experimental data. The field is obtained by using multiple scattering formalism that solves Maxwell's equations for the pertinent geometry [19].To do this, we consider an x-polarized incident wave, $\mathbf{E}_{\text{inc}} = E_{inc}(x, y, z, \lambda)\hat{\mathbf{x}}$. Using this incident field, we calculate the total field at a certain $x - y$ plane at a distance z_0 from the origin of the scatterer, $\mathbf{E}(x, y, z_0, \lambda) = E_{\text{x}}(x, y, z_0, \lambda)\hat{\mathbf{x}} + E_{\text{y}}(x, y, z_0, \lambda)\hat{\mathbf{y}} + E_{\text{z}}(x, y, z_0, \lambda)\hat{\mathbf{z}}$. Due to the fact that the resulted x-component of the scattered field is much larger than the other two components, we only consider this component in the following. After Fourier transforming the field into the reciprocal space $\hat{E}_{\text{x}}(k_x, k_y, z_0, \lambda)$, we suppress all spatial frequencies larger than those accepted by the numerical aperture of our system (NA=0.95). This technique allows us to reproduce the low-pass behavior of our system. The result is the filtered electric field in reciprocal space, $\hat{E}_{\text{x}}(k'_x, k'_y, z_0, \lambda)$, as it is filtered by the microscope objective. Then, we forward and backward propagate this referential field at different z, $\hat{E}_{\text{x}}(k'_x, k'_y, z, \lambda)$. Finally, we transform it back to real space by using inverse Fourier transform and obtain the field at the same z, $E_x(x, y, z, \lambda)$. The code that implements the above mentioned technique was written by Radius N. S. Suryadharma and Andreas Vetter. The intensity profiles are the square of the absolute value of the electric field, from which we subtract the intensity of the incident field, $|E_x|^2 - |E_{\text{inc}}|^2$ to ease the comparison with the measured data. This corresponds to the subtraction of the background image, which translates to the subtraction of the incident field intensity, in the experimental data. The phase value is the unwrapped phase difference between the phases of the x component of the total field and the incident field $Unwrap\{\angle E_x - \angle E_{\text{inc}}\}$, which is analog to the data post-processing procedure. In our set-up, the phase accumulated by y- and z-components will not contribute to the signal, as they only appear as the background intensity because the reference field is polarized in x-direction. The phase unwrapping based on weighted (simulations) and unweighted (measurements) least-square method was used [20]. For the remainder of this work, we will use the terms *intensity* and *phase* to describe the modified values we get after processing the data as described in this section.

6.3 Results

6.3.1 Expected behavior

Before we present the results obtained by our method, we show spectral response of every simple structure (sphere) used in this work, since this gives us an additional insight when interpreting the obtained data.

Starting with Fig. 6.4, we plot the calculated cross-sections for a single silica sphere, gold sphere and gold nanoparticle in panels (a)-(c) respectively. The left y axis shows the cross-section values in nm^2, while the right y axis shows, in smaller font size, the corresponding cross-section efficiency, which is dimensionless. Their relation is:

$$CS = Q_{eff} \cdot A, \tag{6.1}$$

where CS is the cross-section, Q_{eff} is the cross-section efficiency and A is the area of each particle. The cross-section efficiency shows how much optically larger or smaller a particle is, compared to its physical cross-section. The cross-section efficiencies were calculated using Matlab code written by Christian Mätzler that is based on Mie's theory [21]. The black solid line represents the extinction cross-section, the dotted red line represents the scattering cross-section and the dashed blue line represents the absorption cross-section. The relation between those values is:

$$Q_{ext} = Q_{sca} + Q_{abs}, \tag{6.2}$$

where Q_i is the relevant cross-section efficiency.

Those graphs give us insight into the dominant contributor of the extinction cross-section; for the silica sphere, the absorption is negligible across the whole spectrum and the extinction is only due to scattering. For the gold sphere case, the behavior depends strongly on the wavelength; for $\lambda < 500\,\text{nm}$, both scattering and absorption have comparable contributions to the total extinction, while for $\lambda > 600\,\text{nm}$ the scattering becomes clearly dominant. The region $500\,\text{nm} \leq \lambda \leq 600\,\text{nm}$ is transitional. Finally, we note that the extinction of the gold nanoparticle is always dominated by absorption.

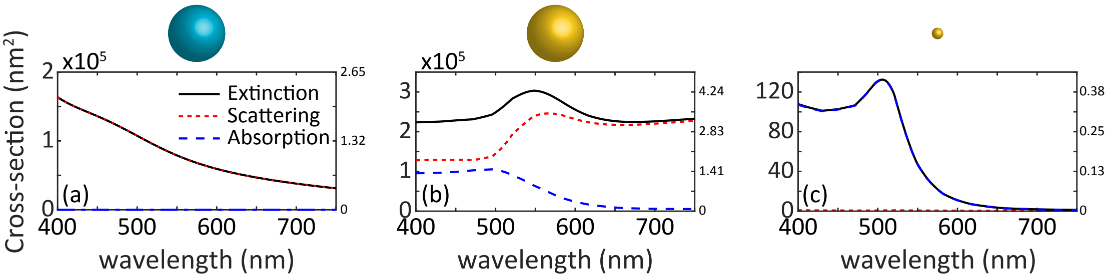

Figure 6.4 – Simulated cross-sections of (a) $D = 310\,\text{nm}$ silica sphere, (b) $D = 300\,\text{nm}$ gold sphere and (c) $D = 20\,\text{nm}$ gold nanoparticle using Mie's theory.The extinction cross-section of the silica sphere is dominated by scattering. For the gold sphere case, scattering and absorption have comparable contributions for $\lambda < 500\,\text{nm}$; for $\lambda > 600\,\text{nm}$ scattering becomes dominant and there is a transitional regime between $500\,\text{nm} \leq \lambda \leq 600\,\text{nm}$. For the gold nanoparticle case, absorption is always dominant.

The same behavior of the particles is also verified by the spectrally measured extinctions, shown in Fig. 6.5, for the cases of a silica sphere of $D = 310\,\text{nm}$, a gold sphere of $D = 300\,\text{nm}$ and a gold nanoparticle of $D = 20\,\text{nm}$ in panels (a)-(c) respectively. The measurements are a courtesy of Rossella Grillo and were carried out in colloidal solutions, although the concentration is not known. We note that the silica sphere shows a smooth, decreasing profile. The gold sphere shows little change in the extinction spectra; the second, broad peak for $\lambda > 600\,\text{nm}$ is due to agglomeration of many particles, which is expected for gold spheres of that size. The gold nanoparticles show a pronounced peak around $\lambda = 520\,\text{nm}$ and for longer wavelengths their extinction reduces, until it become negligible around $\lambda = 700\,\text{nm}$. The qualitative agreement between Figs. 6.4 and 6.5 is satisfactory; all examined cases show the same trends. However, without knowledge of the concentration of particles in the colloidal solution, a quantitative comparison is not straight-forward.

Having shown the spectral behavior of the simple particles, we move on to present the experimental and simulated results and compare them. The intensity plots have been normalized to the absolute value of the global maximum of each set of lines.

6.3.2 Silica sphere

We will begin with the results obtained for a silica sphere of diameter $D = 304\,\text{nm}$. Although its size is slightly different from the spheres used in the previous section, the same behavior

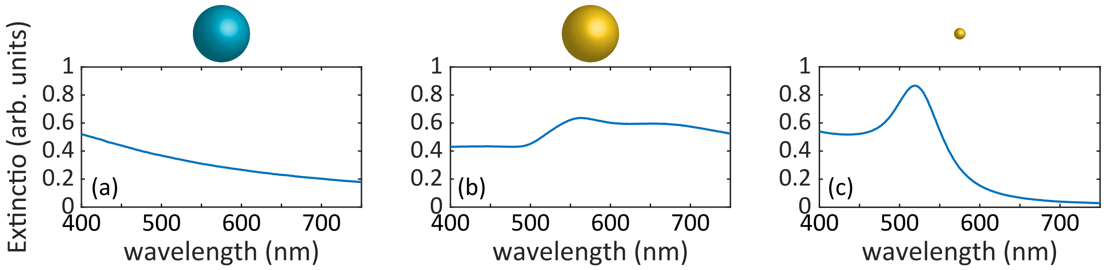

Figure 6.5 – Measured extinction spectra of (a) $D = 310\,\text{nm}$ silica sphere, (b) $D = 300\,\text{nm}$ gold sphere and (c) $D = 20\,\text{nm}$ gold sphere in colloidal solution. The silica sphere shows a smooth, decreasing spectrum. The gold sphere has little change. The second, broad peak at $\lambda = 600\,\text{nm}$ is a characteristic of particle agglomeration. The gold nanoparticle shows a pronounced peak around $\lambda = 520\,\text{nm}$, after which the extinction drops fast, until it becomes negligible for $\lambda > 600\,\text{nm}$.

is expected, since we examine a spectral region away from any resonances. In Figs. 6.6(a) and 6.6(b), the intensity profiles for simulated and recorded data are shown. The agreement between the simulated and the measured data is discussed later on. The profiles in both cases are the same, namely a dip before the position of the particle, followed by a peak just after it, which is the result of the focusing caused by the silica sphere. The focused intensity becomes weaker as the wavelength increases. Another chromatic behavior observed in the measured data, is the slight shift of the peak modulation towards larger z values for longer wavelengths. The dispersion of silica was neglected in the simulations. Finally, we note that the dip is not as pronounced as the peak.

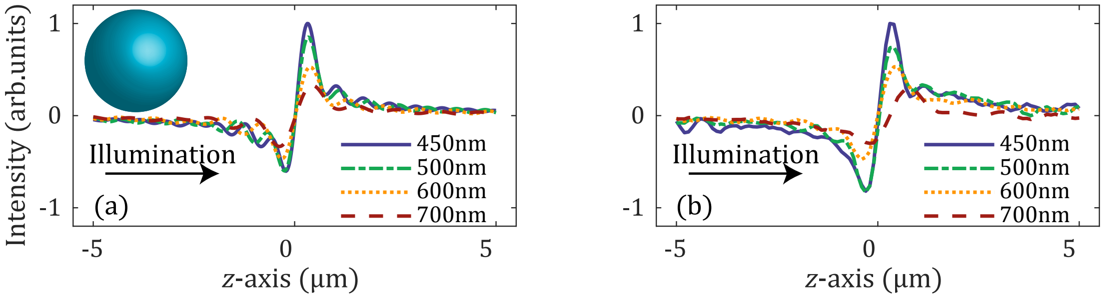

Figure 6.6 – On-axis values of the (a) simulated and (b) measured intensity profiles of the silica microsphere. The results are in good agreement. The peak after the particle is due to focusing, which occurs at the same position for all wavelengths, but decreases in strength as the wavelength increases.

The results for the simulated and recorded phase are shown in Figs. 6.7(a) and 6.7(b), respectively. At the positions where the scattered field has significant power, a retardation (or phase shift) of the total field is observed. As the particle moves away from the focus, the scattered field becomes negligible, and the phase of the total field effectively is that of the incident field. The accumulated phase shift is reduced for longer wavelengths, which can be attributed to the smaller optical path (longer wavevector) inside the sphere. The maximum recorded phase retardation is $\phi \approx -0.4\pi$ for $\lambda = 450\,\text{nm}$ and the maximum simulated phase shift is $\phi \approx -0.5\pi$ for the same wavelength. As a general remark, the phase profiles are smooth for the dielectric sphere and the intensity profiles always show a focusing effect.

The behavior of the dielectric sphere is similar across all wavelengths, it only reduces in strength, as is indicated by Figs. 6.5(a) and 6.4(a).

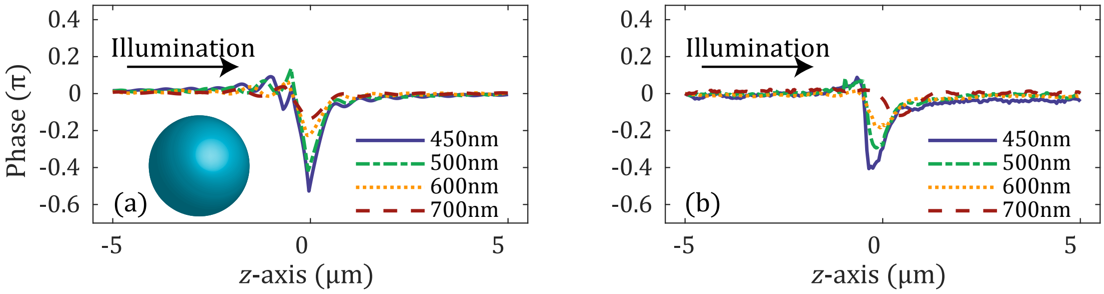

Figure 6.7 – On-axis values of the (a) simulated and (b) measured phase profiles of the silica microsphere. The profiles in both cases are similar, a pronounced phase change at the particle's position. The maximum measured phase shift is -0.4π, while the maximum calculated is -0.5π, a reasonable difference between simulation and experiment. For the dielectric case, the phase profiles are smooth.

6.3.3 Gold sphere

We continue with the intensity results from a gold sphere with diameter $D = 300\,\text{nm}$, that are shown in Figs. 6.8(a) and 6.8(b) for simulation and measurement respectively. We use this particle to demonstrate that the measurement is valid for metals as well and to identify the response of a plasmonic structure. In this case, the asymmetry of the experimental data is more pronounced; possible reasons for will be discussed shortly. Still, the slight discrepancies do not invalidate the generally good agreement between simulations and experiments. The main feature of the metallic sphere is the strong dip at the particle's position, which arises from extinction, and the absence of the focusing effect due to the same reason. We note however, that the peak at positive z values is more pronounced for $\lambda = 600\,\text{nm}$ (simulation) and 700 nm (simulation and experiment), where the extinction is dominated by scattering.

The simulated and measured phase values of the gold nanosphere are shown in Figs. 6.9(a) and 6.9(b) respectively. Again, the agreement is quite good, showing a peak and a dip for both cases and an abrupt phase change. The profiles are different compared to the dielectric measurements, which confirms that the scattering cross-section of the particle changes the results and the central profile can be used for benchmarking. There is a spectral dependency that is, nevertheless, rather weak. This is quite reasonable considering the large size of the object and the absorptive nature of the material from which it is made. It is a strongly dissipative system that smoothens out tremendously a possible spectrally narrow response.

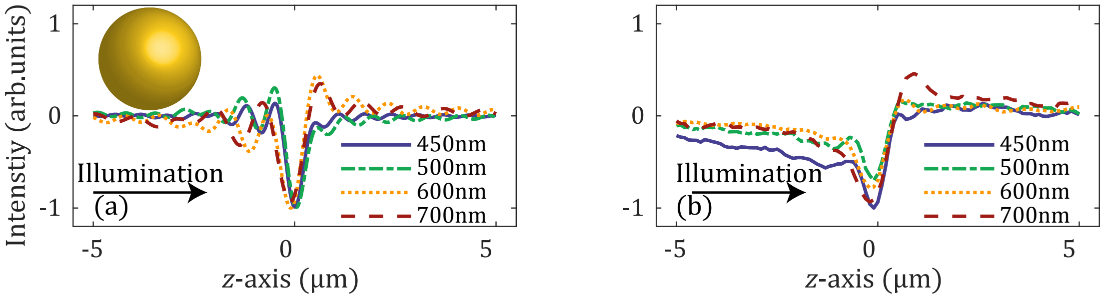

Figure 6.8 – On-axis values of the (a) simulated and (b) measured intensity profiles of the gold sphere. The profiles are in satisfying agreement. The main features are the dip at the particle's position and the absence of focusing effect that are the result of the metallic nature of the particle. This is in contrast to the results obtained for the dielectric sphere.

The central dip in the intensity profile of the gold sphere is comparable across all wavelengths, since its extinction does not change much. At longer wavelengths, where the scattering becomes dominant, an intensity peak appears at positive z values. The phase profile has a similar shape across all wavelengths, that is different from the dielectric one, both in form and in values. Those findings are consistent with Figs. 6.5(b) and 6.4(b).

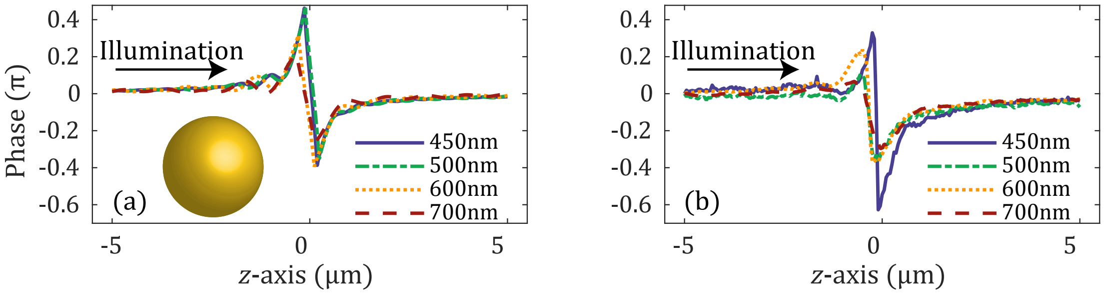

Figure 6.9 – On-axis values of the (a) simulated and (b) measured phase profiles of the gold sphere. The agreement between the profiles is satisfactory, both showing a peak, immediately followed by a dip and an abrupt phase change between them. These sudden changes are in contrast to the dielectric case.

At this point, we should comment on the agreement between simulation and measurement, that is satisfying, especially for the form of the profiles. The disagreement between the values and the contrast (difference between minimum and maximum value) can be explained by a number of reasons. Firstly, the bandwidth of the source, although limited ($BW \approx 10\,\mathrm{nm}$), is still wider than that considered in the simulations (that is essentially strictly monochromatic), so very sharp resonant effects captured in the simulation are smoothed out in the measurement. Additionally, aberrations are always present in the measurements, so we cannot capture a perfect representation of the measured field. This leads to a decreased contrast in the measured results. Finally, we are looking for small variations in a strong background, so noise also impacts the final results. We do not consider variations from the nominal shape (spherical) and size as a reasons for creating discrepancies between simulation and experiment, since any small variation produces unlikely any observable effect. There will be differences in the multipolar composition but this is unlikely to be drastic. It should be stressed, that, since the size of the examined particles is smaller than the resolution of the imaging system, we do not use the interferometric microscope to image the samples themselves, but rather to collect the scattered light and the illumination field.

6.3.4 Meta-atom

After using two simple structures, in this section we will finally show the results for the core-shell cluster meta-atom. In Figs. 6.10(a) and 6.10(b) the simulated and experimental intensity profiles are shown respectively, which bear greater resemblance to the dielectric case compared to the metallic one. The profile with the dip and peak just before and after the particle is retained, although the focusing effect deteriorates faster. The simulated results show a shift in the peak position, that can be attributed to the spectral behavior of the gold nanoparticles. Moreover, the intensity at $\lambda = 500\,\mathrm{nm}$, close to the absorption peak of the gold nanoparticles, is less than the peak at $\lambda = 600\,\mathrm{nm}$. The focusing effect is still comparable and more pronounced than that of the measurements. The recorded data outline a similar profile to that shown in Fig. 6.6(b), only with broader and shallower peaks, that can be attributed to the additional losses introduced by the gold nanoparticles, which is how they mainly manifest. Therefore, the simulations show that the effect of the gold nanoparticles is demonstrated by the spectral shift and the change of the value of the intensity peak; the light is still focused, though the effective refractive index is different compared to the dielectric core alone. This is consistent with the difference between the scattering cross-sections of the dielectric core $(_{mean} \approx 1 \times 10^5\,\mathrm{nm}^2)$ and the gold nanoparticles$(C_{max} \approx 130\,\mathrm{nm}^2)$.

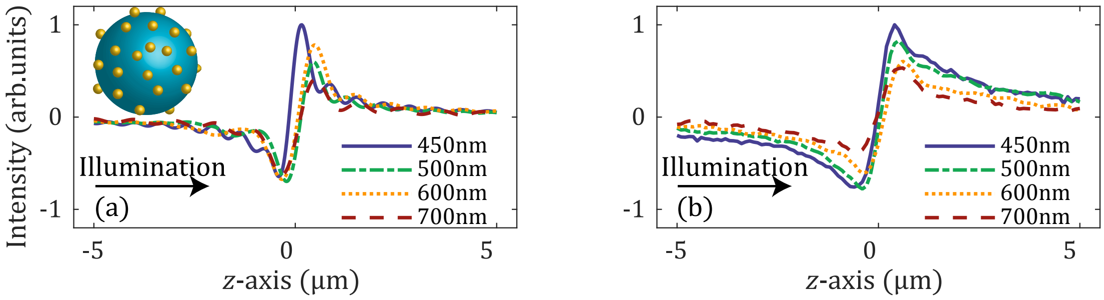

Figure 6.10 – On-axis values of the (a) simulated and (b) measured intensity profiles of the core-shell cluster meta-atom. The profiles resemble strong those of the silica nanosphere, although the position and the intensity of the focus are not the same.

The phase results for the same meta-atom are shown in Figs. 6.11(a) and 6.11(b) for simulation and measurement respectively. They resemble the response of the silica case more than the gold sphere, with a pronounced phase change at the position of the particle.Comparing Figs. 6.7(b) and 6.11(b), we notice that in the first case the accumulated phase is reduced gradually, while in the latter figure there is a sudden drop of the phase accumulation for illuminating wavelength $\lambda > 500\,\text{nm}$. This difference is due to the effect of the gold nanoparticles around the dielectric core.

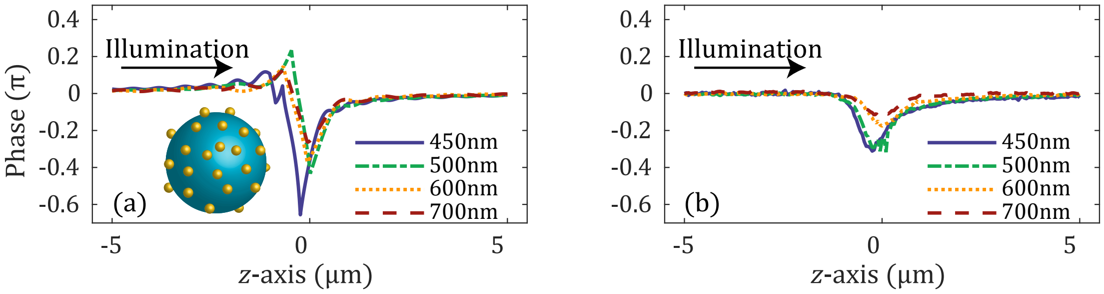

Figure 6.11 – On-axis values of the (a) simulated and (b) measured phase profiles of the core-shell cluster meta-atom. The profiles resemble strong those of the silica nanosphere, showing a pronounced phase change at the particle's position. However, the wavelength at which the phase accumulation changes more is different, showing the effect of the gold nanoparticles.

From the simulated data, we observe that the meta-atom still has a focusing effect, and that the accumulated phase is comparable to the simulated silica microsphere case. The experimental data though show a significantly less pronounced focusing effect and less phase accumulation compared to silica measurements. Consequently, we can observe a different effect of the gold nanoparticles. This is justified by an excess of gold nanoparticles, due to the fabrication and deposition process, which creates a layer and alters the results. The excessive gold nanoparticles have a greater influence than those on the dielectric core. This can be seen in Figs. 6.12(a) - 6.12(c), which show scanning electron microscopy images of the samples. It is shown that less gold nanoparticles attach on the surface of the silica core when compared to the gold nanoparticles lying around it. Under those conditions, we could assume that the principal effect of the gold nanoparticles is to change the effective refractive index of the dielectric core and its surrounding medium. Consequently, the extinction cross-section shown in Figs. 6.4(c) and 6.5(c) is not guaranteed to apply in this case.

Under optical microscopy in reflection configuration, the sample is imaged as shown in Figs. 6.13(a) - 6.13(c), where brightfield, darkfield, and defocused darkfield images of the sample are shown, respectively. Again, we notice a large particle with many more, smaller particles in close proximity. The scattering of the larger particle is dominant, since it is much brighter in the darkfield imaging, even when it is out of focus.

6.4 Experimental results discussion

In the last part, we discuss and summarize the experimental findings. The results are shown in Figs. 6.14 - 6.17 for 450 nm to 700 nm, respectively. In all figures, panel (a) includes the intensity measurements, while panel (b) shows the phase regime.

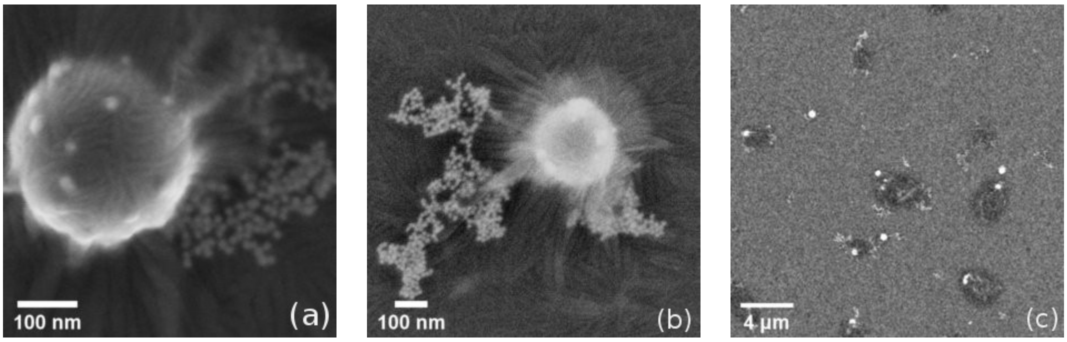

Figure 6.12 – Scanning electron microscopy images of the sample. (a),(b): Dielectric core with gold nanoparticles attached to it and excessive nanoparticles around. (c): Larger overview showing individual dielectric cores (bright spots), with the excess of gold nanoparticles clearly visible.

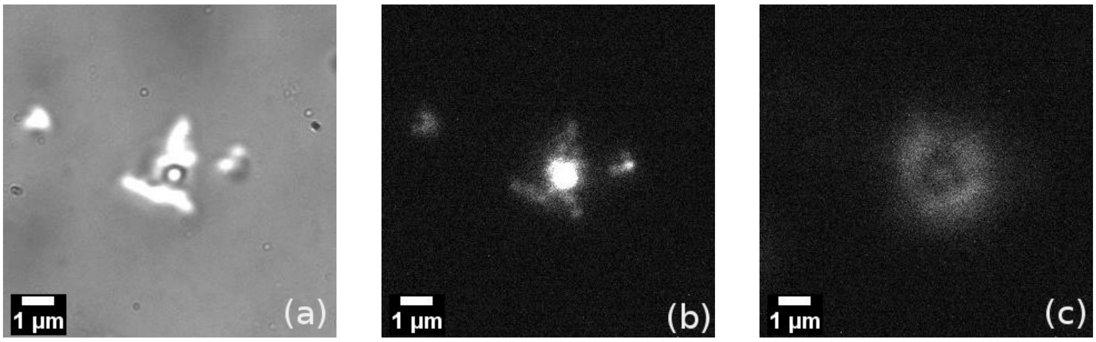

Figure 6.13 – Reflection microscopy. (a) Brightfield, (b) darkfield and (c) defocused darkfield images of a core-shell cluster meta-atom. The excessive gold nanoparticles around the dielectric core that dominates the response are shown. The defocused image shows that the dominant scattering arises from the central particle, indicating that it is the larger silica sphere.

Figure 6.14 shows that at $\lambda = 450\,\mathrm{nm}$, the dielectric and metallic particles are distinguishable either from the intensity or the phase profiles, due to their different behavior or pure scattering versus combined scattering and absorption respectively.The cluster of the gold nanoparticles is seen in the longer tail of the meta-atom profile.

The phase retardation of the silica sphere is reduced when moving from $\lambda = 450$ nm to 500 nm, while it remains constant for the meta-atom, as can be seen by comparing Figs. 6.14(b) and 6.15(b). This can be attributed to resonance of the $D = 20\,\mathrm{nm}$ nanopartilces around $\lambda = 520\,\mathrm{nm}$ that can be shifted due to size variations and aggregation of excess particles [22]. Also, Fig. 6.15 shows that the distinction between the dielectric and metallic sphere is greater in the intensity data, compared to the phase.

The results at the wavelength of $\lambda = 600\,\mathrm{nm}$ are shown in Fig. 6.16. The extinction of the gold sphere is dominated by scattering, which can be related to the peak that starts to appear at positive z values, resembling the dielectric case. The phase profile of the same particle is still

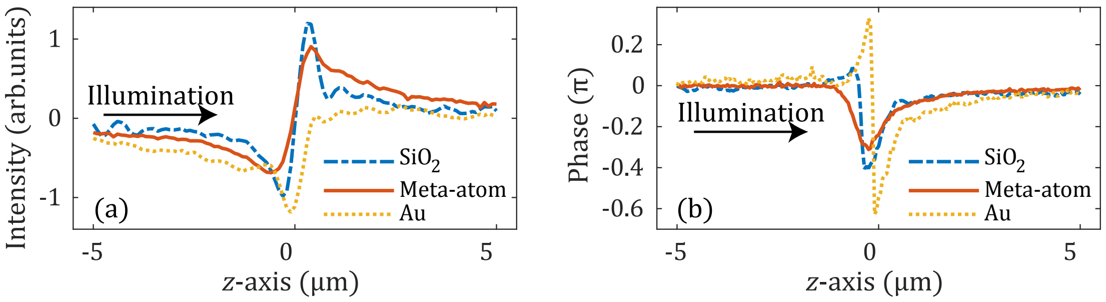

Figure 6.14 – Measured on-axis (a) intensity and (b) phase values of silica microsphere (SiO_2), core-shell cluster structure (Meta-atom) and gold sphere (Au). The illumination wavelength is $\lambda = 450\,\text{nm}$. The meta-atom profile resembles strongly the silica sphere. The metallic particle can be distinguished both in intensity and phase measurements.

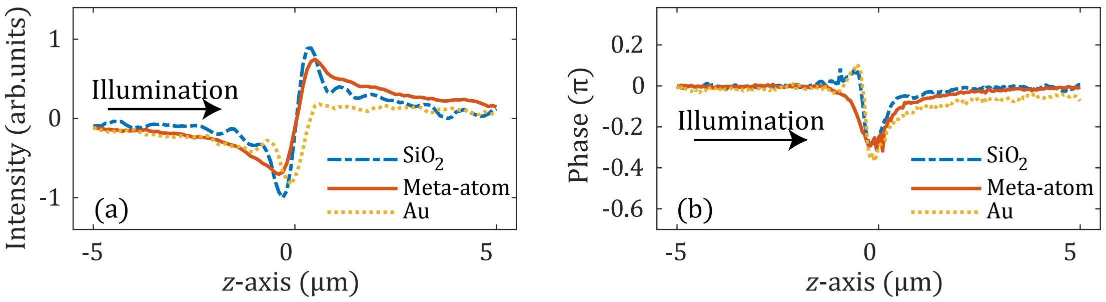

Figure 6.15 – Measured on-axis (a) intensity and (b) phase values of silica microsphere (SiO_2), core-shell cluster structure (Meta-atom) and gold sphere (Au). The illumination wavelength is $\lambda = 500\,\text{nm}$. The dielectric sphere has accumulated less phase compared to the previous measurement (Fig. 6.14), while the meta-atom the same, due to the presence of the gold nanoparticles. In this case, the metallic sphere can be easier distinguished in the intensity regime.

quite indicative, thus the distinction between dielectric and metallic particle is easier in the phase regime.

Figure 6.17 compares the studied particles at $\lambda = 700\,\text{nm}$, where we see that the peak of the metallic sphere is more pronounced compared to the previous case of $\lambda = 600\,\text{nm}$ and reaches the value of the intensity peak of the dielectric particle. Contrary to the dielectric case, the dip is still significant, which is a result of the greater extinctions cross-section of the metallic sphere. The meta-atom shows an smaller displacement along the z axis compared to the bare core. Nevertheless, the effect of the nanoparticles is concentrated on the longer tail of the peak. Distinguishing the dielectric from the metallic sphere can be done either in intesity or in phase.

Focusing on the silica sphere, we showed that, in the intensity profiles, it creates a focusing effect that diminishes for longer wavelengths; the phase profile shown a similar behavior, since

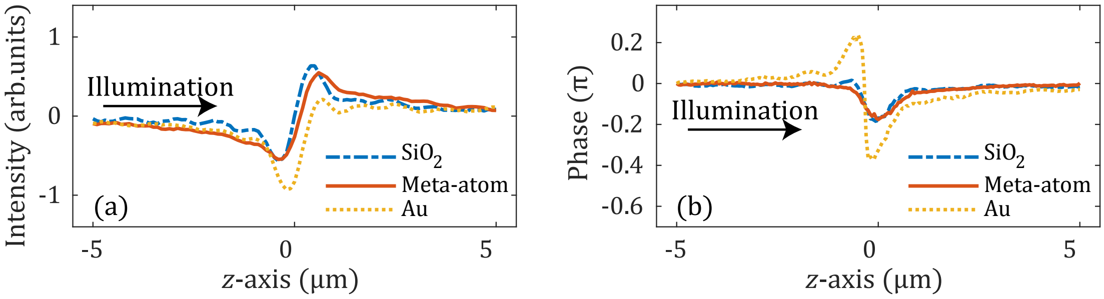

Figure 6.16 – Measured on-axis (a) intensity and (b) phase values of silica microsphere (SiO$_2$), core-shell cluster structure (Meta-atom) and gold sphere (Au). The illumination wavelength is $\lambda = 600\,\text{nm}$. The meta-atom and the silica sphere have almost identical responses, due to the small scattering cross-section of the gold nanoparticles. The intensity response of the gold sphere bears strong resemblance to the silica case, but the profiles in phase are easily distinguishable.

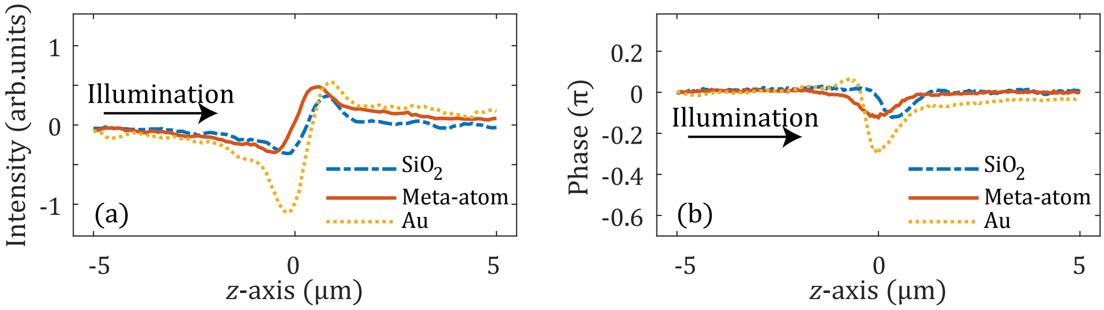

Figure 6.17 – Measured on-axis (a) intensity and (b) phase values of silica microsphere (SiO$_2$), core-shell cluster structure (Meta-atom) and gold sphere (Au). The illumination wavelength is $\lambda = 700\,\text{nm}$

the phase accumulation is gradually reduced. Those trends are supported by the extinction and cross-section plots, that are smooth and decreasing. Additionally, the extinction cross-section is always dominated by scattering, therefore we expect similar behavior across all measurements, with a diminishing strength of the observed effects.

Moving on to the gold sphere of $D = 300\,\text{nm}$, we observe that the extinction cross-section does not change significantly; what changes however is the contribution of scattering and absorption. For wavelengths of $\lambda < 500\,\text{nm}$, the contribution of scattering and absorption are comparable; for longer wavelengths however, the scattering becomes dominant. This is depicted in the measurements as well. The dip in the intensity modulation is comparable for all wavelengths; at $\lambda = 600$ nm and 700 nmhowever, the peak just after the gold sphere is more pronounced, indicating the change in the behavior of the material. The phase modulation does not show a distinct feature, since there is no pronounced resonance, owning to the size of the particle[1], consequently predicting its exact trend is complicated. Comparing however this

---

[1] the combination of the large size of the metallic sphere with the losses of the material broaden the resonance

gold sphere to the dielectric one, we observe that, generally, the scattered field accumulates more phase, which is consistent with the larger values of the extinction cross-section.

Relating the extinction cross section of an individual gold nanoparticle to the measurements of the meta-atom is not straight-forward, because the distribution of the former on the dielectric core is quite sparse; most of them are closely packed around and underneath the dielectric core. This changes their expected response and that is hinted by the fact that the effect they have on the dielectric core is similar across all wavelengths, namely weakening the focusing effect by creating a longer tail of the intensity peak. This is also observed at $\lambda = 700\,\text{nm}$, where the gold nanoparticles should practically no effect, due to their negligible optical cross-section. However, they still influence the response of the meta-atom, since the potential coupling due to proximity, enlarges the extinction cross-section. Also, the phase measurements indicates the resonance of the gold nanoparticles around $\lambda = 520\,\text{nm}$.

The conclusion drawn from the above discussion, is that having access to intensity and phase information across different wavelengths is beneficial in many aspects. We can relate the measured data with the material properties translated into their cross-sections and also explain some deviations as a result of fabrication inaccuracies. Also, the different behavior of the various materials is not always optimally expressed in a singe regime; capturing both guarantees that separating different nanoparticles is possible. Of course, we showed that only for a limited variety of samples and measurements. More data is necessary, especially on *reference* samples, before we can safely generalize those findings. Having access to more measurements, we can create a map of the intensity and phase profile for different materials (shapes, sizes, etc.) at different wavelengths; in case an unknown sample should be identified, we can use such a map to correlate its features to the samples already studied.

---

peaks, smoothing the transmission spectrum.

Bibliography

[1] V.G. Veselago. The electrodynamics of substances with simultaneously negative values of epsilon and mu. *Soviet Physics Uspekhi*, 10(4):509–514, 1968.

[2] I. B. Vendik and O. G. Vendik. Metamaterials and their application in microwaves: A review. *Technical Physics*, 58(1):1–24, January 2013.

[3] Stefan Linden, Christian Enkrich, Martin Wegener, Jiangfeng Zhou, Thomas Koschny, and Costas M. Soukoulis. Magnetic Response of Metamaterials at 100 Terahertz. *Science*, 306(5700):1351, November 2004.

[4] C. Enkrich, M. Wegener, S. Linden, S. Burger, L. Zschiedrich, F. Schmidt, J. F. Zhou, Th. Koschny, and C. M. Soukoulis. Magnetic Metamaterials at Telecommunication and Visible Frequencies. *Physical Review Letters*, 95(20):203901, November 2005.

[5] Costas M. Soukoulis and Martin Wegener. Past achievements and future challenges in the development of three-dimensional photonic metamaterials. *Nature Photonics*, July 2011.

[6] H.O. Moser and C. Rockstuhl. 3d THz metamaterials from micro/nanomanufacturing. *Laser & Photonics Reviews*, 6(2):219–244, April 2012.

[7] Stefan Mühlig, Alastair Cunningham, José Dintinger, Toralf Scharf, Thomas Bürgi, Falk Lederer, and Carsten Rockstuhl. Self-assembled plasmonic metamaterials. *Nanophotonics*, 2(3), January 2013.

[8] Anton Kuzyk, Robert Schreiber, Zhiyuan Fan, Günther Pardatscher, Eva-Maria Roller, Alexander Högele, Friedrich C. Simmel, Alexander O. Govorov, and Tim Liedl. DNA-based self-assembly of chiral plasmonic nanostructures with tailored optical response. *Nature*, 483:311, March 2012.

[9] N. Radius Suryadharma and Carsten Rockstuhl. Predicting Observable Quantities of Self-Assembled Metamaterials from the T-Matrix of Its Constituting Meta-Atom. *Materials*, 11(2), 2018.

[10] José Dintinger, Stefan Mühlig, Carsten Rockstuhl, and Toralf Scharf. A bottom-up approach to fabricate optical metamaterials by self-assembled metallic nanoparticles. *Optical Materials Express*, 2(3):269–278, March 2012.

[11] J. Kimling, M. Maier, B. Okenve, V. Kotaidis, H. Ballot, and A. Plech. Turkevich Method for Gold Nanoparticle Synthesis Revisited. *The Journal of Physical Chemistry B*, 110(32):15700–15707, August 2006.

[12] Stefan Mühlig, Alastair Cunningham, Sebastian Scheeler, Claudia Pacholski, Thomas Bürgi, Carsten Rockstuhl, and Falk Lederer. Self-Assembled Plasmonic Core–Shell Clusters with an Isotropic Magnetic Dipole Response in the Visible Range. *ACS Nano*, 5(8):6586–6592, August 2011.

[13] Hongta Yang and Peng Jiang. Large-Scale Colloidal Self-Assembly by Doctor Blade Coating. *Langmuir*, 26(16):13173–13182, August 2010.

[14] Jaesuk Hwang and W.E. Moerner. Interferometry of a single nanoparticle using the Gouy phase of a focused laser beam. *Optics Communications*, 280(2):487–491, December 2007.

[15] Philipp Kukura, Helge Ewers, Christian Müller, Alois Renn, Ari Helenius, and Vahid Sandoghdar. High-speed nanoscopic tracking of the position and orientation of a single virus. *Nature Methods*, 6:923, November 2009.

[16] Fook Chiong Cheong, Bhaskar Jyoti Krishnatreya, and David G. Grier. Strategies for three-dimensional particle tracking with holographic video microscopy. *Optics Express*, 18(13):13563–13573, June 2010.

[17] Yi-Fan Huang, Guan-Yu Zhuo, Chun-Yu Chou, Cheng-Hao Lin, Wen Chang, and Chia-Lung Hsieh. Coherent Brightfield Microscopy Provides the Spatiotemporal Resolution To Study Early Stage Viral Infection in Live Cells. *ACS Nano*, 11(3):2575–2585, March 2017.

[18] Joseph W. Goodman. *Introduction to Fourier Optics*. Number McGraw - Hill Series in Electrical and Computer Engineering. McGraw - Hill, 2 edition, 1996.

[19] Yu-lin Xu. Electromagnetic scattering by an aggregate of spheres. *Applied Optics*, 34(21):4573–4588, July 1995.

[20] Dennis C. Ghiglia and Louis A. Romero. Robust two-dimensional weighted and unweighted phase unwrapping that uses fast transforms and iterative methods. *Journal of the Optical Society of America A*, 11(1):107–117, January 1994.

[21] Christian Mätzler. MATLAB Functions for Mie Scattering and Absorption. Research Report 2002-08, June 2002.

[22] Viktor Myroshnychenko, Jessica Rodríguez-Fernández, Isabel Pastoriza-Santos, Alison M. Funston, Carolina Novo, Paul Mulvaney, Luis M. Liz-Marzán, and F. Javier García de Abajo. Modelling the optical response of gold nanoparticles. *Chemical Society Reviews*, 37(9):1792–1805, 2008.

7 Conclusions

At this point, we have presented all the studies that were conducted on various cases, each one demonstrating a different aspect of optics and requiring a different feature / method of measurements. The motivation of this work, as well as the principles and concepts that drive it were mentioned in the introduction; however we deem it beneficial to restate them and establish their connection to every sample examined. This is the purpose of this chapter; summarize the work and declare to what extend was the main goal achieved.

The framework of this study is optical metrology, which is the quantitative and qualitative description of the investigated samples using optical means. The physical dimensions of the samples range from a few hundreds of micrometers to few hundreds of nanometers. Consequently, we employ microscopy, specifically in a transmission configuration, that is a well established and straight forward method for examining structures in that length scale. The process followed in every study is, in rough terms, that we illuminate each structure with a well defined field, capture the transmitted light and use the information contained therein to conclude on the characteristic of the sample. Therefore, our objective is to extract specific properties and not necessarily to image the samples themselves; we are looking for fine features and general trends that the samples imprint on the transmitted field and depend on their properties.

Since the transmitted field plays a key role in our study, we want to be able to describe it as precisely as possible. To that extend, apart from the intensity, we also record the phase of field, using interferometry. Moreover, we carry out those measurement at different wavelengths, probing the spectral behavior of the samples as well. Although interferometry and spectral resolution are not new in themselves, their systematic combination constitutes a new concept. There are, of course, examples of spectrally resolved interferometry, using either pulsed sources or white light sources (white light interferometry), whose application range is limited nevertheless, because they are developed for a specific purpose, like refractive index measurement or profilometers. As was already shown, we apply this technique to a wide variety of distinct samples that have different functions and give rise to different optical phenomena. A key point of this work however, is that we have an a priori knowledge of the sample and we use our interferometer to exploit it. We also claim that the phase data are prominent for that purpose, for the reasons explained below.

The first sample we present is a microlens, within the context of providing meaningful fabrication feedback for high numerical aperture lenses. Detailed characterization required microscope objective with high resolving power, which must have limited field of view nevertheless. Our solution is to extract the profile information using phase measurements, which is the conventional method, that are carried out on a different plane along the propagation direction. The results we obtained show the usefulness of this approach. We test the method only on a specific lens; this is the first step, before expanding this method to different microlenses. When combined with the spectral feature of the set-up the potential for a complete characterization of microlenses, in terms of fabrication feedback and chromatic aberration study, becomes apparent.

Moving from a refractive sample to a diffractive one, we investigate a phase element. Such structures affect predominantly the phase of the incoming field and naturally modulate phase stronger than intensity. Thus, imaging such structures in phase results inherently in high contrast. However, we are interested in locating the edges of those elements with the highest possible precision. One phase feature that was briefly mentioned is the phase singularity, which can in principle be localized with arbitrary precision. Their potential is a matter of debate; the ease with which they can now be detected, thanks to the improvement of the recording equipment can boost their use in metrological applications and this work has planted a seed. The main work was focused on finding different characteristic points in intensity and phase profiles to localize the edges. Both approaches (intensity and phase) have comparable performance, which is within the few tenths of nanometers of accuracy. However, it is unclear if this is the case for more complex phase elements that create more than two phase values or operate at different wavelengths. What is certain however, is that this study provides the necessary tools for further investigation and hints towards the phase regime as the natural choice for experiments.

The next phenomenon that was investigated – the photonic nanojet – bridges the diffractive and the refractive regime and might also be observed in the scattering regime. The intensity measurements allow us to examine the spectral evolution of the photonic nanojet effect, measure the characteristics of the created focal spot and set an upper limit to the diameter of a sphere that would create a nanojet. The phase measurements were used to try and identify the change in the behavior of the sphere (diffractive - scattering) as the ratio of the wavelength over the diameter of the sphere increases. The recorded phase maps do show a different profile for different sizes and wavelengths; so do the intensity distribution as well, however the differences in phase are easier to spot. Still, we cannot safely draw a conclusion, since we examined a single sphere. More measurements are required before a safe generalization, the idea is there and the first step is nevertheless taken.

We conclude the experimental measurements with a study on nano-sized, sub-wavelength particles; for the first time we probe single core-shell meta-atoms, composed of a dielectric core around which gold nanoparticles are attached. The measuring concept is based on the fact that every particle creates a different scattered field, because of its unique features (size, shape, refractive index, etc.). When those particles are studied under the microscope, we capture the total field, i.e. the interference between the scattered and the illuminating field; consequently when we translate the samples through the focus of the objective, we record the intensity and phase of the total field at different distances from the sample. Using this technique, we provide a tool to better understand the behavior of complex structures, such this meta-atom, that can be show either dielectric or metallic behavior, depending on the wavelength of the incoming light. Additionally, we demonstrated that the comparison between the basic particles (dielectric and metallic spheres), the simulations and the measured results of the meta-atom can be used to assess its performance. Similarly, provided enough reference measurements, we can differentiate between different particles. The next step is to create those references and use the intensity and phase profile to extract the properties, like the effective refractive index of complex structures, like meta-atoms or meta-surfaces.

Considering the above summary of the experiments, we can conclude that this work keeps true to the claim that investigating the phase provides distinct advantages; this should not be taken as a statement that intensity is needless. The studied cases, although different to each other, remain specific, since few samples of each category were examined. The closing remark of each experiment paragraph was that further investigation is needed, before safely generalizing the findings. In other words, this works sets a solid basis upon which the phase investigation for different applications can be supported; building up on those results will be done in future work. It is the current trend in research generally to acquire large volume of data and use the abundant processing power of computers to analyze and extract general patterns. This could be used for example to improve the surface reconstruction accuracy of the intermediate plane measurement, or establish a relationship between the slope of the phase profiles of diffractive elements and their physical wall slope. It could also reveal which features are more indicative for identifying the transition between the scattering, diffractive and refractive regimes of nano- and macro-scaled elements. Creating a database of the response of different particles and link it to their size, shape and effective refractive index can be applied to particle identification and meta-material structuring. The message is that using the tools presented in this work, large amount of data can be produced, which can be potentially used for different purposes.

Regarding the methodology itself, there are also aspects that can be further studied. Apart from optimizing the techniques presented in each chapters individually, there are benefits for analyzing the basic principles of this work in more detail. To give an example, establishing a signal to noise ratio for phase measurements (and proving that they are more resilient to specific noise) might make evident the advantages of probing samples in the phase regime. A better understanding of the phase unwrapping effect on the extracted phase maps will clarify when it is necessary to be done and what might be the most appropriate way to do it. This is also linked to the value of phase acquisition in low light regions.

We are confident that this work is complete, although not exhaustive. To condense all the above, the writer would be happy if this work would encourage further research and aspire new paths to explore, rather than be taken as establishing new standards.

Michail Symeonidis | Curriculum Vitae

Avenue Jomini 17, 1018 Lausanne – Vaud, Switzerland
☎ (+41) 76 74 33 135 • ✉ misymeonidis@gmail.com

Education

Ècole Polytechnique Fédérale de Lausanne
PhD candidate *2015 – present*

Aristotle University of Thessaloniki
Diploma in Electrical and Computer Engineering, GPA – 7.78/10 *2006–2013*
Graduated 37th of my year out of 281

German School Thessaloniki
Highschool Diploma (Apolytirion Lykiou), GPA – 18.3/20 *2000–2006*
Abitur, GPA – 1.6

Diploma Thesis

Title: *Theoretical and Experimental Study of Four Wave Mixing and Stimulated Raman Scattering in Optical Fibers.*

Supervisor: Professor Dr. Emmanouil E. Kriezis

Description: In this thesis the non-linear phenomena of Four Wave Mixing (FWM) and Stimulated Raman Scattering (SRS) were studied, both theoretically and experimentally. The experimental results were compared to the simulated ones and their similarity reached a satisfactory level. As for FWM, the conditions that optimise this phenomenon were investigated, along with its competence for telecommunicational applications. In the case of SRS, Polarisation Dependent Gain was studied in two different types of optical fibres, so as to calculate specific parameters and relations needed to evaluate a Raman amplifier.

Experience

Greek Army Service
Private (Research Informatics) *11.2013–8.2014*
I served at the Bureau of Research Informatics as a computer analyst and programmer.

TED^x Thessaloniki
Volunteer *4.2013 & 5.2012*
The volunteers helped to prepare and carry out the event.

Hellenic Telecommunications Organization (OTE S.A.) **Thessaloniki**
ADSL help-desk / Call centre agent *10.2009–10.2010*
Provided help related to ADSL, Internet and other services' problems (eg. e-mail).

University projects

Photonics Technology: Modelization of photonic components using Matlab. *Feb. 2013*

Electromagnetic Compatibility: Simulation and manufacturing of microwave meta-material filter. The simulation was made using the CST studio suite and the manufacturing through chemical etching. Antennas found in literature. *Feb. 2013*

Microwaves: Analysis and modelization of the function of microwave components and circuits using Matlab. *Feb. 2013*

Topics in Antennas - Antennas Synthesis: Simulation of linear antennas using 4nec2 and micro-strip dual-layer antennas using Sonnet. Antennas found in literature. *Jun. 2012*

Wireless Communication: Design the radio-coverage network of the county of Thessaloniki for terrestrial digital TV needs. *Sep. 2012*

Advanced Signal Processing Techniques: Analysis of EEG signals using higher order statistics in order to predict a person's sentimental state. This project was the result of a four-people team. *Sep. 2012*

Applied Telecommunication Systems: Information-oriented, based on bibliography project on wireless power transmission. *Jun. 2011*

Computer skills

Language: C, C++, JAVA, HTML, CSS, PYTHON

Tools: LaTeX, Matlab, CST, Sonnet, 4nec2, Radio-Mobile, PSpice

Miscellaneous: Microsoft Office, CorelDRAW, AutoCAD, Adobe Illustrator, GIMP

Languages

Greek: Mother tongue

English: Fluent *Holder of C2*

German: Good *Abitur*

French: Beginner *Self-assessed level: A1*

Interests

- Climbing
- Board games
- Literature / Poetry
- Music
- Sailing
- Winter sports
- Popular science reading

List of publications

Peer reviewed:

M. Symeonidis, R.S .Suryadharma, R .Grillo, A. Vetter, C .Rockstuhl, T. Bürgi, T. Scharf

High-resolution interference microscopy with spectral resolution for the characterization of individual particles and self-assembled meta-atoms
Opt. Express 27, 20990-21003 (2019)
M. Symeonidis, W.Nakagawa, D-C. Kim, A. Hermerschmidt, T. Scharf

High-resolution interference microscopy of binary phase diffractive optical elements
In peer review
J. Béguelin, M. Symeonidis, W. Noell, R. Völkel, T. Scharf

Towards a complete and meaningful characterization of high NA microlenses by high resolution interference microscopy
Submitted
SPIE Proceedings:

J. Béguelin, M. Symeonidis, W. Noell, R. Völkel, T. Scharf

Assessing microlens quality based on 3D irradiance measurement at the focal spot area
Volume 10678 (2018)
M. Symeonidis, D-C. Kim, A. Hermerschmidt, M-S. Kim, T. Scharf

Diffractive optical elements investigation in the phase domain
Volume 10914 (2019)
M. Symeonidis, R.S .Suryadharma, R .Grillo, T. Scharf, C .Rockstuhl, T. Bürgi

Engineered nanostructures characterization by spectral interferometric microscopy
Volume 10927 (2019)
M. Symeonidis, M-S. Kim, T. Scharf

Are photonic nanojets achromatic?
Volume 10930 (2019)

List of conferences

Poster: M. Symeonidis, T. Scharf

Amorphous Metamaterial Composed out of Meta-atoms
Photonics Day, EPFL,Lausanne (2016)
Poster: M. Symeonidis, T. Scharf

SPECTRAL HIGH RESOLUTION INTERFERENCE MICROSCOPE (sHRIM)
Photonics Day, EPFL,Lausanne (2017)
Poster: M. Symeonidis, M-S. Kim, T. Scharf

Are Photonic Nanojets Achromatic?
Photonics Day, EPFL,Lausanne (2018)
Oral presentation: T. Scharf

Singularities behind microstructures under different coherence conditions
WIO Canada (2018)

Oral Presentation: M. Symeonidis, J. Béguelin

Spectral High Resolution Interferometry for Broadband Characterisation of Optical Components
EOSAM, Delft (2018)
Oral presentation: M. Symeonidis

Engineered nanostructures' characterization by spectral interferometric microscopy
Photonics West, San Francisco, California, USA (2109)
Poster: M. Symeonidis, M-S. Kim, T. Scharf

Are Photonic Nanojets Achromatic?
Photonics West, San Francisco, California, USA (2109)
Poster: M. Symeonidis, D-C. Kim, A. Hermerschmidt, M.S. Kim, T. Scharf

Diffractive Optical Elements Investigation in the Phase Domain
Photonics West, San Francisco, California, USA (2109)
Poster: M. Symeonidis, R.S. Suryadharma, R. Grillo, A. Vetter, C. Rockstuhl, T. Bürgi, T. Scharf

High-resolution interference microscopy with spectral resolution for the characterization of individual particles and self-assembled meta-atoms
Swiss NanoConvention (2019)

Ce document a été imprimé au Centre d’impression EPFL,
imprimerie climatiquement neutre, certifiée myClimate.